3D Site-Scale Geological Model in the Revell Batholith:

Model Version 1.0

NWMO-TR-2021-12 June 2021

Aaron DesRoches, Lindsay Waffle, Andy Parmenter
Nuclear Waste Management Organization (NWMO)

NUCLEAR WASTE MANAGEMENT ORGANIZATION
SOCIÉTÉ DE GESTION DES DÉCHETS NUCLÉAIRES

Nuclear Waste Management Organization
22 St. Clair Avenue East, 6th Floor
Toronto, Ontario
M4T 2S3
Canada

Tel: 416-934-9814
Web: www.nwmo.ca

3D Site-Scale Geological Model in the Revell Batholith: Model Version 1.0

NWMO-TR-2021-12

June 2021

Aaron DesRoches, Lindsay Waffle, Andy Parmenter
NWMO

Document History

Title:	**3D Site-Scale Geological Model in the Revell Batholith: Model Version 1.0**		
Report Number:	NWMO-TR-2021-12		
Revision:	R000	Date:	June 2021
Nuclear Waste Management Organization			
Authored by:	Aaron DesRoches, Lindsay Waffle, Andy Parmenter		
Reviewed by:	Raymond Munier (TerraMobile)		
Accepted by:	Sarah Hirschorn		

Revision Summary		
Revision Number	**Date**	**Description of Changes/Improvements**
R000	2021-06	Initial issue

ABSTRACT

Title: **3D Site-Scale Geological Model in the Revell Batholith: Model Version 1.0**

Report No.: **NWMO-TR-2021-12**

Author(s): Aaron DesRoches, Lindsay Waffle, Andy Parmenter

Company: NWMO

Date: June 2021

Abstract

Developing a site-scale 3D geological model is an essential part of the Descriptive Geoscientific Site Model. The objective of this report and the 3D geological model is to develop a numerical representation of the subsurface that can be further used to evaluate the site for its potential to host a deep geological repository. This geological model forms the site framework to be used in associated geoscientific studies to develop discipline-specific sub-models, including geomechanical, thermal, hydrogeological, hydrogeochemical, and transport property models. This report defines the first iteration of the site-scale geological model, which incorporates a significant amount of information measured from the ground surface and subsurface information collected mainly from three drilled boreholes within the site-scale extent.

This initial version 1.0 of the 3D model is considered to be sparsely constrained. It is acknowledged that building a 3D model with sparse data will have a high degree of uncertainty, and the projected information will most likely not be completely accurate. The main sources of uncertainty in this iteration of the 3D model are sparsity of data, integrated rock unit and structural unit modelling, poorly defined variogram, and the difficulty linking borehole HFFI to surface lineaments. Eventually, as additional data is acquired and used in the model, remaining uncertainties will be minimized. Continually updated models will ultimately inform other geoscientific disciplines and will form the framework used in the design of an underground repository and the assessment of long-term safety of the site.

TABLE OF CONTENTS

ABSTRACT iii

1. Introduction 1
- **1.1 Scope and Objectives 1**
- **1.2 Model Version and Data Freeze 2**
- **1.3 Terminology 3**
- **1.4 Software 4**

2. Summary of Geology 4
- **2.1 Geological Setting 4**
- **2.2 Structural and Metamorphic History 9**

3. Model Inputs 11
- **3.1 Water Features and Overburden Cover 11**
- **3.2 Revell Site Area Geology 13**
- **3.3 Borehole Data 20**
- **3.4 LiDAR Digital Elevation Model and Aerial Imagery 21**
- **3.5 Airborne Geophysics 24**
- **3.6 Interpreted Lineaments 26**

4. Geological Data Integration 28
- **4.1 Updated Site-scale Lineament Map 28**
- **4.2 Compilation of Single Borehole Integration Reports 32**
- **4.3 Conceptual Geological Integrated Summary 58**

5. Geological Model 61
- **5.1 General Principles and Overview 61**
- **5.2 Geological Modelling Approach 62**
- **5.3 Integrated Rock Unit Modelling 63**
- **5.4 Integrated Structural Unit Modelling 68**
- **5.5 Deterministic Fracture Zone Modelling 77**
- **5.6 Diabase Dyke Surface Model 90**
- **5.7 Combined Models 91**

6. Confidence Assessment 93
- **6.1 Main Uncertainties 94**

7. Summary 96

8. References 98

Appendix A: Summary of Inferred Fracture Zone (IFZ) Attributes 106

LIST OF TABLES

Table 1: The Archean and Proterozoic structural and metamorphic history of the Revell Regional Area, summarized by time, and based on a sequence of deformation events established regionally. See also schematic summary of events shown in Figure 5. 10

Table 2. Description of surficial water feature and overburden data. 12

Table 3. Total logged length and percentage of distinct rock types recorded in each borehole. Distinct rock types were determined by geological core and geophysical logging, combined with petrographic and lithogeochemical data. 33

Table 4. High fracture frequency intervals (HFFI) identified in boreholes IG_BH01, IG_BH02, and IG_BH03 (Parmenter et al. 2021a, 2021b and 2021c). 53

Table 5. Rock unit interval top and bottom depths along drilled boreholes. Rock unit (RU) represents the interpretation domain based on the single borehole integration report, whereas the integrated rock unit (IRU) represents common domains identified in each of the boreholes. 57

Table 6. Structural unit interval top and bottom depths along drilled boreholes. Mean fractures per metre and standard deviations are presented as metrics to compare the units between boreholes. Structural unit (SU) represents the interpretation domain based on the single borehole integration report, whereas the integrated structural unit (ISU) represents common domains identified in each of the boreholes. 58

Table 7. Summary statistics for integrated rock unit thicknesses derived from the model. 67

Table 8. Vertical and horizontal variogram model parameters..72

LIST OF FIGURES

Figure 1: General elements of a Descriptive Geoscientific Site Model (DGSM). 2

Figure 2: Geological setting of the Superior Province in Northwestern Ontario (after Thurston, 1991) around the Revell Regional Area (red outline on main map) and showing the outline of the Revell batholith (RB). Inset at top right shows the 1:250,000 scale outline of the Revell batholith and surrounding greenstone belts. The Winnipeg River, Marmion and western Wabigoon terranes are part of the Wabigoon subprovince. 5

Figure 3: Bedrock geology map of the Revell batholith and surrounding greenstone belts. The collar locations and planned trajectories of IG_BH01-03 are shown in the northern lobe of the batholith. 8

Figure 4: Simplified SW-NE oriented cross-section across the Revell Regional Area. Section line location is indicated on the inset map at bottom right. Refer to Figure 3 for legend to inset map. 9

Figure 5: Summary of Archean and Proterozoic geological events for the Revell Regional Area. 11

Figure 6: Water features, including lakes, rivers and wetlands, and distribution of Quaternary overburden composed of glaciolacustrine and organic deposits within the site-scale extent. The main bedrock exposed comprises Biotite Granodiorite to Granite suite. 13

Figure 7. Borehole area showing field mapping stations with identified rock type and select structural measurements. 14

Figure 8. Field examples of the plutonic rocks of the Revell batholith. (a) Typical exposure of granodiorite at outcrop scale. Yellow notebook and gamma ray spectrometer for scale. (b) Close-up of granodiorite showing mineral composition and texture. (c) Close-up of tonalite showing mineral composition and texture. (d) Typical exposure of granite at outcrop scale. (e) Close-up of granite showing mineral composition and texture. (f) Close-up of feldspar-megacrystic granite showing mineral composition and texture. 16

Figure 9. Equal-area lower hemisphere projections of poles to the planes of surface mapped planar structures, including a) foliation (N = 33), b) shear zones (N = 15), and c) fractures (N = 426), including all joints, faults and veins. Note that the shear zone dataset is not contoured due to the limited number of data points. 18

Figure 10. Field examples of Proterozoic Wabigoon dykes. (a) Typical exposure of a Wabigoon dyke covering entire field of view. (b) Close-up of fractures developed at low angle to dyke contact near its margin. 19

Figure 11. Northwest trending Wabigoon diabase dyke swarm crossing through the site-scale extent. Airborne magnetic data allowed for three separate dyke segments to be delineated (black dashed lines). Red vector symbols define the local strike and dip (with magnitude) of the dyke contact. 20

Figure 12. Topographic distribution within the site-scale extent. Topography ranges from 368 to 498 m above mean sea level for a total range of 130 m. Highest elevations exist in the central portion of the site, which broadly slopes towards the west. 22

Figure 13. RGB and NIR orthoimage of the Revell Site. Southern portion of the site consists of dense forest with mature trees, whereas the majority of the northern and western portion of the site has been deforested prior to acquiring the imagery (imagery acquired by ATLIS 2017). 23

Figure 14. Airborne magnetic data and derivative grids showing the boundary of the Revell site. A) reduced to pole, and B) first vertical derivative of the magnetic field. Northwest trending linear magnetic highs correspond to diabase dykes of the Wabigoon dyke swarm. Majority of the linear magnetic anomalies shown in the vertical derivative are interpreted as magnetite-rich sediments within water bodies and streams. 24

Figure 15. Airborne gravity data and derivative grids clipped to the boundary of the Revell site. A) Bouguer gravity field, B) first vertical derivative of gravity field. 25

Figure 16. Distribution of structural lineaments interpreted over the Revell Batholith and surrounding greenstone belt units. The thick black outline represents the extent of the site-scale model. 27

Figure 17. Comparison between lineaments interpreted from DesRoches et al (2018) and the new lineaments based on the reassessment documented in this report. 30

Figure 18. Regional-scale faults interpreted to represent first-order fracture zones in the region. Fault data comes from Ontario Geological Survey (MRD126-rev1). Solid black lines represent sub-province tectonic boundaries. 31

Figure 19. Lineaments at the Revell site presented by a) orientation set, and b) order, based on relationship with regional scale structures. Unique identifiers on the lineaments correspond to their inferred fracture zone surfaces (see section 5.5) 32

Figure 20. Pie plot showing relative rock type proportions identified within each drilled borehole. All three boreholes are dominated by biotite granodiorite-tonalite, with IG_BH01 showing in addition a high amount of biotite tonalite. 35

Figure 21. Representative samples of biotite granodiorite-tonalite (IG_BH03_LG020; a-c) and biotite tonalite (IG_BH01_LG020; d-f). a) Hand-sample showing medium grain size and massive texture. b) Thin section billet photograph; billet has been etched with hydrofluoric acid and stained with sodium cobaltinitrite, which gives potassium-bearing minerals a yellow colour (in this case, highlighting K-feldspar; billet size is 25 x 40 mm, A and B denote different grain size domains in the sample). c) Thin section photomicrograph with rock forming minerals plagioclase (pl) and quartz (qz). Minor biotite is also present, and fine-grained white mica is visible in the cores of the plagioclase grains as a secondary alteration; crossed polarizers transmitted light. d) Hand-sample showing fine-medium grain size and massive texture. e) Thin section billet photograph showing absence of yellow staining indicating no K-feldspar present in the sample (billet size is 25 x 40 mm). f) Thin section photomicrograph with rock forming minerals plagioclase (pl), quartz (qz), and biotite (bt), fine-grained white mica is visible in the cores of the plagioclase grains as a secondary alteration; crossed polarizers transmitted light. 36

Figure 22: Chondrite-normalized rare-earth element (REE) plot (after Taylor and McLennan, 1985) of 8 of the rock types logged in BH01-03 and a representative average of 2.8 Ga low-heavy REE (low-HREE) tonalite-trondhjemite-granodiorite (TTG) from the Fennoscandian shield (open diamonds; Halla et al., 2009; Halla, 2018). The y-axis shows concentrations (expressed as logarithm to the base 10 of the value) of REE (x-axis, by atomic number) in our samples normalized to a reference chondrite standard. 37

Figure 23: Representative examples of amphibolite (sample IG_BH03_LG010). A) Hand-sample photograph B) Billet photograph (billet size is 25 x 40 mm). C) Thin section photomicrograph with main rock-forming minerals amphibole (am; tremolite-actinolite), biotite (bt) and epidote (ep); plane polarized transmitted light. 39

Figure 24. Amphibolite contact orientations from both upper and lower unit contacts. Orientations are defined by sinusoid trace using oriented televiewer images. Although there is a spread of contact orientations, the poles produce a tight cluster with a mean plane that dips 30º towards 348º...40

Figure 25. Representative samples of feldspar-phyric tonalite (IG_BH03_LG005; a-c) and aphanitic tonalite (IG_BH02_LG010; d-f) dykes. a) Hand-sample showing dark grey aphanitic matrix and visible mm-size albite phenocrysts. b) Thin section billet photograph showing foliation in groundmass wrapping phenocrysts. Billet has been etched with hydrofluoric acid and stained with sodium cobaltinitrite, which gives potassium-bearing minerals a yellow colour (interpreted as fine-grained K-feldspar, in this case; billet size is 25 x 40 mm). c) Thin section photomicrograph with 2-3 mm plagioclase phenocrysts (pl) and aphanitic groundmass composed of quartz, plagioclase, and biotite (qz+pl+bt). Groundmass foliation wraps the phenocrysts; crossed polarizers transmitted light. d) Hand-sample showing dark grey aphanitic groundmass and no visible phenocrysts. e) Thin

section billet photograph showing small plagioclase phenocrysts and very minor yellow staining of K-feldspar (billet size is 25 x 40 mm). f) Thin section photomicrograph shows slightly coarser grain size in groundmass compared to c) and small 0.5 – 1.5 mm plagioclase phenocrysts (pl). Groundmass is composed of plagioclase, quartz, and biotite (pl+qz+bt) and foliation is not present in this sample; crossed polarizers transmitted light. 42

Figure 26. Aphanitic and feldspar-phyric tonalite dyke contact orientations from both upper and lower unit contacts. Orientations are defined by sinusoid trace using oriented televiewer images. Although there is a spread of contact orientations, the poles produce a tight cluster with a mean plane that dips 27º towards 047º. 43

Figure 27. Representative samples of aplite (IG_BH01_LG018; a-c) and granite (IG_BH03_LG015; d-f) dykes. a) Hand-sample showing very fine grain size and white-grey colour. b) Thin section billet photograph showing massive texture and very fine grain size. Billet has been etched with hydrofluoric acid and stained with sodium cobaltinitrite, which gives potassium-bearing minerals a yellow colour (in this case, K-feldpsar; billet size is 25 x 40 mm). c) Thin section photomicrograph with rock forming minerals plagioclase (pl), quartz (qz), and K-feldspar (af). Note the fresh look of the minerals compared to the host biotite granodiorite-tonalite; crossed polarizers transmitted light. d) Hand-sample showing medium grain size and pink colour. e) Thin section billet photograph showing massive texture and medium grain size. Billet has been etched with hydrofluoric acid and stained with sodium cobaltinitrite, which gives potassium-bearing minerals a yellow colour (in this case, K-feldpsar; billet size is 25 x 40 mm). f) Thin section photomicrograph with rock forming minerals plagioclase (pl), quartz (qz), and K-feldspar (af). Note the larger grain size compared to the aplite dyke and the fresh look of the minerals compared to the host biotite granodiorite-tonalite; crossed polarizers transmitted light. 44

Figure 28. Aplitic and granitic dyke contact orientations from both upper and lower unit contacts. Orientations are defined by sinusoid trace using oriented televiewer images. Although there is a spread of contact orientations, the poles produce a tight cluster with a mean plane that dips 43º towards 015º...45

Figure 29. Fracture count per metre calculated in boreholes IG_BH01, IG_BH02 and IG_BH03. Frequency is based the integration of core logged and televiewers logged structures. The term fracture refers to joints, veins and faults. Position is along the borehole axis............46

Figure 30. Stereonet of poles to fracture planes (joint, vein and fault) from three boreholes; IG_BH01, IG_BH02, IG_BH03 combined. (a) distributions of poles with contoured pole density, and (b) distributions of poles with Terzaghi-weighted pole densities contoured. Black dashed outlines present general clusters for the purpose of discussion in the report; detailed cluster analyses will be completed in a separate report. 47

Figure 31. Compilation of poles for primary igneous and ductile planar structures from the first three boreholes (IG_BH01, IG_BH02, and IG_BH03). Unweighted data is shown on the left and Terzaghi-weighted data is shown on the right. a) Igneous primary structure which represents primary layering recognized in the bedrock; b) foliation defined by weak to moderate biotite alignment within the biotite granodiorite-tonalite unit or by aligned amphiboles in amphibolites; and c) shear zones categorized as either brittle-ductile or ductile (SHR and SHRD) plus a few logged mylonite (MYL) occurrences. 49

Figure 32: Compilation of lineations (n=275) from the first three boreholes (IG_BH01, IG_BH02, and IG_BH03). 51

Figure 33. High fracture frequency intervals interpreted visualized with cumulative fracture logs for boreholes IG_BH01, IG_BH02, and IG_BH03. High fracture frequency intervals (HFFI) are outlined by their yellow bands. The red dashed line represents the peak location. 52

Figure 34. Vertical frequency of subhorizontal fractures per 5 metre interval calculated in boreholes IG_BH01, IG_BH02 and IG_BH03. Subhorizontal fractures here are defined with dip magnitudes ranging between 0 and 30 degrees. Frequency is based the integration of core logged and televiewers logged structures. The term fracture refers to joints, veins and faults. Depth is along the borehole axis. 54

Figure 35. Normalized cumulative fracture count, the fracture frequency, and the moving average fracture frequency for the subhorizontal fractures from IG_BH02. Subhorizontal fractures here are defined with dip magnitudes ranging between 0 and 30 degrees. Frequency is based the integration of core logged and televiewers logged structures. The term fracture refers to joints, veins and faults. Depth is along the borehole axis. Five subhorizontal fracture frequency intervals have been identified (yellow) 55

Figure 36. Borehole view showing vertical distribution of a) IRU and b) ISU model domains (bins of low, medium and high represent fracture intensity groupings based on mean fracture counts). 57

Figure 37. Current conceptual understanding of site-scale bedrock geology based on integrated geological and geophysical data from surface and initial three boreholes. The main rock type is biotite granodiorite-tonalite and is intruded by various suites of high-angle felsic dykes, and moderately dipping amphibolites. Bedrock can be subdivided into rock unit domains based on intervals identified in single borehole integration reports. Rock unit subdivisions are largely based on presence, or a relative absence, of (a) gently inclined and north-dipping amphibolite occurrences throughout the bedrock. Relatively pervasive alteration is present along the shallow fractured subsurface (upper ~100 m) and is hypothesized to collocate along the ((b) and (c)) near vertical fracture zones associated with interpreted lineaments. Subhorizontal fracture zones (d) tend to be identified in

borehole logs at various depths. e) presents a hypothetical borehole log through the conceptualized model. The borehole shows the shallow fracture zone near the ground surface with weak alteration, intersection of amphibolite units, and a near vertical fracture zone with alteration. 60

Figure 38. Extent of the site-scale model. a) model outline on simplified bedrock geology. Pale grey shows the Revell batholith and dark grey shows the surrounding greenstone belt; b) model boundaries in 3D oblique view. 62

Figure 39. Modelling workflow followed to develop a site-scale geological model. a) includes the review and preparation of geoscientific data, b) input of prepared data into surface-based and voxel-based modelling approaches, c) output of integrated rock unit, integrated structural unit, and inferred fracture zone models, and d) review of each model component. 63

Figure 40. Surface-based modelling workflow used to interpolate rock unit domain boundaries between boreholes to develop the Integrated Rock Unit (IRU) model. 65

Figure 41. Surface based representation of geological domain boundaries subdividing the integrated rock units and crossing through borehole markers. Borehole markers are defined based on the rock units identified in the single borehole integration reports. 67

Figure 42. Vertical thickness of the integrated rock units. A) IRU1a, B) IRU3, and C) IRU1b. IRU3 represents the biotite granodiorite-tonalite with the inclusion of approximately 5 percent amphibolite. 67

Figure 43. Voxel representation of the integrated rock unit model. IRU1a and IRU1b present predominantly biotite granodiorite-tonalite with subordinate narrow felsic dykes, and IRU3 represents a similar biotite granodiorite-tonalite with felsic dykes and the addition of approximately 5% amphibolite. 68

Figure 44. Voxel-based modelling workflow used to interpolate structural unit domains in the model extent and develop the Integrated Structural Unit (ISU) model. 70

Figure 45. Schematic diagram of data representation as (a) indicator values along decomposited borehole as points, (b) upscaled indicator values to grid cells based on most probable, (c) indicator interpolated on a 2D view, and (d) indicator interpolated on a 3D grid view 70

Figure 46. Vertical semi-variogram model fitted to the composited borehole log for the High structural unit indicator. 72

Figure 47. Integrated structural unit (ISU) model showing High, Medium, and Low domains. Bins of High, Medium, and Low represent fracture intensity domains based on mean fracture counts. Domains were estimated by ordinary Indicator Kriging (IK), honouring composited borehole structural units at 10 m intervals, and the variogram model. Due to a sparse distribution of boreholes, the horizontal variogram was approximated to allow the integrated structural unit boundaries to be smooth and laterally continuous across the entire model extent (with a 10:1 horizontal to vertical ratio used to assign the horizontal range)............73

Figure 48. Three example realizations of the integrated structural unit model showing High, Medium, and Low domains shown in a), b) and c). A total of 25 realizations were simulated. Using all realizations d), e) and f) show the probability distributions for the Low, Medium and High indicator for each model cell. 75

Figure 49. Integrated structural unit model showing High, Medium, and Low domains. Domains were simulated using the sequential Indicator simulation (SIS) with ordinary Kriging (IK) algorithm, honouring composited borehole structural units at 10 m intervals, and a vertical variogram model. Due to a sparse distribution of boreholes, the horizontal variogram was approximated to allow integrated structural unit boundaries to be smooth and laterally continuous across the entire model extent (with a 10:1 horizontal to vertical ratio used to assign the horizontal range). SIS results provide multiple probable realizations (n=25) and allow the model to incorporate some degree of spatial heterogeneity in the distribution of units. 75

Figure 50. Relative structural unit proportions presented in the composited borehole log, and as a result of indicator estimation and simulations. Estimation and simulation results perform well at simulating the relative proportions of each structural unit in the model. 76

Figure 51. Compilation of the integrated structural unit models showing High, Medium, and Low domains. Estimation (a) and simulation (b) results are overprinted with an interpreted continuous shallow fracture zone based on a mean thickness of 53.5 m over the entire site-scale model domain. 77

Figure 52. Workflow for modelling lineament traces as 3D inferred fracture zone surfaces. 80

Figure 53. Spatial distribution of deterministically modelled inferred fracture zones in top view categorized in a) by order; and in b) by orientation set. Inferred fracture zones extend from ground surface to a depth equal to their total trace length (1:1 length to depth ratio). Unique identifier labels for each IFZ are displayed on Figure 20...81

Figure 54. Stereonet plots of fracture orientations within the correlated high fracture frequency intervals...84

Figure 55. Lineament fracture zones IFZ050, IFZ051 and IFZ072 intersected by IG_BH02. a) presents an oblique view looking towards the NW at the fracture zones, and b) shows the top-view of the fracture zones. Black line shows the path of IG_BH02. 86

Figure 56. Lineament fracture zones IFZ044 and IFZ071 intersected by IG_BH03. a) presents an oblique view looking towards the NE at the fracture zones, and b) shows the top-view of the fracture zones. Black line shows the path of IG_BH03. 88

Figure 57. Interpreted subsurface projection of inferred fracture zone IFZ012 based on field fracture mapping orientations. a) lineament trace and fracture orientations in proximity to the trace. Field data are filtered to include only those fractures with strikes ±45º degrees of lineament trend, and dips greater than 45º. Filtered fracture orientations are transferred to lineament trace by neighbourhood search of 2000 m to generate a smooth dip and strike geometry. b) surface lineament trace projected into the subsurface using a gripframe from the GSC/Mira sparse module. c) final triangulated surface is interpolated through the gripframe representing the best-fit subsurface geometry of the inferred fracture zone based on proximal fracture orientations. 89

Figure 58. Oblique view of IFZ012 fracture zone looking towards the northwest. IFZ012 has a mean dip of 84º ±3.2º and a mean strike of 316º ±26º (mean dip direction of 46º).............90

Figure 59. Wabigoon diabase dykes interpreted from airborne magnetic data and field mapping are represented as vertically projected surfaces. All dykes extend from ground surface to the base of the model domain. 91

Figure 60. Voxelized integrated rock unit model overprinted with Wabigoon diabase dykes......92

Figure 61. Voxelized integrated structural unit model based on a) indicator kriging and b) indicator simulation. Each model is overprinted with inferred fracture zone model............92

Figure 62. Uncertainty metric quantified by log distance to measured and interpreted input data. Metric indicates regions of the model that have a higher or lower degree of data density..94

1. Introduction

Geological models in the context of this study constitute three-dimensional approximations of the subsurface. The subsurface can be partitioned into discrete or continuous property distributions with a complex spatial arrangement or can be classified into broad domains that reflect regions of the subsurface with similar characteristics. The resulting models attempt to honour the complexity of the subsurface while maintaining the ability to develop the model with a small glimpse of the subsurface through borehole drilling and other geophysical investigations. These models can be used to better understand the spatial arrangement of a site in terms of structural and lithological complexity and can be further queried to assist with planning subsequent field studies. Furthermore, the results from the site framework can be used in subsequent geoscientific disciplinary studies (e.g., hydrogeological, geomechanical, thermal, etc).

This report presents an initial three-dimensional (3D) geological model based on the use of three cored boreholes and a compilation of field mapping data for a site within the central portion of the northern lobe of the Revell batholith. The site is located northwest of the community of Ignace and southeast of Wabigoon Lake Ojibway Nation, in northwestern Ontario. The Revell batholith is a body of plutonic rock that was previously identified by the Nuclear Waste Management Organization (NWMO) as being potentially suitable for hosting a deep geological repository (NWMO, 2013). The northern part of the Revell batholith was subsequently selected for further investigation (NWMO, 2015) and is currently in Phase 2 of NWMO's Adaptive Phased Management (APM) Site Selection Phase.

The surface portion of the 3D geological model presented herein is based on a two-dimensional (2D) representation of the bedrock geology for the Revell batholith, including the surface trace of Proterozoic dykes that transect the model volume (Parmenter et al., 2020), and available information regarding water bodies and Quaternary overburden and topography. The subsurface portion of the 3D geological model is based on the geological and geophysical information described in single borehole geological interpretation reports from drilling of three deep boreholes IG_BH01 (Parmenter et al., 2021a), IG_BH02 (Parmenter et al., 2021b), and IG_BH03 (Parmenter et al., 2021c). Additional geological elements integrated into this initial 3D geological model include an updated representation of structural lineaments, based upon a previous regional scale interpretation (DesRoches et al., 2018 and updated in this report), and herein projected into the subsurface as zones within the 3D model.

1.1 Scope and Objectives

This report presents the initial development of a site-scale 3D geological model within the central portion of the northern lobe of the Revell batholith. The report describes the use of the geoscientific datasets as inputs and summarizes the modelling approaches. The main objective of the report and the geological model is to build a numerical representation of the subsurface that can be further used to evaluate the potential of the site to host a deep geological repository. Results from the geological model form the site framework to be used in associated geoscientific studies to develop discipline-specific sub-models, including geomechanical, thermal, hydrogeological, hydrogeochemical, and transport (petrophysical) property models. The geological model, along with these additional sub-models, will be described in a Descriptive Geoscientific Site Model (DGSM) report. The discipline-specific models and the overall inter-dependencies between all of these models and the geological framework model, within the DGSM, are illustrated in Figure 1. The key message represented in Figure 1 is the critical role of the geological framework model in developing all other associated sub-models.

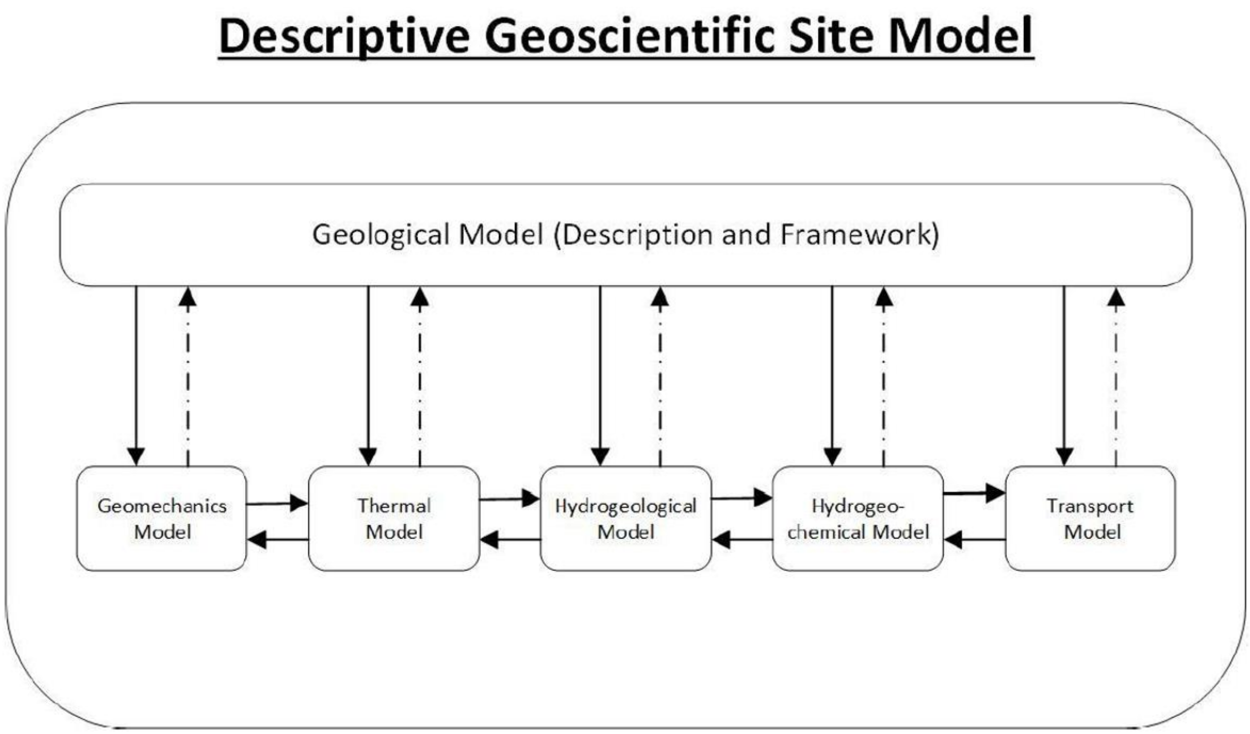

Figure 1: General elements of a Descriptive Geoscientific Site Model (DGSM).

1.2 Model Version and Data Freeze

The site-scale geological model version v1.0 has been developed based on select geoscientific data compiled from NWMO Phase 1 and Phase 2 studies up until the end of 2020. This report documents the initial version of the Revell site-scale 3D geological model. Results from this model will be referred to as Model v1.0. After finalizing this report, minor modifications to the results will be appended to this report and the model version will be updated as v1.1, and v1.2, and so on.

A data freeze has been implemented in the development of the model to organize and control the use of quality-assured geoscientific data, which represents the currently acquired geoscientific data for a defined period of time. During the period in which the model is being developed, site characterization and data collection activities continue in parallel. The data used in the initial site-scale model has undergone QA review, and has been stored on the NWMO geoscience data management system.

The introduction of new geoscientific data following a data freeze will be included in short periods of time to limit the amount of new data. New data may include, for example, additional drilled boreholes with associated geoscientific data and test results. Decisions around the timing, and types of additional geoscientific data to include into the model will be justified and documented in new versions of the model (e.g. v1.2, and v1.3). The development of a new model, which would be accompanied by a new report, will include a new version number as v2.0.

The decision to implement a data freeze will be identified at stages when a model is required to support milestone decisions, such as safety assessment and repository design requirements, planning for borehole targeting and mapping activities, and development of geoscientific site model.

1.3 Terminology

Rock unit: Initially defined based on a borehole length comprising a dominant rock type and/or a combination of rock types (and, if applicable, alteration and weathering types) that are considered distinct from adjacent parts of the borehole. Each rock unit is uniquely labelled and can be repeated with a sub-label at different depths if appropriate.

Structural unit: A borehole length comprising a relatively uniform per metre fracture frequency that is distinct from adjacent parts of the borehole. Each structural unit is uniquely labelled and can be repeated with a sub-label at different depths if appropriate.

High fracture frequency interval (HFFI): A cluster of fractures (i.e., faults, joints and/or veins) that exceeds a minimum relative fracture intensity threshold along a distinct borehole length.

Zone: A localized region of more closely spaced brittle and/or ductile structures defining an approximately tabular region with its smallest dimension (thickness) much less than the other two directions (strike dimension and dip dimension, respectively). The zone may be defined based on exceedance of a minimum relative intensity threshold or exceedance of a defined per metre frequency (P10) threshold.

Fracture zone: A zone that is defined only by brittle deformation features (i.e., faults, joints and/or veins).

Inferred fracture zone: A localized region of closely spaced fracturing that is interpreted to have an approximately tabular geometry. It may represent the extrapolation of a surface traced lineament into the subsurface, or the extension of a high fracture frequency interval away from a borehole.

Brittle-ductile deformation zone: A zone that is defined by both brittle and ductile deformation features. This type of zone may have either formed in the brittle-ductile regime OR may represent a previously formed ductile zone that has been reactivated in the brittle regime.

Ductile deformation zone: A zone that is defined only by ductile deformation features (i.e., protomylonitic, mylonitic and/or ultramylonitic fabrics).

1.4 Software

SKUA-GOCAD™ was used for visualization and development of the site-scale 3D Geological Model. This software is developed by Paradigm (now part of Emerson Paradigm LLC) and is coupled with the Integrated Modeling module as a part of the GOCAD® Mining Suite developed by Mira Geoscience Ltd. Model outputs can be exported and visualized in Mira Geoscience Analyst software (free viewer) to allow users to visualize and query the model. ArcGIS and QGIS were used to develop 2D maps presented as figures in this report. A single Python script was written to post-process the results from geostatistical indicator simulation to combine the realizations as a 3D ensemble presenting the indicator probabilities and the expected indicator value.

2. Summary of Geology

2.1 Geological Setting

The geological setting for the Revell batholith and surrounding area is described in detail in Parmenter et al. (2020) and is briefly summarized below.

The Revell Regional Area is situated in the northwestern part of the Superior Province of the Canadian Shield – a stable craton created from a collage of ancient plates and accreted juvenile arc terranes that were progressively amalgamated over a period of more than 2 billion years (Figure 2). The Canadian Shield forms the stable core of the North American continent. The Superior Province has historically been divided into various regionally extensive east-northeast-trending subprovinces based on rock type, age and metamorphism (Thurston, 1991). More recently, the Superior Province has been subdivided into lithotectonic terranes, defined as tectonically bounded regions with characteristics distinct from adjacent regions prior to their accretion into the Superior Province (Percival and Easton, 2007; Stott et al., 2010). The Revell Regional Area is situated in the south-central part of the western Wabigoon terrane, adjacent to the boundary with the Marmion terrane (Figure 2).

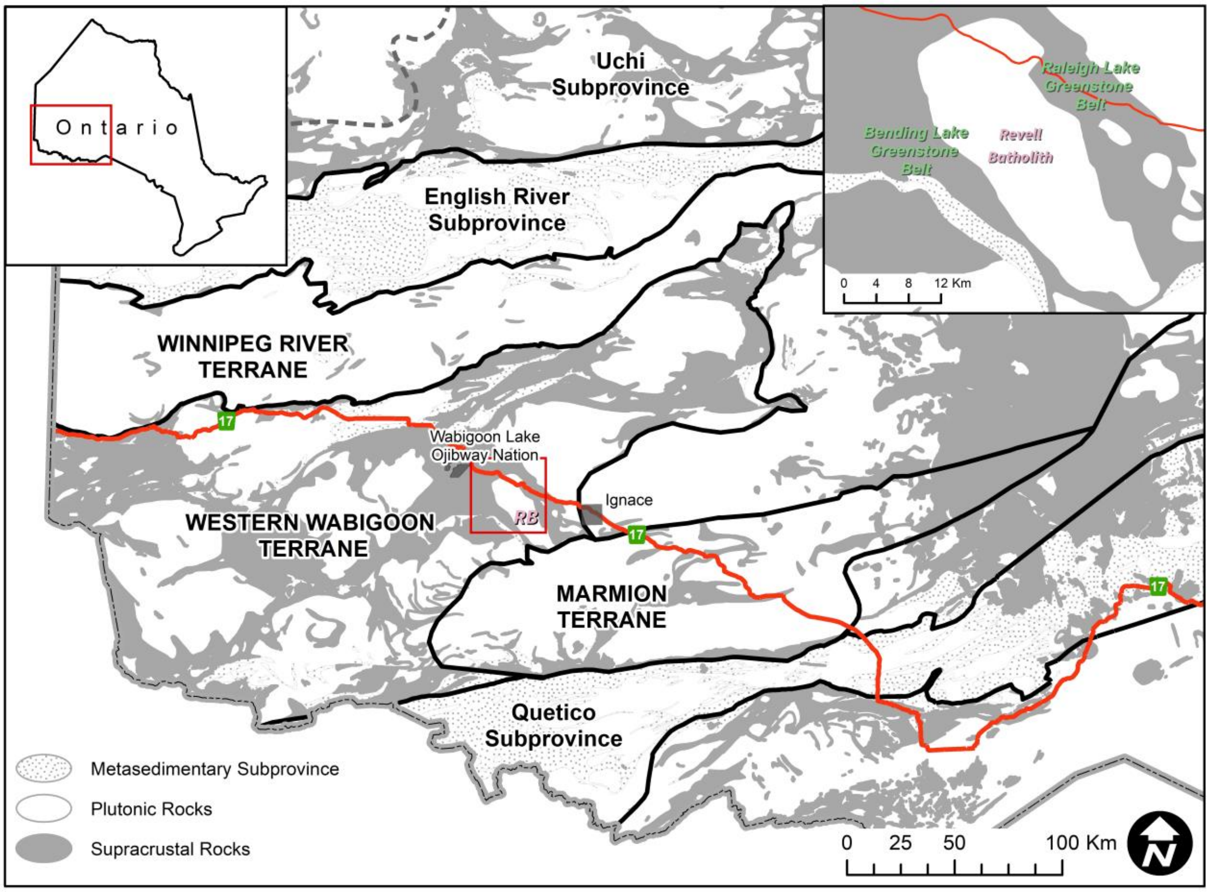

Figure 2: Geological setting of the Superior Province in Northwestern Ontario (after Thurston, 1991) around the Revell Regional Area (red outline on main map) and showing the outline of the Revell batholith (RB). Inset at top right shows the 1:250,000 scale outline of the Revell batholith and surrounding greenstone belts. The Winnipeg River, Marmion and western Wabigoon terranes are part of the Wabigoon subprovince.

The western Wabigoon terrane, interpreted to represent a volcanic island arc, is predominantly composed of two main groups of rock. This includes ca. 2.745 to 2.711 Ga supracrustal rocks, comprising Archean mafic to intermediate to felsic metavolcanic rocks and subordinate sedimentary rocks distributed in greenstone belts, and ca. 2.70 to 2.67 Ga rocks of granitoid affinity predominantly consisting of felsic plutonic rocks. These two major rock groups are a common characteristic of granite-greenstone belts and granite-greenstone subprovinces across the entire western Superior province.

The Archean supracrustal rocks in the Revell Regional Area wrap entirely around the northern margin of the Archean Revell batholith (Figure 2). The supracrustal rocks distributed to the southwest of the batholith belong to the Bending Lake greenstone belt and those distributed to the northeast of the batholith belong to the Raleigh Lake greenstone belt. Both of these greenstone belts, as well as the additional supracrustal rocks wrapping around the northern boundary of the batholith, represent contiguous parts of the Kakagi Lake-Savant Lake greenstone belt that underlies the entire western Wabigoon terrane. Five main rock units are identified in the supracrustal rock group: mafic metavolcanic rocks, intermediate to felsic metavolcanic rocks, metasedimentary rocks, iron formation, and mafic intrusive rocks (Figure 3). Sedimentation within the supracrustal rock assemblage was largely synvolcanic, although sediment deposition in the Bending Lake area may have continued past the volcanic period (Stone, 2009; Stone, 2010a; Stone, 2010b). All supracrustal rocks are affected, to varying degrees, by penetrative brittle-ductile to ductile deformation under greenschist- to amphibolite-facies metamorphic conditions (Blackburn and Hinz, 1996; Stone et al., 1998). In some locations, primary features, such as pillow basalt or bedding in sedimentary rocks are preserved, in other locations, primary relationships are completely masked by penetrative deformation. Uranium-lead (U-Pb) geochronological analysis of the supracrustal rocks produced ages that range between 2734.6 +/-1.1 Ma and 2725 +/-5 Ma (Stone et al., 2010).

The Revell batholith is roughly rectangular in shape, trends northwest, is approximately 40 km in length, and covers an area of approximately 455 km^2 (Figure 2). Three main suites of plutonic rock are recognized in the Revell batholith, including, from oldest to youngest: biotite tonalite to granodiorite suite, a hornblende tonalite to granodiorite suite, and a biotite granite to granodiorite suite (Figure 3). Plutonic rocks of the biotite tonalite to granodiorite suite occur along the southwestern and northeastern margins of the Revell batholith. The principal type of rock within this suite is a white to grey, medium-grained, variably massive to foliated or weakly gneissic, biotite tonalite to granodiorite. One sample of foliated and medium-grained biotite tonalite produced a U-Pb age of 2734.2+/-0.8 Ma (Stone et al., 2010). The hornblende tonalite to granodiorite suite occurs in two irregularly shaped zones surrounding the central core of the Revell batholith. Rocks of the hornblende tonalite to granodiorite suite range compositionally from tonalite through granodiorite to granite and also include significant proportions of quartz diorite and quartz monzodiorite. One sample of coarse-grained grey mesocratic hornblende tonalite produced a U-Pb age of 2732.3+/-0.8 Ma (Stone et al., 2010). Rocks of the biotite granite to granodiorite suite underlie most of the northern, central and southern portions of the Revell batholith. Rocks of this suite are typically coarse-grained, massive to weakly foliated, and white to pink in colour. The biotite granite to granodiorite suite ranges compositionally from granite through granodiorite to tonalite. A distinct potassium (K)-feldspar megacrystic granite phase of the biotite granite to granodiorite suite occurs as an oval-shaped body in the central portion of the Revell batholith (Figure 3). One sample of coarse-grained, pink, massive K-feldspar megacrystic biotite granite produced a U-Pb age of 2694.0+/-0.9 Ma (Stone et al., 2010).

West-northwest trending mafic dykes interpreted from airborne magnetic data extend across the northern portion of the Revell batholith and into the surrounding greenstone belts. One mafic dyke occurrence is approximately 15-20 m wide (Figure 3). All of these mafic dykes have a similar character and are interpreted to be part of the Wabigoon dyke swarm. One sample from the same Wabigoon swarm produced a U-Pb age of 1887+/-13 Ma (Stone et al., 2010), indicating that these mafic dykes are Proterozoic in age. Based on surface measurement, it is assumed that these mafic dykes are sub-vertical (Golder and PGW, 2017).

Szewczyk and West (1976) interpreted the Revell batholith to be a sheet-like intrusion that is approximately 1.6 km thick. More recent 2.5D gravity modelling suggested that the batholith is on the order of 2 km to 3 km thick through the center of the northern part of the batholith (SGL, 2020). SGL (2020) subsequently completed a 3D geophysical model of the Revell batholith by incorporating information on bedrock unit distributions, structural geometries, and petrophysical properties. The 3D model presents the batholith with a relatively flat base that extends to depths of nearly 4 km in some regions. The batholith is encapsulated within surrounding mafic metavolcanic rocks and felsic to intermediate metavolcanic rocks, referred to broadly as the greenstone unit. The biotite granite to granodiorite suite has a well-defined density (mean of 2.65 ± 0.05 g/cc), which is the lowest of the four rock units inside the Revell batholith and dominates the 3D model and the gravity signature of the batholith. The biotite granite to Granodiorite suite has been modelled with a nearly flat base at a depth around 2 km extending over most of the batholith. A model assigning the same density as that of the biotite granite to granodiorite suite at 2.65 ± 0.05 g/cc to all the batholith phases in the model gave total thickness extending to 3km in most regions. This model was used to set a lower limit to the thickness of the entire batholith. Incorporating the denser biotite tonalite to granodiorite and hornblende tonalite to granodiorite suites as distinctive units in the model has the effect of increasing the batholith overall thickness while raising the base of the biotite granite to granodiorite suite.

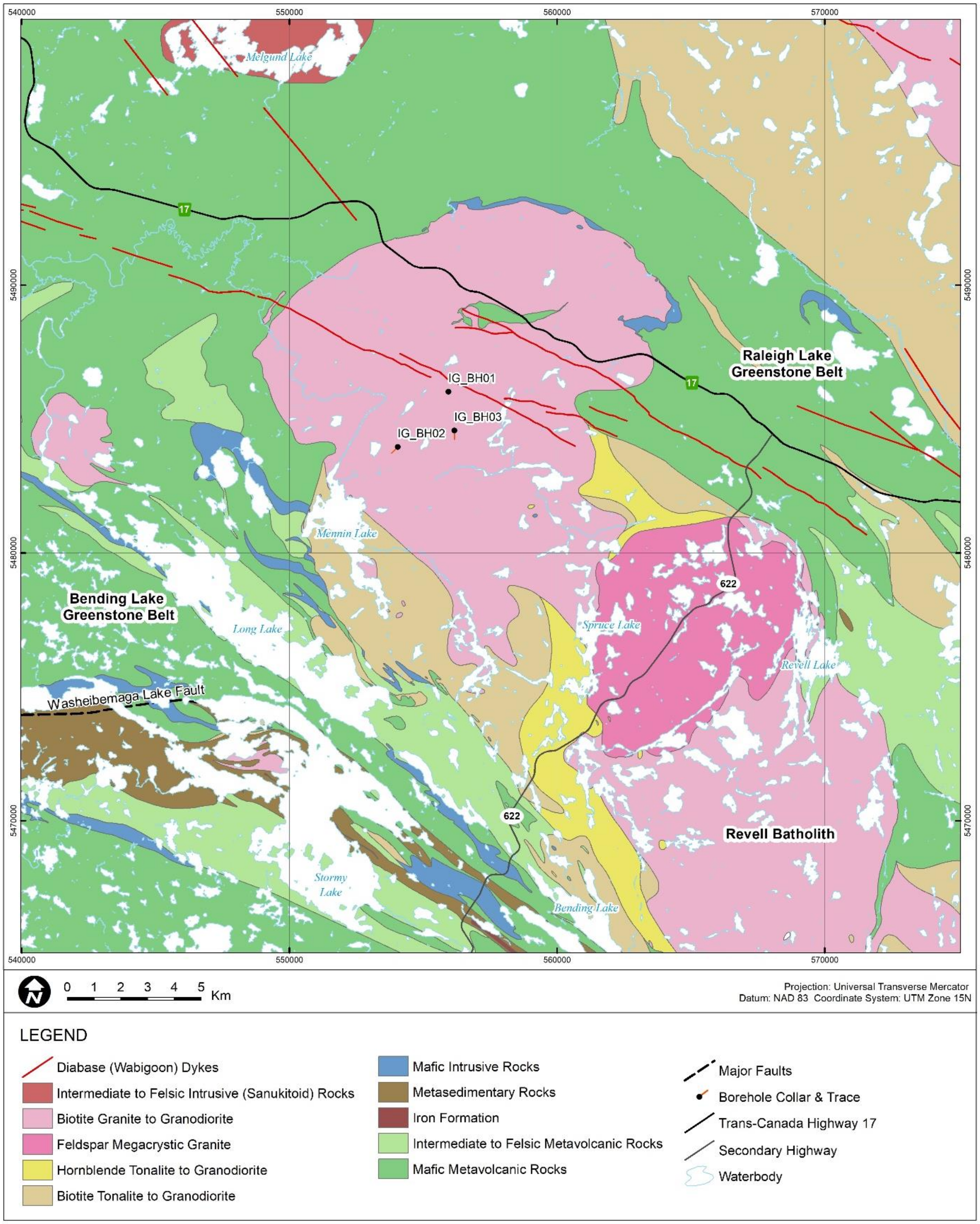

Figure 3: Bedrock geology map of the Revell batholith and surrounding greenstone belts. The collar locations and planned trajectories of IG_BH01-03 are shown in the northern lobe of the batholith.

A simple conceptual cross-section (Figure 4), based on the results from the gravity modelling of SGL (2020), is presented below for a northeast-trending section line through the northern lobe of the Revell batholith (Parmenter et al., 2020). The orientation of the section line is perpendicular to the long axis of the batholith and also to the main northwest-trending fabric orientation in the surrounding greenstone belts. In the cross-section, the near-surface orientation of the southwest and northeast contacts between the supracrustal rocks and the southwest margin of the batholith are, in dip and dip direction notation, 61° towards 223° and 75° towards 221°, respectively. In the deeper subsurface, the batholith is given a generally tabular shape (e.g., Cruden, 1998). The SGL (2020) interpretation also suggests the presence of a slight inflection in the slope of the base of the batholith towards its northeast margin, which has been reflected in the section shown here. The Wabigoon dykes are represented as vertical lines where crossed by the section. Some uncertainty remains regarding the type(s) of rock that occur below the base of the batholith.

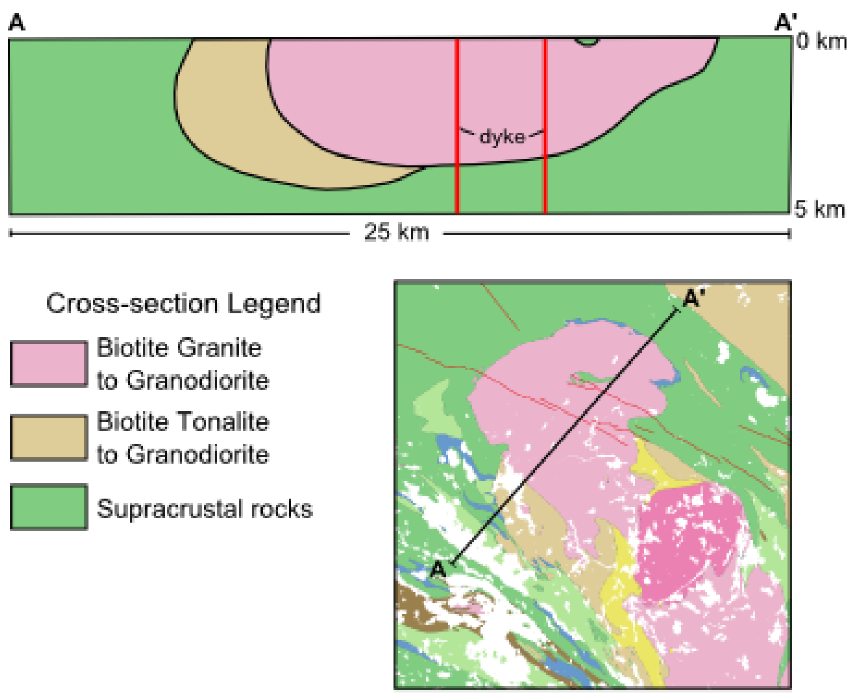

Figure 4: Simplified SW-NE oriented cross-section across the Revell Regional Area. Section line location is indicated on the inset map at bottom right. Refer to Figure 3 for legend to inset map.

2.2 Structural and Metamorphic History

A summary of the Archean and Proterozoic geological events that have shaped the bedrock in the Revell Regional Area is presented in Table 1 and shown schematically in Figure 5. This information is based on a synthesis of results from studies undertaken across the Wabigoon Subprovince (e.g., Percival et al., 2004; Bethune et al., 2006; Sanborn-Barrie and Skulski, 2006; Stone, 2010a). It is acknowledged that there is some uncertainty in applying the results from a regional synthesis to the Revell Regional Area.

The collision between the western Wabigoon terrane and the Marmion-Winnipeg River terrane at 2.7 Ga is interpreted to have coincided with the peak of regional metamorphism of the western Wabigoon terrane (Easton, 2000). A greenschist- to amphibolite-facies metamorphic overprint is widespread in the Raleigh Lake greenstone belt with the highest-grade metamorphic overprint indicated by numerous amphibolite and garnetiferous layers and clasts in the metavolcanic rocks (Blackburn and Hinz, 1996). In the Bending Lake greenstone belt, mineral assemblages are generally indicative of low to medium grade greenschist-facies metamorphism. Kresz (1987) identified a thermal metamorphic overprint that extends up to 1.5 km away from the western contact between the Revell batholith and the adjacent supracrustal rocks. This contact metamorphism, caused by the emplacement of the batholith, caused recrystallization that destroyed earlier fabrics in the bedrock. The metamorphosed rocks are now, typically, massive hornfels. Distal to the pluton, albite-epidote hornfels is characteristic, whereas proximal to the pluton, the presence of hornblende suggests lower hornblende hornfels facies (Kresz, 1987). Similar contact metamorphism was documented by Satterly (1960) and Stone (2010a) from other locations proximal to the margin of the Revell batholith.

Table 1: The Archean and Proterozoic structural and metamorphic history of the Revell Regional Area, summarized by time, and based on a sequence of deformation events established regionally. See also schematic summary of events shown in Figure 5.

Age (Ga)	Geological Event (Deformation event)	Reference(s)
2.93-2.87	Marmion and Winnipeg River terrane collision; this part of the evolving Superior Province was amalgamated into the Winnipeg River-Marmion terrane	Tomlinson et al., 2004
2.725-2.71	Ductile deformation recognized in gneissic rocks within the western Wabigoon terrane (D1-D2). However, studies that were focused in the greenstone belts did not recognize any fabrics related to the D1-D2 event.	Sanborn-Barrie and Skulski, 2006
2.745-2.711	Supracrustal rocks (D1-D4)	
2.71-2.70	Western Wabigoon terrane collision with Marmion-Winnipeg River terrane (D1-D4)	
2.70-2.67	Plutonic rocks; peak metamorphism (D3-D5; 2.70 Ga)	
>2.698	Regional penetrative deformation (D3-D4; D1-D2 of Sanborn-Barrie and Skulski, 2006) finished prior to 2.698 Ga; characterised by the development of F3 northwest-trending folds and an associated S3 axial planar cleavage. D4 east- to northeast-striking structures locally overprint the northwest-striking S3 foliation. An S4 foliation occurs as a moderately- to strongly developed, steeply-dipping, schistosity.	Percival et al., 2004
2.69-2.4	Development of regional-scale conjugate shear zones in plutonic and gneissic rocks (D5). These shear zones are associated with significant sinistral strike-slip displacement along northeast-trending	Davis, 1989; Brown, 2002; Percival et al., 2004; Sanborn-Barrie

	structures and dextral strike-slip motion along east- to east-southeast-trending structures. The D5 event spanned the transition between ductile and brittle deformation into a poorly constrained and protracted series of episodic events that continued until approximately 2.4 Ga.	and Skulski, 2006; Bethune et al., 2006; Hanes and Archibald, 1998
1.947-1.887	Episodic re-activation of pre-existing structures across the region (D6)	Kamineni et al., 1990
1.887	Emplacement of Proterozoic Wabigoon dykes (D6)	Stone et al., 2010
1.150-1.130	Rifting and intrusion associated with Midcontinent Rift magmatism (D6)	Heaman and Easton, 2006; Easton et al., 2007
Post-1.13	A complex interval of erosion, brittle fracture, repeated cycles of burial and exhumation.	e.g., Brown et al., 1995

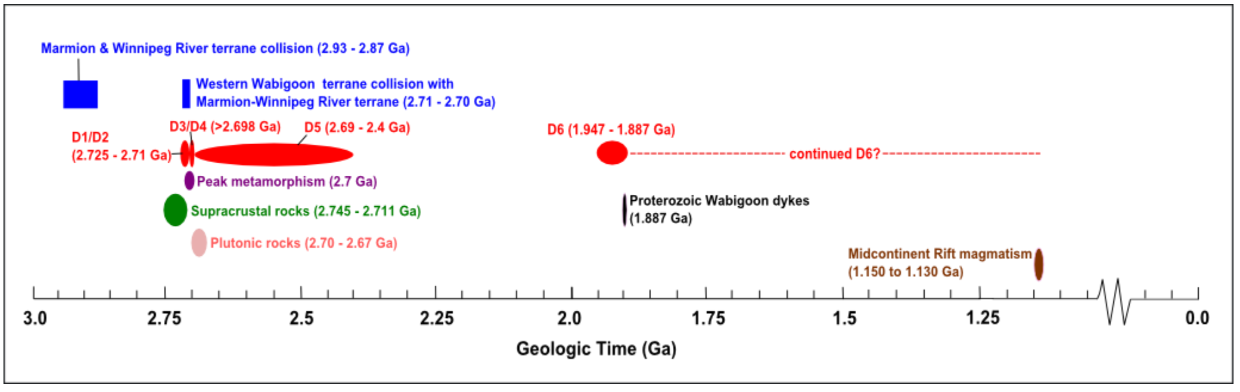

Figure 5: Summary of Archean and Proterozoic geological events for the Revell Regional Area.

3. Model Inputs

Geoscientific data is used in the development of the 3D site-scale geological model within the northern lobe of the Revell batholith. The data sets chosen can be classified as direct inputs, which are imported into the model and used to constrain and guide the interpolation and extrapolation workflows, and other geoscientific and surficial data sets that are used indirectly to enhance our conceptual understanding of the site. The following section describes each of the chosen data sets which forms the initial foundation of the site-scale model.

3.1 Water Features and Overburden Cover

Both water features and overburden cover mask the bedrock and make continuous interpretation of bedrock structures and lithology difficult (Figure 6). Water features within the site-scale model are evaluated as a digital data set of lakes, wetlands, and streams and rivers. Information is obtained from Land Information Ontario as polyline and polygon geometries.

Within the model, nodes to all lakes, wetlands, streams and rivers are densified to a maximum node spacing of 10 m and each object is draped onto the topographic surface.

Overburden cover is incorporated into the model as GIS shapefiles consisting of spatial coverage and overburden types. Nodes of the polygon shapes are densified to 10 m and are draped onto ground surface elevation. As information becomes available, future iterations of the model shall attempt to include more detail on the spatial distribution and incorporate information on overburden thickness.

Table 2. Description of surficial water feature and overburden data.

Feature	Description/Input	Source
Lakes, Wetlands and Rivers	There are 12 lakes within the site-scale ranging in size from 627 m^2 to 1,495,307 m^2, with a total surface area of 1,886,827 m^2. One named lake identified as 'dry-nl-598' is the largest lake within the model located along the eastern boundary. Approximately 40 percent of the lake exists outside of the model extent. The total lake surface area within the site-scale model represents just under 4 percent of the area.	Land Information Ontario (LIO)
Overburden	The footprint of the site-scale model is sparsely covered with Quaternary overburden material. Based on data compiled by the Ontario Geological survey (i.e. NOEGTS), Figure 6 shows the majority of the area is comprised of exposed bedrock or thin veneer, with two relatively small units distributed through the area. A small glaciolacustrine deposit is located along the northern boundary of the site. The largest deposit consists of organic material through the central portion of the site, which in general follows a broad low-lying valley through the area.	Northern Ontario Engineering Geology Terrain Study (NOEGTS)

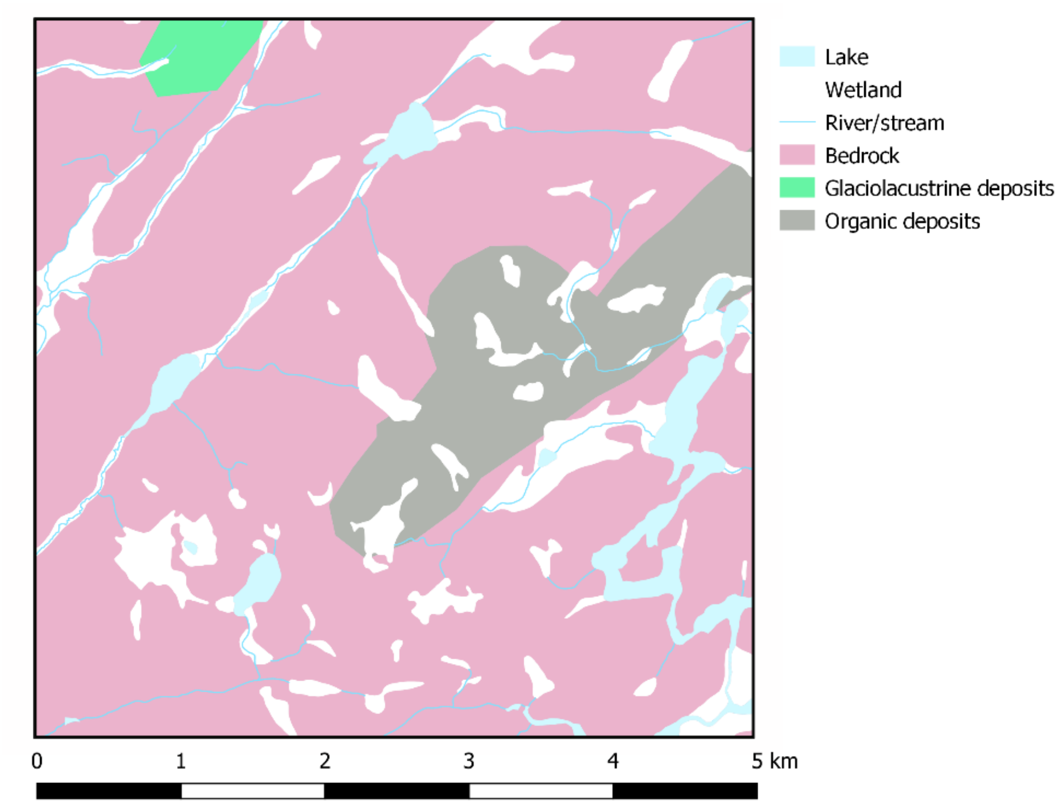

Figure 6: Water features, including lakes, rivers and wetlands, and distribution of Quaternary overburden composed of glaciolacustrine and organic deposits within the site-scale extent. The main bedrock exposed comprises Biotite Granodiorite to Granite suite.

3.2 Revell Site Area Geology

The following subsections provide an overview of the character of the bedrock geology at the Revell site, including descriptions of the main rock types and structures observed. The information presented here is based on the data acquired during two phases of outcrop mapping (SRK and Golder, 2015; Golder and PGW, 2017).

3.2.1 Rock Types from Surface Mapping

The Revell site is underlain by bedrock that is identified across the entire northern lobe of the Revell batholith and belongs to the biotite granodiorite to granite suite. During the mapping work, a hand-held gamma ray spectrometer was used on the main intrusive phase of the batholith to better understand the distribution of granodiorite, tonalite, and granite (Golder and PGW, 2017). Using the potassium values as an indicator, the main rock type was subdivided into tonalite (<1.7 % K), granodiorite (1.7 to 3.0 % K), and granite (>3.0 % K). Based on this analysis (Figure 7), Golder and PGW (2017) determined that granodiorite was the predominant phase encountered based on number of occurrences, followed by tonalite and then granite. They observed no evidence of an intrusive relationship between the granodiorite and tonalite phases and instead determined that they were in gradational contact and together represent a coherent intrusive complex. No boundary was defined for this granodioritic to tonalitic phase of the biotite granodiorite to granite unit. Granite was observed to intrude into the granodiorite and tonalite, suggesting that it is a separate, younger, intrusive phase within this e unit (Golder and PGW, 2017).

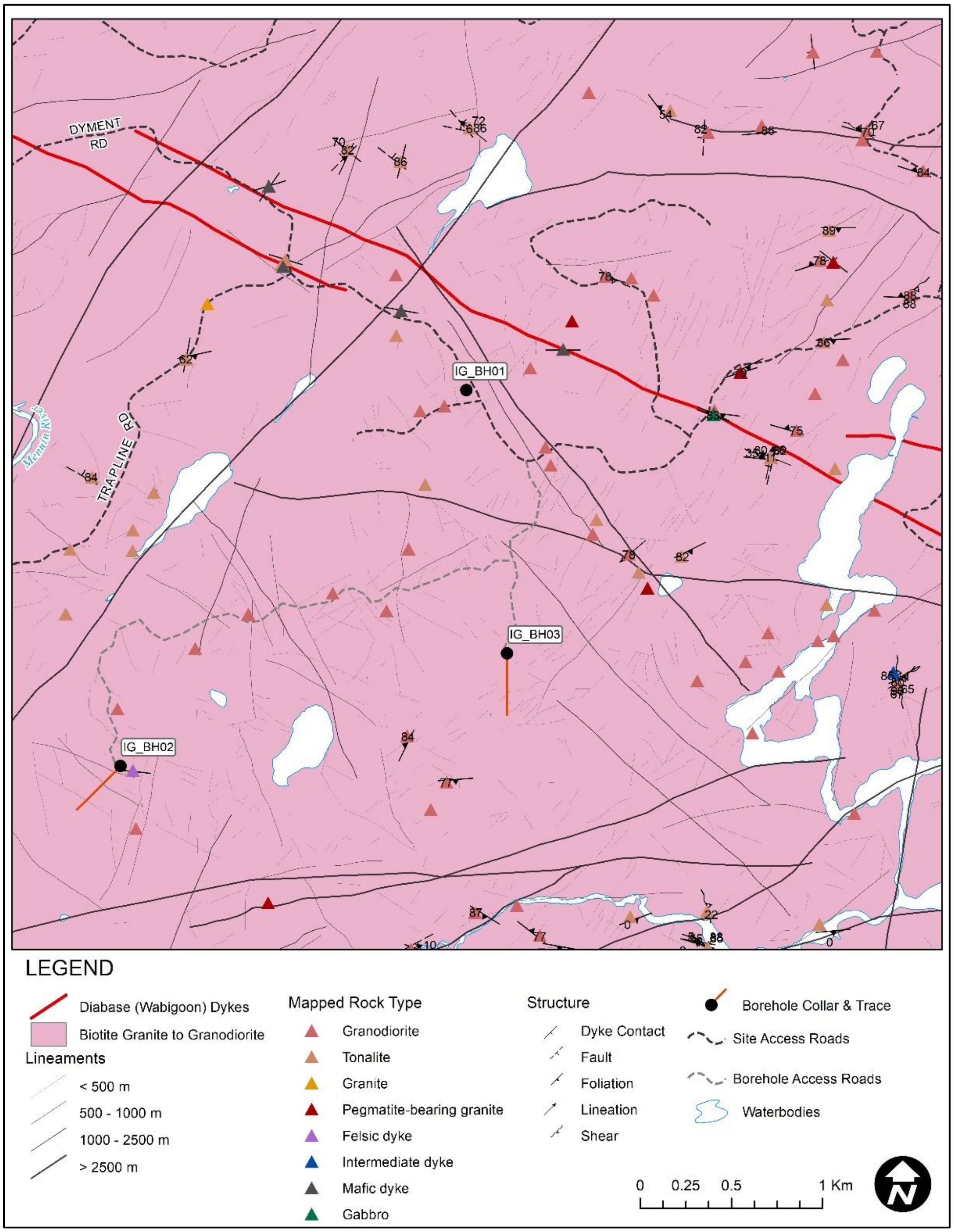

Figure 7. Borehole area showing field mapping stations with identified rock type and select structural measurements.

Detailed descriptions of the granodiorite, tonalite and granite phases distinguished within the biotite granite to granodiorite unit in the northern part of the Revell batholith are presented in Golder and PGW (2017). The granodiorite is predominantly white to light grey, pink or beige on fresh surfaces and light grey, white, brown or pink on weathered surfaces (Figure 8a and Figure 8b). The granodiorite matrix is most commonly medium-grained (1–5 mm), with some local fine-grained (0.5–1 mm) and coarse-grained (5–10 mm) variations. Main matrix mineral phases within the granodiorite are quartz, plagioclase, alkali feldspar and biotite. The predominant phenocryst phase is medium- to coarse-grained (10–50 mm) K-feldspar. The granodiorite is usually massive with an equigranular to inequigranular, occasionally porphyritic, texture. Locally, the granodiorite exhibits a weak foliation defined by aligned quartz, biotite and/or feldspar phenocrysts.

The tonalite is, similarly, predominantly white to light grey or grey on fresh surfaces and most commonly light grey to grey or beige on weathered surfaces (Figure 8c). The tonalite matrix is most commonly medium-grained (1–5 mm), with some local variation to fine-grained (0.5–1 mm) and coarse-grained (5–10 mm). Main mineral phases within the tonalite matrix include quartz, plagioclase, biotite and hornblende. The predominant phenocryst phase is medium- to coarse-grained (10–50 mm) plagioclase. The tonalite is observed as either massive or weakly foliated in texture. Where foliated, the long axes of the phenocrysts and aligned quartz define the planar structure.

The granite is predominantly pink to off white or light grey on fresh surfaces and most commonly light grey to beige or pink on weathered surfaces (Figure 8d, Figure 8e and Figure 8f). The granite matrix is fine-grained (0.5–1 mm) to medium-grained (1–5 mm). Main mineral phases within the granite are quartz, plagioclase, K-feldspar and biotite. Phenocrysts, predominantly plagioclase, K-feldspar or quartz, commonly range from medium- to coarse-grained (10–50 mm).

Figure 8. Field examples of the plutonic rocks of the Revell batholith. (a) Typical exposure of granodiorite at outcrop scale. Yellow notebook and gamma ray spectrometer for scale. (b) Close-up of granodiorite showing mineral composition and texture. (c) Close-up of tonalite showing mineral composition and texture. (d) Typical exposure of granite at outcrop scale. (e) Close-up of granite showing mineral composition and texture. (f) Close-up of feldspar-megacrystic granite showing mineral composition and texture.

Golder and PGW (2017) identified cm- to m-scale xenoliths of tonalite within the biotite granite to granodiorite unit. These tonalite occurrences are distinguished by their sharp contacts with the surrounding biotite granite to granodiorite and by the presence of hornblende in their matrix. These xenoliths are interpreted to represent the remnants of a massive to gneissic tonalite suite that predated the intrusion of the biotite granite to granodiorite. Stone et al. (2011a) and Golder and PGW (2017) also identified cm- to m-scale pegmatite and aplite dykes throughout the biotite granite to granodiorite unit. These dykes are commonly observed to be hosted by fractures that are parallel to unfilled joints. A consistent relationship observed is felsic dykes that are cross-cut by quartz-filled shear zones and fractures. There is no evidence of brittle deformation localized along the felsic dyke contacts.

Larbi et al. (1995) report a $^{207}Pb/^{206}Pb$ age of ~2734 Ma for a sample of the foliated biotite granite to granodiorite unit. The information about this sample, including its age, was included in OGS (2019) along with a note indicating that the precise co-ordinates of the sample collection location were not included in the original source. It remains uncertain if this age can be attributed to the biotite granite to granodiorite unit. Alternatively, it could represent a sample of the foliated tonalite that is present as xenoliths within the biotite granite to granodiorite unit.

3.2.2 Structure from Surface Mapping

Both ductile and brittle structures have been documented at surface throughout the northern part of the Revell batholith (Golder and PGW, 2017), including within the site-scale model extent. Brittle structures, including mapped joints, veins and faults, are more prominent at the outcrop scale than ductile structures, which include a weak to moderately developed tectonic foliation and narrow shear zones.

The surface mapped foliation is defined by aligned biotite. Foliation planes are near vertical and predominantly dip to the north or south (Figure 9a). Ductile and brittle-ductile shear zones at the Revell site are characterized by a strong to intense planar fabric developed within mm- to cm-scale zones. In some cases, these shear zones can include damage zones up to one metre in width (Golder and PGW, 2017). Shear zones are filled with secondary quartz, which in some cases is deformed into lenses. One shear zone was observed to offset a felsic (aplitic) dyke. Poles to shear zones suggest that their planes are generally steeply inclined and dip in several directions including northwest, north, and northeast. One gently inclined shear zone dips towards the east (Figure 9b).

Poles to fracture planes mapped on outcrops within the Revell site, including joints, veins and faults, are shown in Figure 9c. The majority of fracture planes are steeply inclined to vertical and they predominantly strike broadly northeast or northwest. In addition, a gently inclined to horizontal fracture set is present. This latter set was initially inferred to represent stress-release jointing near the ground surface (Golder and PGW, 2017). However, as will be presented in Section 3.3 below, gently inclined fractures are present along the entire length of all boreholes and so their formation cannot be attributed to stress-release alone. The northeast and northwest trends evident in the fracture dataset are also evident in the rose diagram of all brittle lineaments interpreted within the Revell batholith (Golder and PGW, 2017).

Fault damage zones range from thin, single slip surfaces to zones several metres wide. Secondary infilling associated with faulting includes epidote, hematite, chlorite or breccia. Similar infilling mineral phases are identified in veins and as thin coatings on some joints. Slickenlines are observed on individual, isolated fault planes and in fault zones characterized by multiple parallel surfaces. Slickenlines, where mapped, are consistently subhorizontal to moderately plunging suggesting primarily, or partly, strike-slip fault movement. Dextral and sinistral faults exhibit some overlap in their trends, though one main peak in the dextral fault data set trends southeast-northwest (Golder and PGW, 2017).

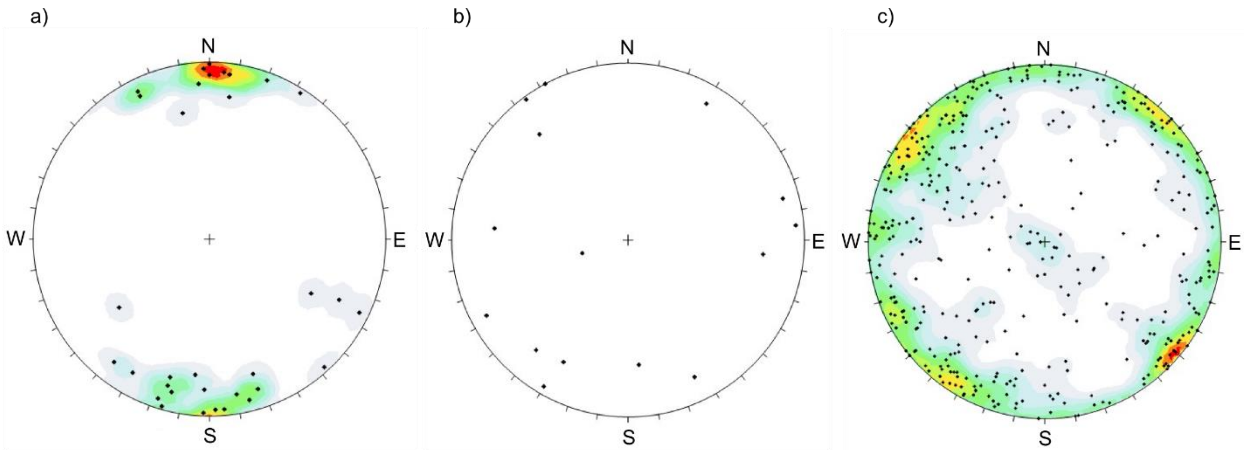

Figure 9. Equal-area lower hemisphere projections of poles to the planes of surface mapped planar structures, including a) foliation (N = 33), b) shear zones (N = 15), and c) fractures (N = 426), including all joints, faults and veins. Note that the shear zone dataset is not contoured due to the limited number of data points.

3.2.3 Diabase Dykes

The youngest Precambrian rocks in the Revell batholith are the west-northwest trending Wabigoon dykes (Figure 10 and Figure 11). These dykes stretch across the northern part of the Revell batholith and into the surrounding greenstone belts and are evident as highly magnetic lineaments that contrast with the low magnetic response of the Revell batholith (SGL, 2015, DesRoches et al 2018). Regionally, Wabigoon dykes extend in a northwest orientation for several 10's of kilometres beyond the Revell batholith.

The Wabigoon dykes are characteristically black to dark grey when fresh and brown to black when weathered (Figure 10; Golder and PGW, 2017). They are massive in texture and generally vary from very fine- to medium-grained. The primary mineral phases observed within the mafic dykes include pyroxene, plagioclase, amphibole, and magnetite with minor occurrences of pyrrhotite and biotite. Overall, the Wabigoon dykes exhibit the character typical of diabase dykes (Golder and PGW, 2017).

The Wabigoon dykes commonly exhibit a sharp and very fine-grained, mm- to cm-width, chilled margin which transitions to coarser-grained towards the center of the dyke occurrences (Satterly, 1960; Golder and PGW, 2017). Most observed dyke-host contacts were intact and exhibited no evidence of brittle reactivation along their contacts. However, some Wabigoon dykes do exhibit an increased density of jointing near their contacts with the surrounding bedrock (Figure 10b).

Wabigoon dykes range from less than 10 cm to approximately 30 m in width. Satterly (1960) identified and traced the approximate locations of several of these dykes across the northern part of the Revell batholith. It is inferred, based on surface measurements across one 18 m wide dyke, that these late intrusions are sub-vertical (Golder and PGW, 2017).

An isotopic age of 1675 Ma reported by Wanless (1970) suggested a Proterozoic age for the Wabigoon swarm. Subsequently, Fahrig and West (1986) reported a K/Ar age of ca. 1.9 Ga. More recently, a Wabigoon dyke sample gave a U-Pb age of 1.887 Ga (Stone et al., 2010).

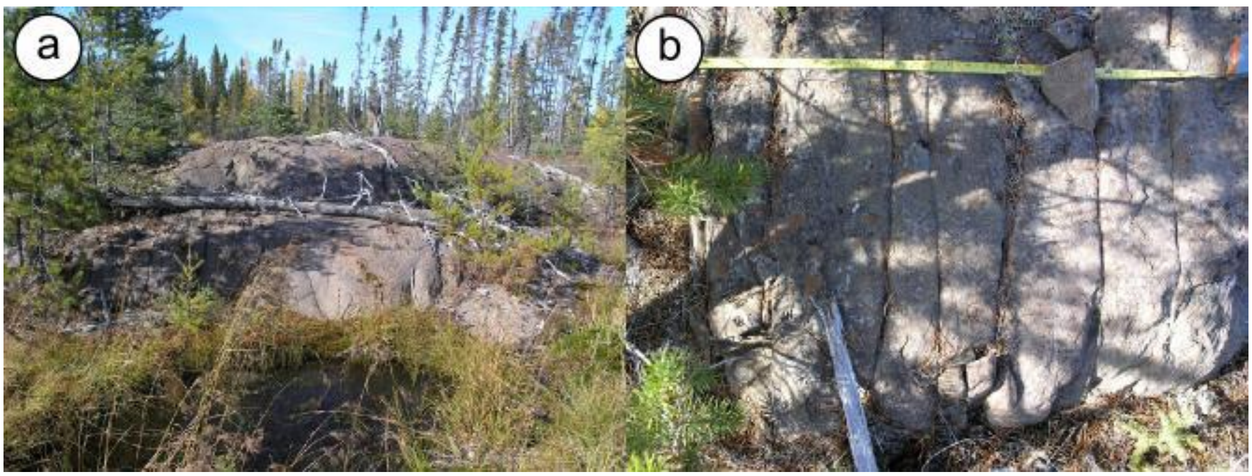

Figure 10. Field examples of Proterozoic Wabigoon dykes. (a) Typical exposure of a Wabigoon dyke covering entire field of view. (b) Close-up of fractures developed at low angle to dyke contact near its margin.

Based on information to date, the diabase dykes are steeply inclined to vertical, with localized mapped contacts ranging in dip from 71 to 90 degrees predominantly northward (Figure 11; Golder and PGW, 2017). In airborne magnetic data, their trends are similar with a mean azimuth of 110°. Two mapping stations along lineament Dyke01 within the site-scale extent provided a perpendicular width of 18 m for the dyke. Immediately outside the site extent a diabase dyke was mapped with a perpendicular width of 30 m attributed to Dyke03.

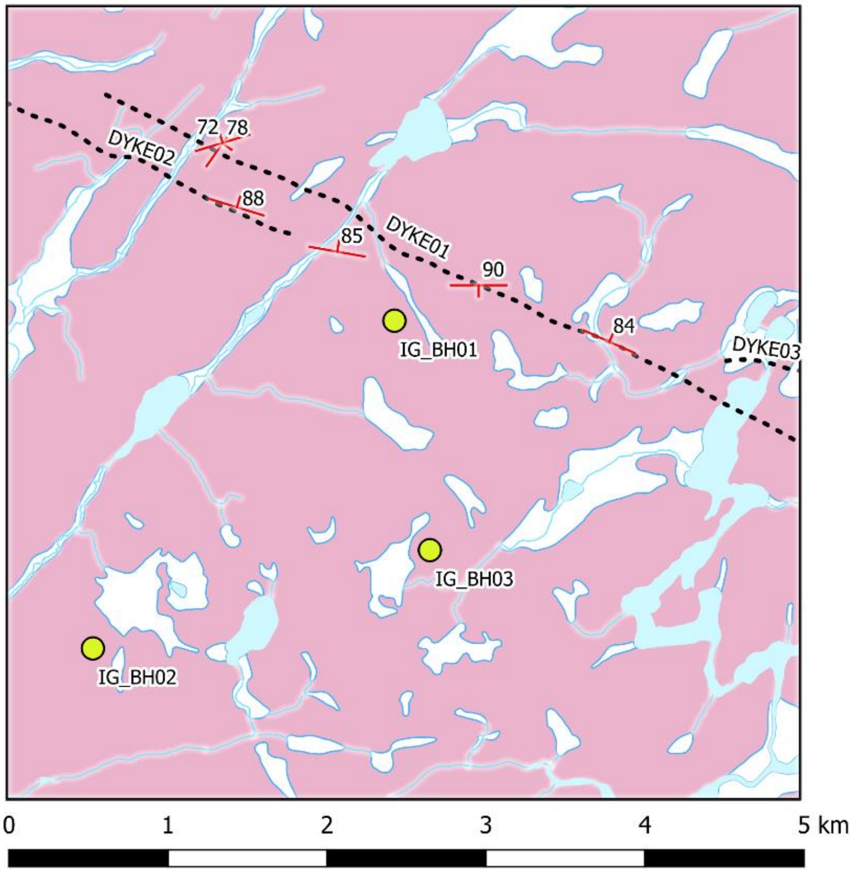

Figure 11. Northwest trending Wabigoon diabase dyke swarm crossing through the site-scale extent. Airborne magnetic data allowed for three separate dyke segments to be delineated (black dashed lines). Red vector symbols define the local strike and dip (with magnitude) of the dyke contact.

3.3 Borehole Data

Between 2017 and 2020, three boreholes have been drilled to build an initial understanding of the subsurface bedrock geology at the Revell Site Area. Preliminary descriptions of all drill cores from IG_BH01, IG_BH02, and IG_BH03 based on onsite geological and geophysical core logging have been published as separate reports.

Approximately 1000 m of continuous HQ core was recovered from each borehole allowing for detailed logging of rock type, alteration, structure, and geotechnical properties. IG_BH01 was drilled nearly vertical with a main objective to evaluate the integrity of the bedrock away from fracture zones assumed to correspond to interpreted lineaments on the ground surface (Golder, 2018a). IG_BH02 and IG_BH03 were drilled with a planned incline of 70º towards the southwest (225º) and the south (180º), respectively (Golder, 2020d, 2020a). The inclination and azimuth of these boreholes were chosen to increase the likelihood of intersecting high-angle fractures in the subsurface that may correspond in part to such fracture zones.

Rock type, alteration, structure, and geotechnical properties were all logged immediately following the retrieval of core from the subsurface (Golder, 2018b, 2020b, 2020e). In addition, each core run and set of four core boxes were photographed to produce a high-resolution core library that can be used as a verification step to reassess and confirm the data from core logging. During logging, core samples were collected for laboratory assessment of certain geomechanical, petrophysical and porewater characteristics. Although these laboratory results have not been directly incorporated into this version of the model, these results indirectly play a role in validating our subsurface model geometry. Petrophysical properties derived from core samples will be useful for producing petrophysical distributions in future model iterations.

Following the completion of coring and sampling, a comprehensive suite of geophysical logs was acquired over the entire length of each borehole (Golder, 2019, 2020c, 2020f). In particular, natural gamma, spectral gamma, gamma-gamma density, and neutron were used both for validating rock types and delineating more confidently the contacts between different rock types. Such subtle boundaries could reflect sharp or gradational changes in mineralogical composition, such that any variability not observed in the initial stage of geological core logging could be identified by assessment in comparison with these geophysical logs. These logs represent indirect measurement of the subsurface and have been interpreted together with geological core logging results to establish an integrated assessment of the subsurface (Parmenter et al. 2021a, 2021b and 2021c).

3.4 LiDAR Digital Elevation Model and Aerial Imagery

A Digital Elevation Model (DEM) was derived as part of a LiDAR survey over the Revell batholith and a portion of the surrounding greenstone belt units. The DEM provides data for creating the topography and the upper boundary of the rock volume to be modelled. The LiDAR data was acquired at 8 p/m^2 via a classified point cloud data (v1.4) with a spatial accuracy of 15 cm. Derived products included a digital elevation model (DEM) and digital surface model (DSM) both at 1 m cell size, created from the interpolation of the point cloud data. Details on the creation of the Digital Elevation Model (DEM) can be found in ATLIS (2018)

The digital elevation model for the site-scale extent was re-interpolated in QGIS using a 10 x 10 m cell and imported into GOCAD as an 2D raster grid. The grid resolution was optimized to maintain a high-resolution but minimize the visualization lag. The grid was converted to a surface to represent the topographic surface within the site-scale model.

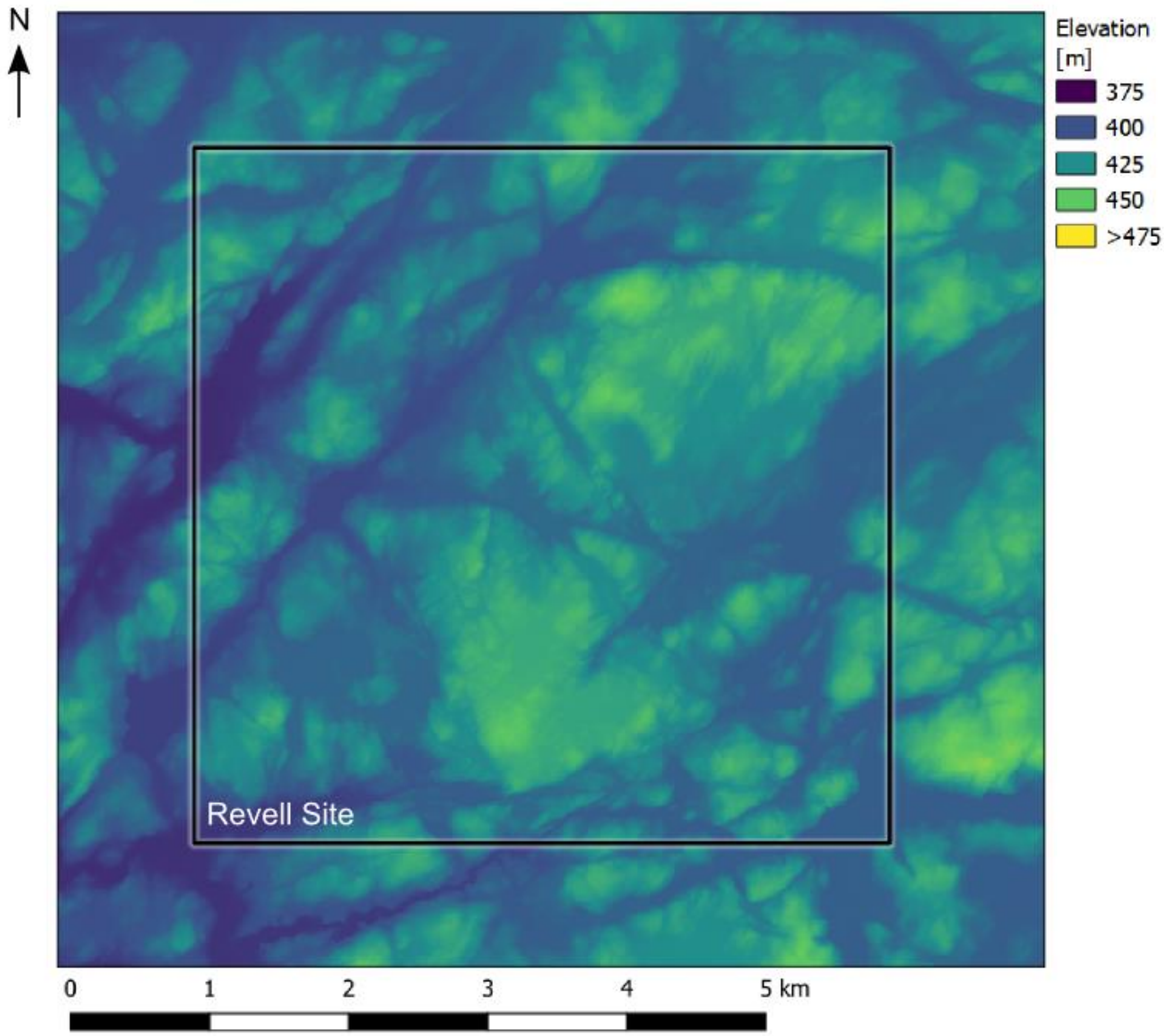

Figure 12. Topographic distribution within the site-scale extent. Topography ranges from 368 to 498 m above mean sea level for a total range of 130 m. Highest elevations exist in the central portion of the site, which broadly slopes towards the west.

High-resolution orthoimagery was acquired concurrently with a LiDAR survey using a Leica RCD30 RGB NIR Stereo Camera mounted on the base of an aircraft. Digital imagery data were captured at a cell resolution of 20 cm, with a spatial accuracy of 30 cm. Details on the creation of the orthoimagery can be found in ATLIS (2018).

The orthoimagery has been incorporated into the site-scale model as a raster grid data set (*.ERS raster grid) and converted to a GOCAD grid format (2D-grid). Figure 13 shows the RGB (red, green, blue) orthoimage composite for the site-scale extent. The southern portion of the site consists of dense forest with mature trees and limited visual bedrock exposure. The majority of the northern and western portions of the site were deforested prior to acquiring the imagery and so bedrock and other geomorphological features are readily exposed.

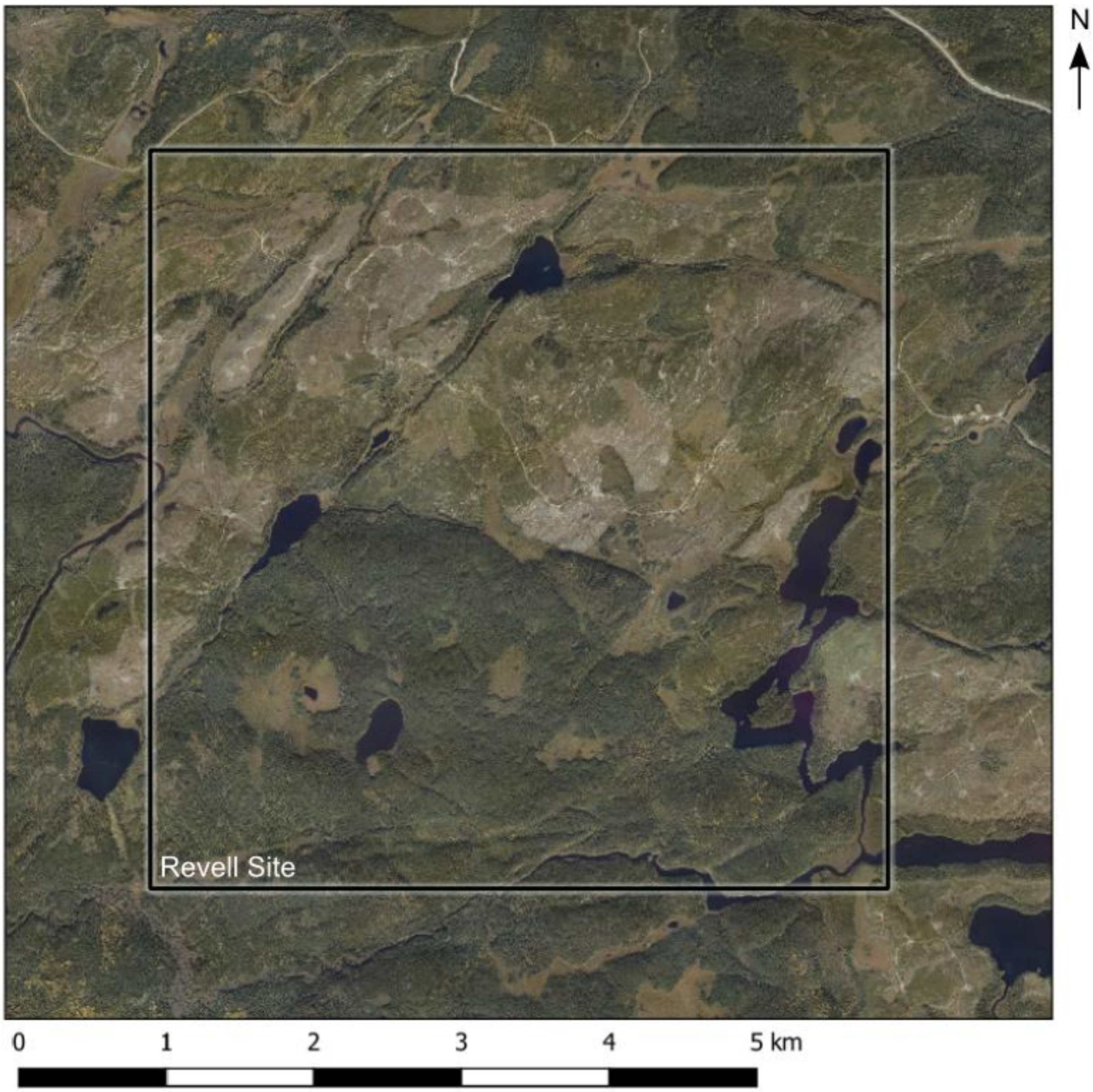

Figure 13. RGB and NIR orthoimage of the Revell Site. Southern portion of the site consists of dense forest with mature trees, whereas the majority of the northern and western portion of the site has been deforested prior to acquiring the imagery (imagery acquired by ATLIS 2017).

3.5 Airborne Geophysics

Airborne total magnetic field data were acquired by Sander Geophysics Ltd (SGL, 2015) within the Revell Batholith and surrounding greenstone belt area. The airborne magnetic data were acquired along planned 100 m traverse lines, and 500 m perpendicular control lines at a target altitude of 80 m above ground surface. Various filters were applied to the processed magnetic data to enhance different wavelength information that arises from different bedrock sources. Various filtering was performed by transforming the data from the space domain to frequency domain by Fourier transform, since frequency characteristics of the filter to be applied are more precisely defined in the frequency domain. As a result, the following derived magnetic grids were produced:

- Reduced to pole transformation of total magnetic field
- First vertical derivative of reduced to pole total magnetic field
- Second vertical derivative of reduced to pole total magnetic field
- Horizontal gradient of total magnetic field
- Analytic Signal of total magnetic field
- Tilt Angle product of reduced to pole total magnetic field.

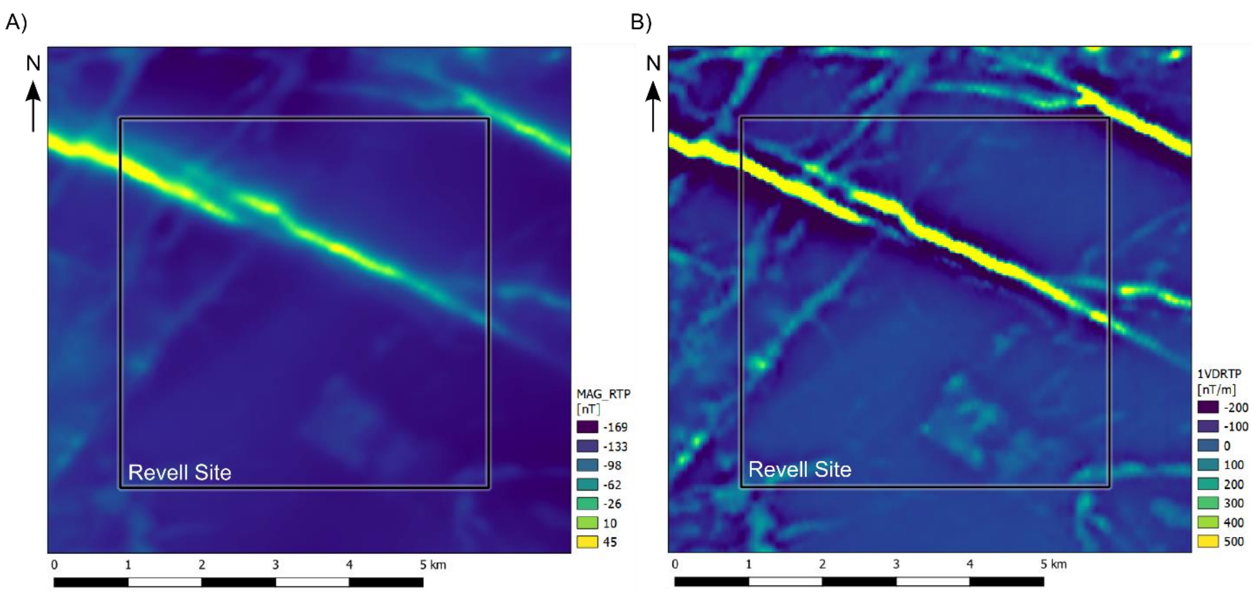

Figure 14. Airborne magnetic data and derivative grids showing the boundary of the Revell site. A) reduced to pole, and B) first vertical derivative of the magnetic field. Northwest trending linear magnetic highs correspond to diabase dykes of the Wabigoon dyke swarm. Majority of the linear magnetic anomalies shown in the vertical derivative are interpreted as magnetite-rich sediments within water bodies and streams.

Each airborne magnetic grid data set was imported into GOCAD as a 2D raster grid (see Figure 14). Figure 14A shows the reduced to pole magnetic data with prominent magnetic anomalies dominated by WNW trending linear response, characterized as mafic diabase dykes. These dykes correspond to the Wabigoon dykes swarm and have elevated magnetic susceptibilities capable of producing a strong anomaly relative to the surrounding bedrock. In general, the remaining bedrock within the site-scale extent, and elsewhere in the Revell batholith have very low magnetic susceptibility and the resulting magnetic response is weak (e.g. SGL, 2015). The remaining weak linear anomalies within the site-scale extent correspond with water features and rivers and streams, which are interpreted as sediments rich in magnetic minerals transported by fluvial processes (e.g. DesRoches et al., 2018). The first vertical derivatives of the pole reduced magnetic field (Figure 14B) emphasize the linear anomalies within the site-scale extent, and further enhance the weaker textural variability in the data. In particular, a rectangular shaped high magnetic anomaly located near the southern boundary of the model extent may be associated with a unique lithologic unit, or the same lithology with increased magnetic mineral composition. This anomaly has no clear correlation with a lake or wetland and does not correspond to a lithologic unit that is currently identified on ground surface. Additional mapping or borehole drilling may be required to further evaluate this anomaly and this potential unit has not been incorporated in the modelling below.

Sander Geophysics Ltd (SGL 2015) also acquired airborne gravity data within the Revell Batholith and surrounding greenstone belt. Similar to the magnetic data, various filters were applied to the gravity data to enhance different wavelength information that arises from different bedrock sources. As a result, a subset of the derived gravity grids are produced and presented in this report:

- Bouguer gravity field
- First vertical derivative of Bouguer gravity field
- Horizontal gradient of Bouguer gravity field

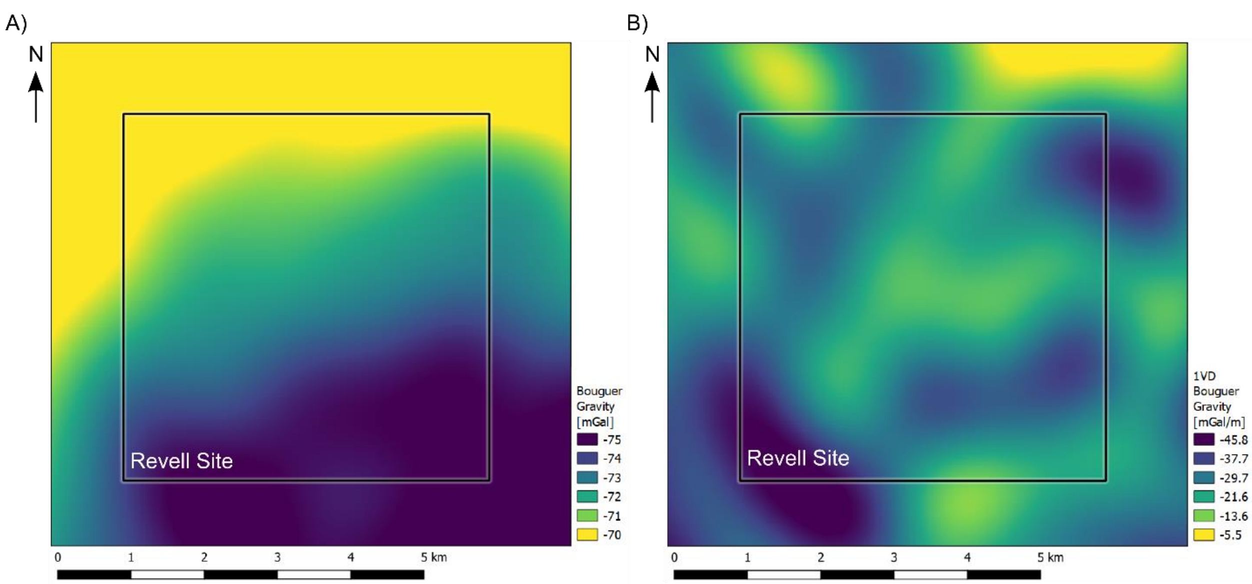

Figure 15. Airborne gravity data and derivative grids clipped to the boundary of the Revell site. A) Bouguer gravity field, B) first vertical derivative of gravity field.

Each airborne gravity data set was imported into GOCAD as a 2D raster grid file (see Figure 15). Figure 15A shows the Bouguer gravity field data characterized by a weak gradient in the gravity field from the NW towards the SE within the site-scale extent. Much of this gradient response is influenced by the regional bedrock geology. The first vertical derivative grid (Figure 15B) display broad linear anomalies that tend to follow the river valleys within the site. It is possible that these anomalies may correspond to the presence and gradual thickening of river valley sediments overlying the bedrock in these areas. At this point, these anomalies are discussed here, but are not expected to impact the development of the geological model in this area.

3.6 Interpreted Lineaments

The result from a structural lineament interpretation completed by DesRoches et al. (2018) over the northern portion of the Revell Batholith and surrounding greenstone belt units is shown in Figure 16. Lineaments are linear to curvi-linear features interpreted from one or more remote-sensing data sets as an expression of an underlying geological structure, including possible brittle, ductile, or brittle-ductile deformation zones. The lineament interpretation is based on high-resolution remote sensing data sets, including high-resolution airborne magnetic data, high-resolution surface topographic data, and digital orthoimagery data collected during the airborne LIDAR survey. Excluding linear positive magnetic anomalies corresponding to diabase dykes, the lineaments within the site-scale extent are assumed to represent the surface traces of planar structures that project into the subsurface as fracture zones. Since fracture zones will have bearing on the safety and constructability of an underground repository, it is important to characterize their location, and other physical attributes. Details of the methodology and complete summary of results can be reviewed in DesRoches et al. (2018).

The integration of magnetic and surficial lineaments for the Revell batholith area resulted in a total of 4701 lineament traces over a footprint that was approximately 500 km^2. As a result, the integrated lineaments comprise 3668 lineaments interpreted as brittle structures (fracture zones), 1023 lineaments interpreted as fabric-concordant structures in the greenstone belts surrounding the Revell batholith, and 10 lineaments that are interpreted as diabase dykes.

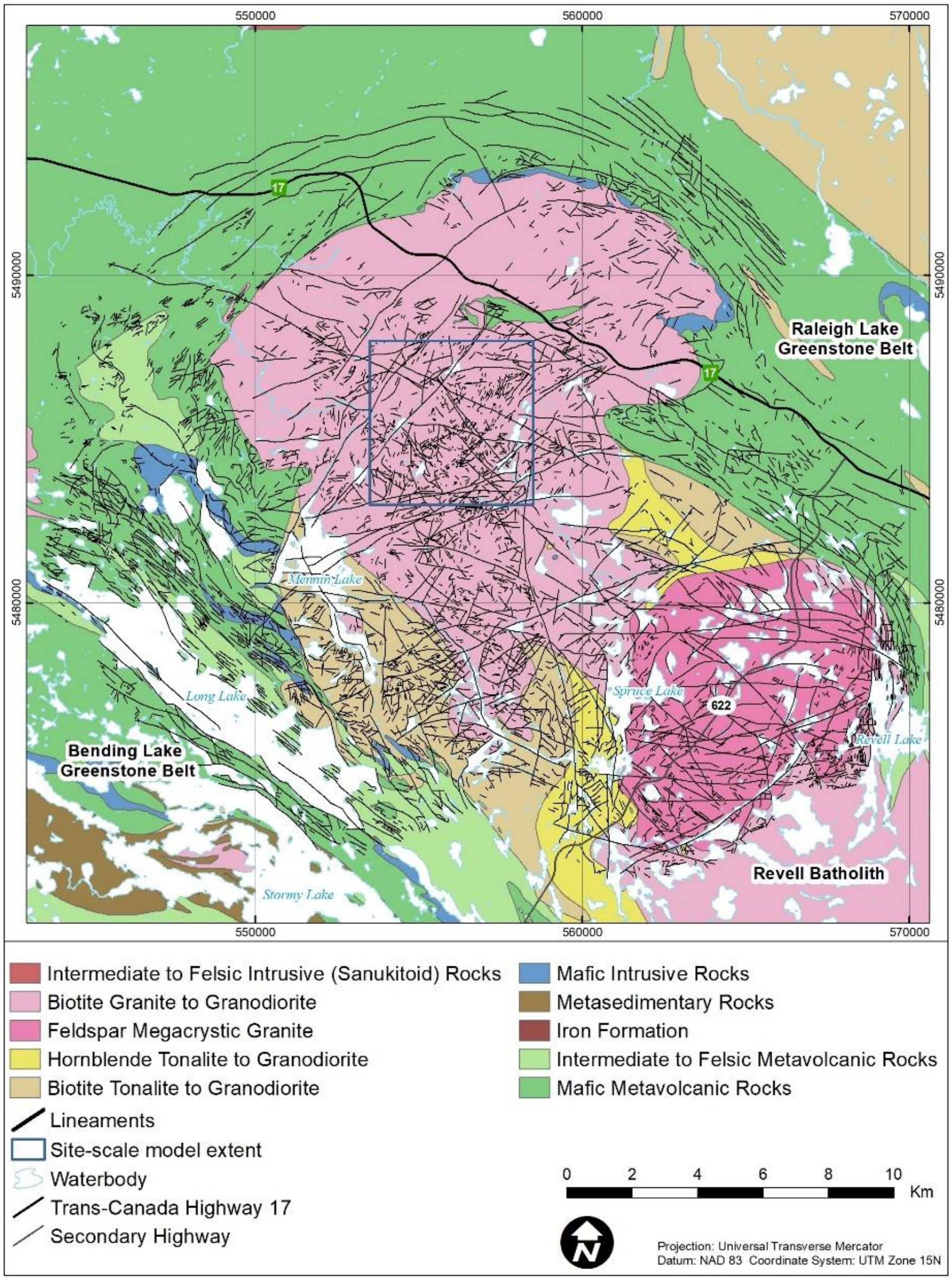

Figure 16. Distribution of structural lineaments interpreted over the Revell Batholith and surrounding greenstone belt units. The thick black outline represents the extent of the site-scale model.

4. Geological Data Integration

4.1 Updated Site-scale Lineament Map

Lineaments interpreted by DesRoches et al., (2018) were traced using a variety of high-resolution remote sensing data covering a nearly ~500 km^2 area, as previously discussed in Section 3.6. Now that a site-scale model extent has been established, there is a need to revisit the interpreted lineament traces within the model extent for completeness and accuracy. Such a reassessment is an important data preparation step in the development of a deterministic fracture zone model, and the approach to the reassessment is documented here.

The reason for the lineament reassessment is to build upon the understanding of the nature and extent of fracture zones specifically within the site-scale model extent. During the previous lineament interpretation, end nodes of lineament traces were terminated based on the evidence from the remote sensing data used at the time. However, in some cases, lineament terminations occurred in proximity to adjacent structure where branching nodes could have been interpreted to be topologically linked. In addition, in several cases there are sets of parallel individual short lineament segments, which may in-fact be part of a longer and more continuous structure. Therefore, evaluating the end points of lineaments as continuous traces and joining end points with adjacent structure were the primary motivations for this reassessment. The results of the reassessment will produce a lineament fracture zone network that follows topological rules and can be directly incorporated into implicit or explicit 3D structural modelling workflows (e.g. Caumon et al., 2009; Cherpeau et al., 2011). The process of reassessing the lineament end nodes provides an opportunity to evaluate and document potential fracture zone truncation and potential fault offset relationships if they exist within the data.

The workflow for the reassessment of lineament traces within the site-scale model extent is described below:

1. Similar to the initial lineament interpretation, the lineament reassessment was completed using QGIS to modify the original polyline traces using the same subset of remote-sensing data (e.g. Lidar, airborne magnetic data and orthoimagery). QGIS offers advanced digitizing tools to edit polyline nodes, merge polylines and extend or trim polylines based on endpoint truncation relationships.

2. The interpretation was conducted jointly by three geoscientists with expertise in structural geology. The combination of multiple interpreters allowed for consensus on the refined lineament trace, and the assignment of attribute characteristics.

3. Lineaments of all trace lengths were selected from within the site-scale model extent, and within a 2 km buffer outside the site-scale model boundary. The additional buffer allows any lineaments that overlap the boundary to be evaluated.

The reassessed lineament network results in lineament traces of all lengths, with characteristics compiled into an attribute table. Due to the nature of merging lineaments, it does not make sense to carry all attributes forward from the previous interpretation of DesRoches et al. (2018). Therefore, a new set of attributes has been compiled to better characterize and describe the reassessed lineaments. Similar to the previous interpretation, attributes which describe the unique lineament identifier and geometry of the lineament are documented, such as trace length and azimuth (strike), in addition to including an attribute for dip magnitude. Although very little is currently known regarding the dip of these fracture zones, this attribute will document our current assumptions, and will be continually updated as more information is collected. Three new categories are provided, including deformation set, deformation order and zone width.

4.1.1 Comparison to Previous Lineament Interpretation

Figure 17 presents a comparison of lineament traces within the extent of the site-scale model. The resulting reassessment did not remove any lineaments from the original data set (e.g., DesRoches et al 2018),). However, there are several cases where shorter lineaments were linked to form longer lineaments. These longer lineaments were only extrapolated if there was some underlying evidence observed from the remote sensing data sets. Overall, the final result provides a better representation of the lineament network and their calculated length extent, which can now be used in developing a 3D deterministic fracture zone model (discussed below in Section 5.5).

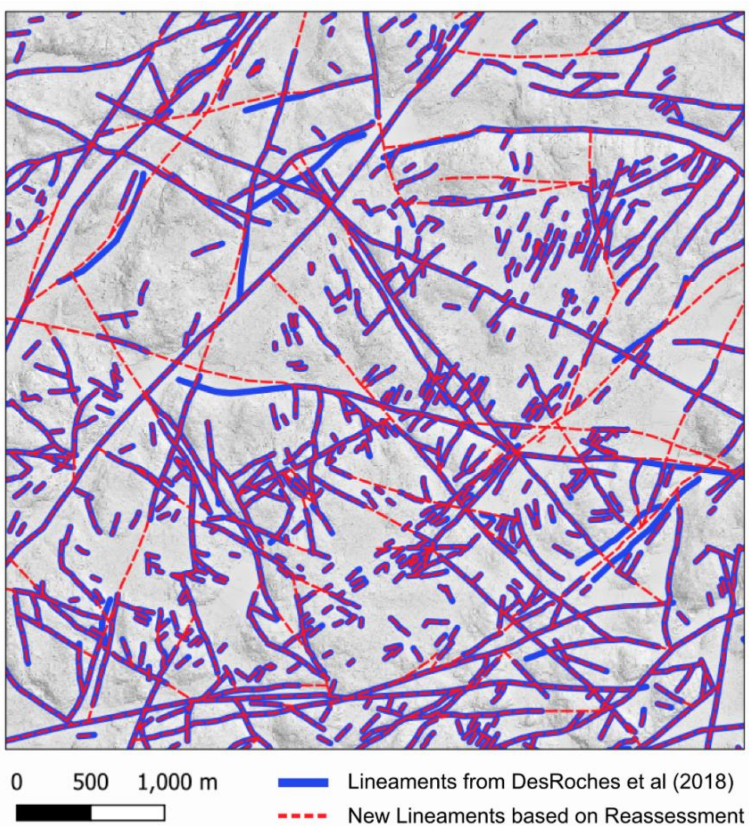

Figure 17. Comparison between lineaments interpreted from DesRoches et al (2018) and the new lineaments based on the reassessment documented in this report.

4.1.2 Deformation Order

Deformation order provides an interpretation of the degree of possible deformation and is based on evidence from the remote sensing data from which it is derived. Largely, this classification is based on the length, observable width representation in the data, and scale at which the lineament is observed in the remote sensing data. Here we suggest that first-order fracture zones are regional scale structures which formed originally during accretion of the Superior Province cratons. Based on the Ontario bedrock geological map (MRD126-rev1), regional scale faults that extend across entire Subprovince boundaries are considered to represent the first-order structures, whereas fracture zones interpreted within our site-scale model are interpreted to represent higher order fracture zones ranging from approximately 10 km long structures down to single discrete fractures or small-scale fracture swarms. The regional scale structures within the western Wabigoon Subprovince are typically E-W to NE striking, with the closest structure being approximately 10 km to the southwest from our site-scale model boundary and located within the Bending Lake Greenstone Belt (Figure 18). Therefore, no first-order structures have been classified within our site-scale model. Structures interpreted within our site-scale model are classified as second- and third-order structures (order = 2 and 3) and divided into different sets according to trend, as shown in Figure 19.

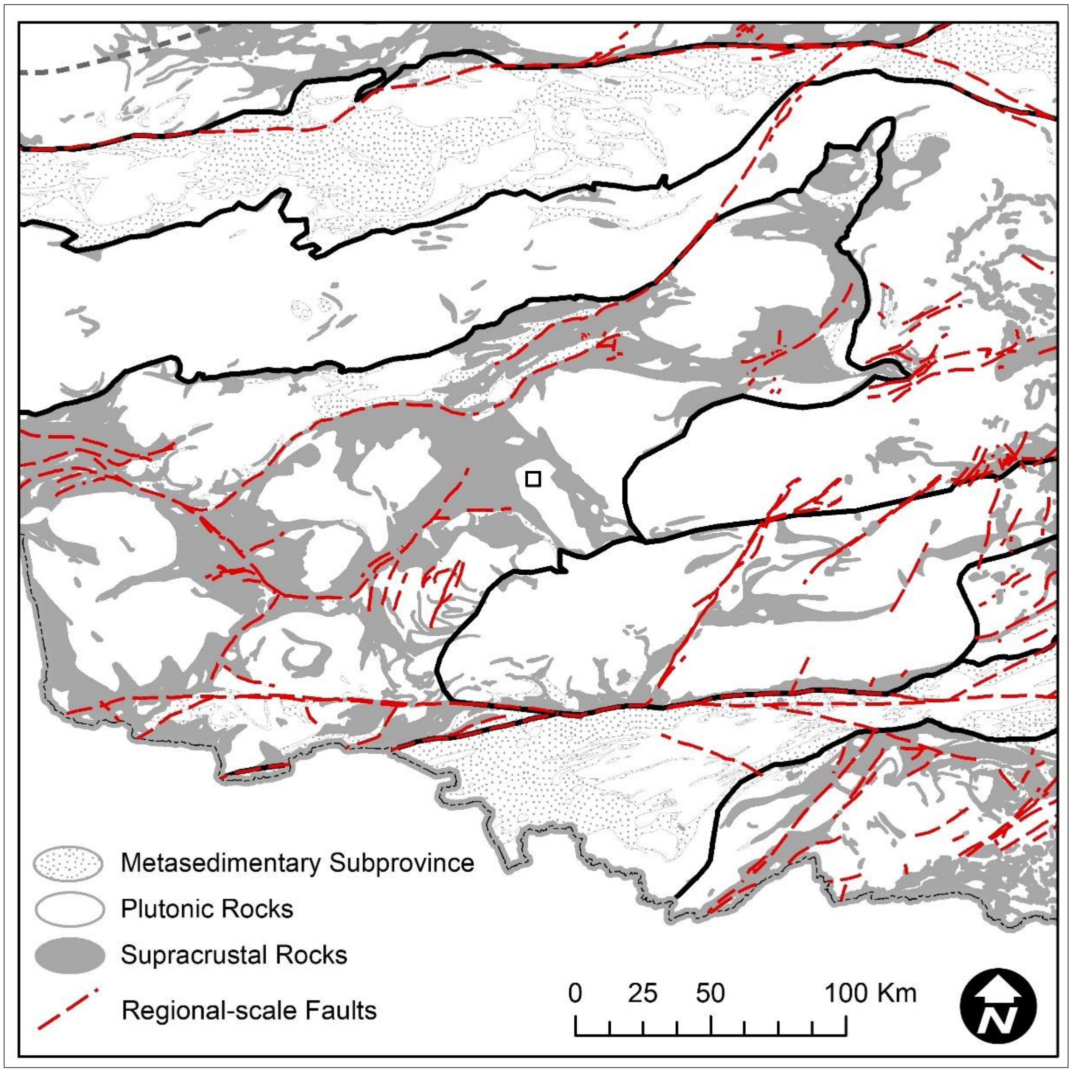

Figure 18. Regional-scale faults interpreted to represent first-order fracture zones in the region. Fault data comes from Ontario Geological Survey (MRD126-rev1). Solid black lines represent sub-province tectonic boundaries.

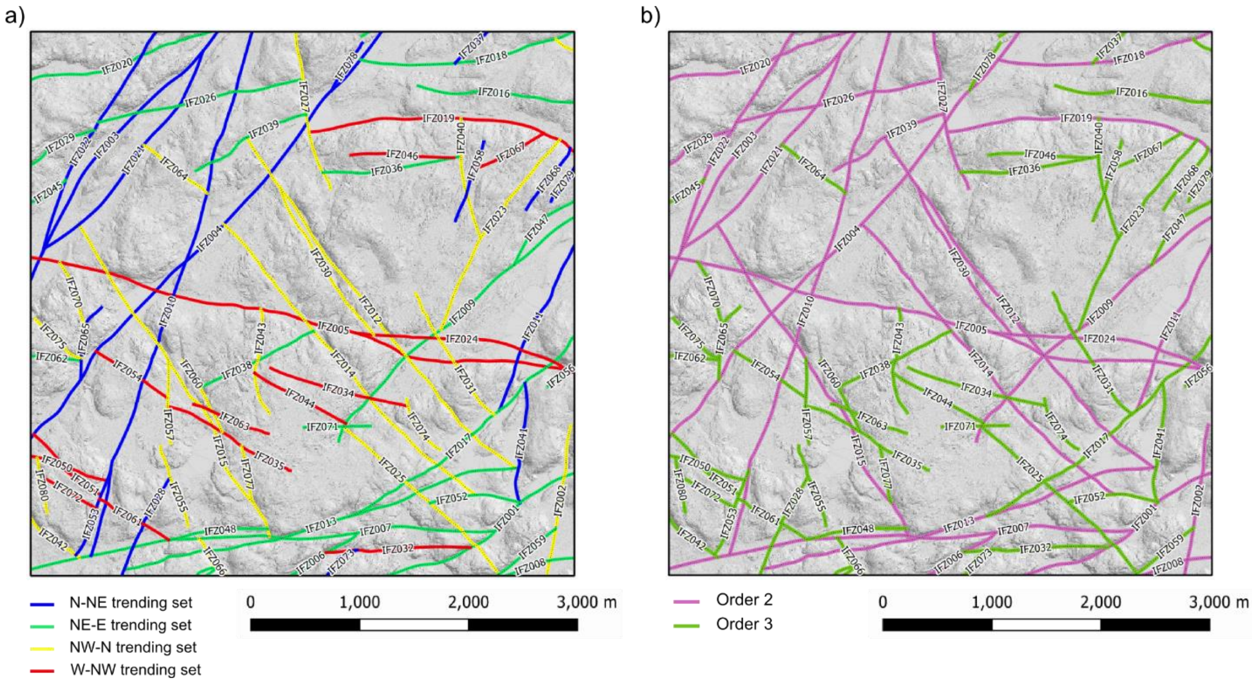

Figure 19. Lineaments at the Revell site presented by a) orientation set, and b) order, based on relationship with regional scale structures. Unique identifiers on the lineaments correspond to their inferred fracture zone surfaces (see section 5.5)

4.2 Compilation of Single Borehole Integration Reports

Between 2017 and 2020 three boreholes have been drilled to build an initial understanding of the subsurface bedrock geology at the site. The objective of the Single Borehole Data Integration reports (Parmenter et al. 2021a, 2021b and 2021c) is to summarize geological findings that aid in providing an initial interpretation of the lithological and structural characteristics of the geosphere. As more data becomes available, the initial interpretation will be revised to update our understanding of the subsurface. The following sections present an initial interpretation of the subsurface based on the compilation of the first three boreholes.

4.2.1 Integrated Rock Types and their Mineralogical Characteristics

The single borehole integration reports present the rock types from each borehole as an assessment of geological core logging and geophysical logging, combined with petrographic and lithogeochemical analysis of selected core samples (Parmenter et al. 2021a, 2021b and 2021c). Rock types were classified by visual inspection during geological core logging and were updated as needed based on analysis of whole rock lithogeochemistry, optical petrography, petrophysical data, and continuous borehole geophysical log data. Gamma-gamma density, neutron and natural gamma ray logs are nicely correlated to discrete rock type intervals throughout the length of the drilled boreholes and have provided an important process for assessing the visual character and boundaries of the classified rock types from geological core logging. In addition, ninety-seven core samples were analysed for whole rock lithogeochemistry by Activation Laboratories, Ltd. to support the rock type and petrogenetic interpretation (Parmenter et al. 2021a, 2021b and 2021c).

Through the complete integration process, a total of ten unique rock types plus overburden have been logged in the three boreholes. Table 3 reveals each of the unique rock types and quantifies their measured lengths along the boreholes and their relative percentages.

Table 3. Total logged length and percentage of distinct rock types recorded in each borehole. Distinct rock types were determined by geological core and geophysical logging, combined with petrographic and lithogeochemical data.

Rock Type	IG_BH01		IG_BH02		IG_BH03		Description
	Total Logged Length (m)	% of Recovered Core	Total Logged Length (m)	% of Recovered Core	Total Logged Length (m)	% of Recovered Core	
Overburden	0	0	2.71	0	1.21	0	-
Biotite granodiorite-tonalite	864.40	86.4	954.42	95.7	973.95	97.5	Pale to medium white-grey, equigranular, with mineral size tending toward the upper range of medium-grained (0.3-3.5 mm average for all mineral phases).
Amphibolite	12.39	1.2	5.95	0.6	11.70	1.2	Dark grey-green, equigranular, and generally fine- to medium-grained (0.2 – 2 mm; Minerals include tremolite/actinolite, biotite, quartz, epidote, albite, and chlorite +/- pyrite. The mineral assemblages are suggestive of albite-epidote hornfels facies metamorphism of basic rocks (e.g., Raymond, 2002), and are also consistent with
Feldspar-phyric tonalite dyke	4.83	<0.5	24.02	2.4	4.66	0.5	Dark grey-black with an aphanitic matrix and 1-5 mm albite phenocrysts. Petrographic analysis identified the mineral composition of the dykes as quartz, plagioclase, and biotite with very minor K-feldspar.

Aplite dyke	3.27	<0.5	3.01	0.3	0.88	<0.5	Pale white-grey to pink-beige, equigranular, and very fine-grained (<0.5 mm). The aplite dykes are granitic in composition with main mineral phases of plagioclase, potassium feldspar, quartz and minor biotite.
Pegmatite dyke	0.65	<0.1	0.92	0.1	0.09	<0.01	Pale grey-pink, massive, and inequigranular with distinct, very coarse-grained (10-50 mm), square-edged feldspar crystals within a medium-grained (5-10 mm) matrix of quartz, feldspar, and biotite.
Aphanitic tonalite dyke	0.43	<0.1	4.22	0.4	5.93	0.6	Dark grey-black, aphanitic to very fine-grained. Petrographic analysis identified the mineral composition of the dykes as quartz, plagioclase, and biotite with very minor K-feldspar.
Biotite granodiorite-tonalite dyke	0.62	<0.1	2.42	0.2	0.24	<0.02	Pale white-grey, equigranular, medium-grained, and massive. Their petrographic and lithogeochemical compositions are the same as the biotite granodiorite-tonalite bedrock, but a distinct intrusive relationship is observed in the borehole and therefore these units are interpreted as dykes.
Granite dyke	-	-	-	-	1.98	<0.5	Equigranular, medium-grained leucogranites with main mineral phases of plagioclase, K-feldspar, quartz, and minor biotite.

Biotite tonalite	114.22	11.4	0.46	<0.05	-	-	Pale to medium white-grey, equigranular, with mineral size tending toward the lower range of medium grained (0.1-2 mm average for all mineral phases.
Quartz dyke	0.37	<0.1	2.29	0.2	-	-	White, massive, fine- to coarse-grained, composed almost entirely of quartz sometimes with accessory pyrite.

Information presented in Table 3 show that a significant proportion of each borehole is dominated by biotite granodiorite-tonalite. In the case of borehole IG_BH01, biotite granodiorite-tonalite and biotite tonalite are interpreted to represent subtle differences in mineralogical composition of the same intrusive unit. Together the biotite granodiorite-tonalite and biotite tonalite make up more than 97% of the total drill core length (Table 3 and Figure). Representative samples are shown in Figure 21.

Such continuity in the main rock type throughout the boreholes and ground surface make subdividing the bedrock into rock unit domains challenging. Despite the challenge, vertical distributions of rock types within each borehole forms the basis for defining unique rock unit domains that can be modelled throughout the model extent. These rock domains are further described in Section 4.2.7.

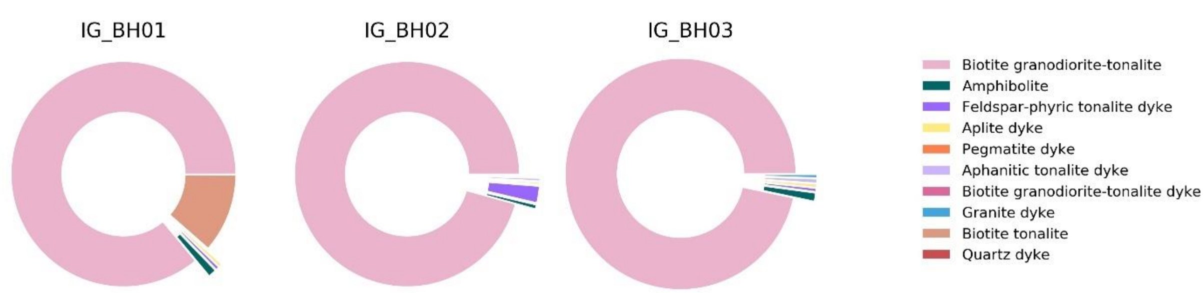

Figure 20. Pie plot showing relative rock type proportions identified within each drilled borehole. All three boreholes are dominated by biotite granodiorite-tonalite, with IG_BH01 showing in addition a high amount of biotite tonalite.

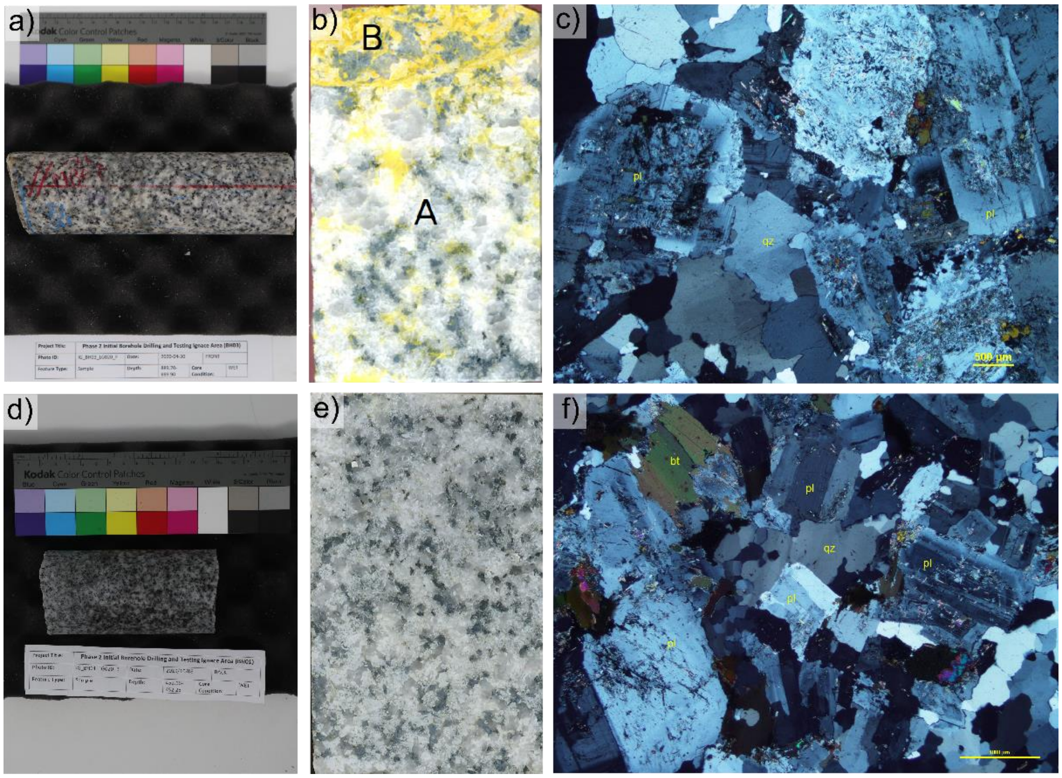

Figure 21. Representative samples of biotite granodiorite-tonalite (IG_BH03_LG020; a-c) and biotite tonalite (IG_BH01_LG020; d-f). a) Hand-sample showing medium grain size and massive texture. b) Thin section billet photograph; billet has been etched with hydrofluoric acid and stained with sodium cobaltinitrite, which gives potassium-bearing minerals a yellow colour (in this case, highlighting K-feldspar; billet size is 25 x 40 mm, A and B denote different grain size domains in the sample). c) Thin section photomicrograph with rock forming minerals plagioclase (pl) and quartz (qz). Minor biotite is also present, and fine-grained white mica is visible in the cores of the plagioclase grains as a secondary alteration; crossed polarizers transmitted light. d) Hand-sample showing fine-medium grain size and massive texture. e) Thin section billet photograph showing absence of yellow staining indicating no K-feldspar present in the sample (billet size is 25 x 40 mm). f) Thin section photomicrograph with rock forming minerals plagioclase (pl), quartz (qz), and biotite (bt), fine-grained white mica is visible in the cores of the plagioclase grains as a secondary alteration; crossed polarizers transmitted light.

Rare-earth element data, collected as part of the lithogeochemistry analysis, are plotted for samples from all three boreholes in Figure 22 (chondrite normalized after Taylor and McLennan, 1985). Biotite granodiorite-tonalite, biotite tonalite, biotite granodiorite-tonalite dykes, and feldspar-phyric and aphanitic tonalite dykes are all steeply fractionated [average $(La/Yb)_{65}$ = 61.6] with significant depletion of heavy rare-earth elements [HREE; average $(Gd/Er)_{65}$ = 3.6]. This pattern is similar to other Neoarchean low-HREE granitoids of the tonalite-trondhjemite-granodiorite (TTG) suite, which carry a basaltic crust signature (Halla et al., 2009; Halla, 2018 and references therein). The origin of low-HREE TTGs is thought to be high-pressure melting of deep, thick, oceanic crust during subduction. The aplite and granite dykes are much less steeply fractionated [average $(La/Yb)_{9}$ =8.2] and are less depleted in HREE [average $(Gd/Yb)_{9}$ =1.7]. The aplite and granite dykes, which are interpreted as the same unit with different grain sizes, show a sharply negative europium anomaly and are enriched in potassium compared to the other units (K_2O = 3.4 – 4.6 %), suggesting they are later stage, evolved granite intrusions.

The amphibolite samples from the Revell Batholith show a similar pattern to the felsic units, suggesting they are from the same magmatic source, though the origin of the amphibolites remains uncertain. The amphibolite samples are less fractionated than the bedrock felsic rocks [average $(La/Yb)_{15}$ = 30.4] and are depleted in HREE [average $(Gd/Er)_{15}$ = 3.4].

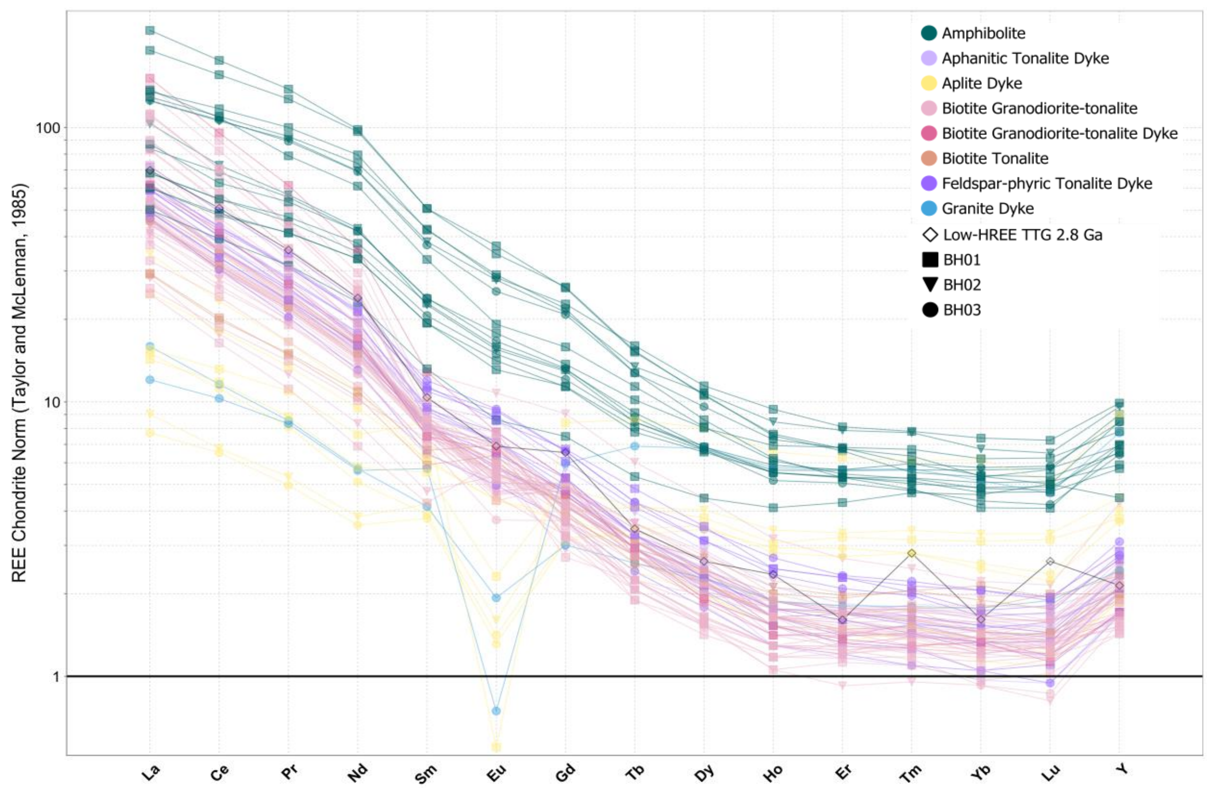

Figure 22: Chondrite-normalized rare-earth element (REE) plot (after Taylor and McLennan, 1985) of 8 of the rock types logged in BH01-03 and a representative average of 2.8 Ga low-heavy REE (low-HREE) tonalite-trondhjemite-granodiorite (TTG) from the Fennoscandian shield (open diamonds; Halla et al., 2009; Halla, 2018). The y-axis shows concentrations (expressed as logarithm to the base 10 of the value) of REE (x-axis, by atomic number) in our samples normalized to a reference chondrite standard.

4.2.2 Alteration

Our early conceptual understanding of alteration within the bedrock is based on information from visual geological core logging and petrography samples specifically targeting logged alteration in boreholes IG_BH01, IG_BH02 and IG_BH03. Eight alteration types were identified during geological core logging: potassic alteration, silicification, hematization, chloritization, bleaching, sericitization, carbonatization, and argillization. Where alteration is logged in the bedrock, it is typically low to moderately altered and the majority of the drill core shows no evidence of alteration. In each of the boreholes, the upper portion of the bedrock (ca. 100 m) tends to have the highest presence of moderately altered (A3) rock. This style of alteration is identified to penetrate the wall rock and create an envelope or halo of alteration around a given fracture or group of fractures. Lower alteration intensity (A2) tends to be generally confined to fractures and with little or no penetration of the alteration beyond the fracture. Deeper in the boreholes, the proportion of moderately altered rock decreases (although is still observed locally) and the bedrock is dominated by unaltered to weakly altered (A2) intervals.

Samples targeting alteration were sent to Actlabs for optical petrography to identify mineral assemblages and degree of alteration. The most common type of alteration observed in all samples was sericitization, which predominantly involved alteration of plagioclase crystal cores to fine-grained white mica. Samples logged as silicified, bleached and showing potassic alteration were all found to have varying degrees of sericitization and there was no evidence of secondary potassium feldspar or quartz/silica formation. What is identified in core as potassic alteration is, therefore, interpreted as either primary potassium feldspar or trace iron oxides (e.g., hematite) producing red staining. Chloritization, carbonatization, and hematization were all observed in thin section, but all instances were minor and generally targeted one mineral (e.g. primary biotite altering to chlorite).

Overall, at this point it is clear that bedrock alteration is present, but is generally weak and localizes on specific minerals. The current understanding is that alteration is associated with regional deformation and hydrothermal fluid flow, evidenced by the observation of alteration around fractures and accessory lithologies. As additional borehole drilling and field mapping is completed, our conceptual model will be updated to reflect the evolving understanding of the alteration assemblages.

4.2.3 Amphibolite Units

Amphibolite units are present to varying degrees in each of the drilled boreholes (Figure 23). These units deserve special attention because their occurrences, although volumetrically minor, are often associated with increases in fracture frequency, the increased presences of shear zones, quartz and calcite veining, and higher alteration intensities. In addition, in the context of spent nuclear fuel, the amphibolites tend to cluster at certain depths, and their presence could affect the bulk thermal conductivity of the solid rock. In geological core logging, the amphibolites contrast sharply with the predominantly felsic character of the remainder of the bedrock. The amphibolites consistently exhibit a well-defined foliation and sharp contact where they are adjacent to biotite granodiorite-tonalite, and an internal foliation is generally observed to align with the orientation of the contacts. A decimetre- to metre-scale hematite +/- sericitization and chloritization halo commonly envelops the amphibolites in the surrounding biotite granodiorite-tonalite. In addition, some fracture surfaces within the amphibolites are coated by chlorite. In geophysical logs the amphibolites consistently exhibit sharp increases in bulk density values and decreases in neutron values. Importantly, strain localization and penetrative deformation along observed contacts obscures any evidence of the primary relationship between the amphibolite occurrences and surrounding bedrock. At this point, it is unclear whether the amphibolite units had a tabular primary geometry, which may suggest that they intruded as mafic dykes, or if they were emplaced as xenoliths from the surrounding greenstone belts, or a combination of both.

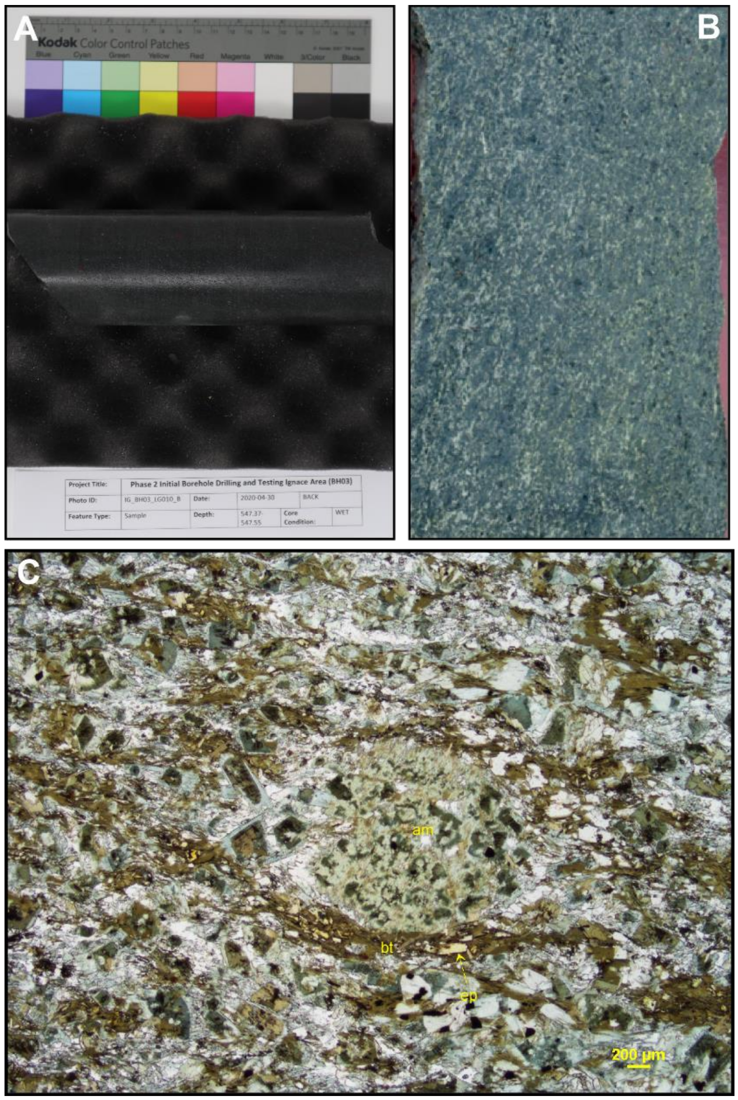

Figure 23: Representative examples of amphibolite (sample IG_BH03_LG010). A) Hand-sample photograph B) Billet photograph (billet size is 25 x 40 mm). C) Thin section photomicrograph with main rock-forming minerals amphibole (am; tremolite-actinolite), biotite (bt) and epidote (ep); plane polarized transmitted light.

Amphibolite contact orientations have been measured through geological core logging as alpha and beta values relative to the core axis, and also defined by a sinusoid trace overtop of a set of continuously oriented televiewer images. From the 29 amphibolites logged, true dip and dip direction information could be accurately obtained from 57 of 58 upper and lower contacts. In one occurrence, a contact could not be accurately traced because its contact relationship was obscured by a contact with a dark-colored feldspar-phyric tonalite dyke. Although there is some spread of contact orientations, as shown on Figure 24, the poles produce a relatively tight cluster overall, with a mean plane dipping 30º towards 348º.

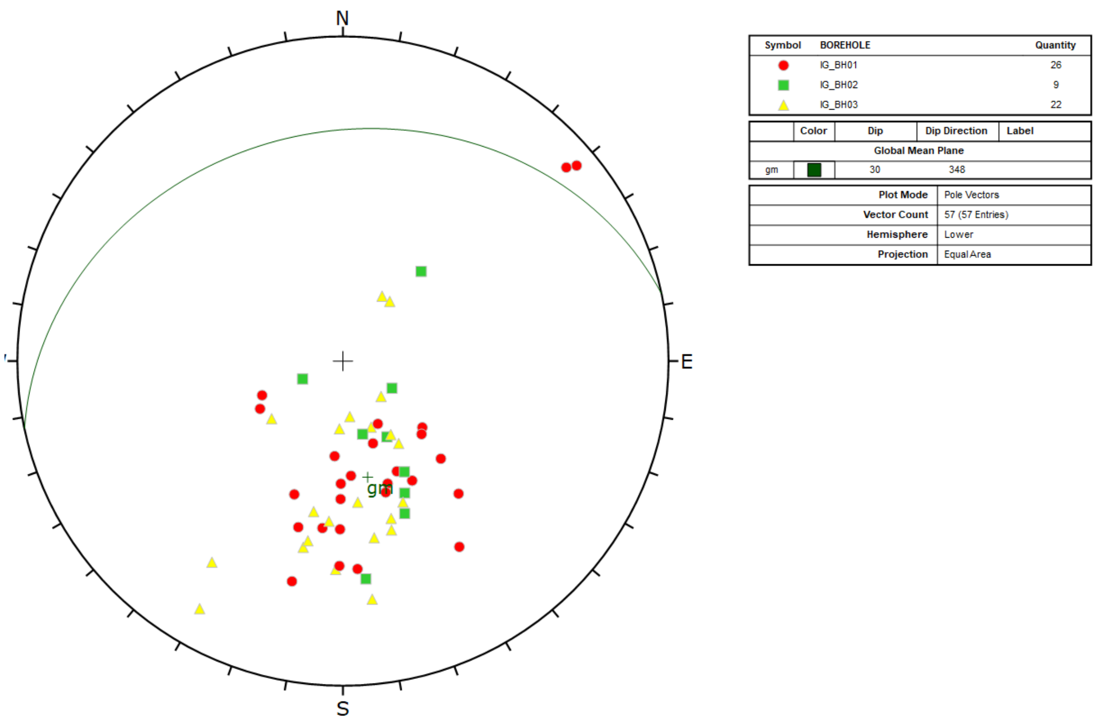

Figure 24. Amphibolite contact orientations from both upper and lower unit contacts. Orientations are defined by sinusoid trace using oriented televiewer images. Although there is a spread of contact orientations, the poles produce a tight cluster with a mean plane that dips 30º towards 348º.

Despite the uncertainty related to their genesis, these amphibolite units tend to be spatially grouped in broad, distinct, intervals in the boreholes. Therefore, the presence or absence of amphibolites within an otherwise extremely homogeneous granitoid body has been used as a main component in subdividing the subsurface geosphere, at the site-scale, into distinct rock unit domains. These rock unit domains, which are primary elements in the 3D geological modelling presented in this report, are discussed further in Section 4.2.7.

4.2.4 Felsic Dykes

As described above, felsic dykes of different composition are present to varying degrees in each of the drilled boreholes. This section presents rock type descriptions and orientation information for two sets of these felsic dykes, including, the aphanitic and feldspar-phyric tonalite dykes and the aplitic-granitic felsic dykes.

Aphanitic and feldspar-phyric tonalite dykes

The aphanitic tonalite dykes and feldspar-phyric tonalite dykes are visually and compositionally similar, exhibiting a characteristic dark grey-black aphanitic matrix and mineral composition of the dykes as quartz, plagioclase, and biotite with very minor K-feldspar. The only differentiator between these two rock types are the 1-5 mm albite phenocrysts identifying the feldspar-phyric end member. Representative examples of the aphanitic and feldspar-phyric tonalite dykes are shown in Figure 25. In core, these aphanitic and feldspar-phyric tonalitic dykes vary between undeformed and unaltered, with a primary intrusive relationship preserved, to exhibiting evidence of brittle-ductile deformation, intense strain localization both internally and along their contacts, and varying degrees of alteration. Also noteworthy is the fact that, in particular in IG_BH02, these aphanitic to felspar-phyric tonalite dykes are often spatially associated with high fracture frequency intervals. These particularly fractured intervals are discussed in further detail in Section 4.2.6 below.

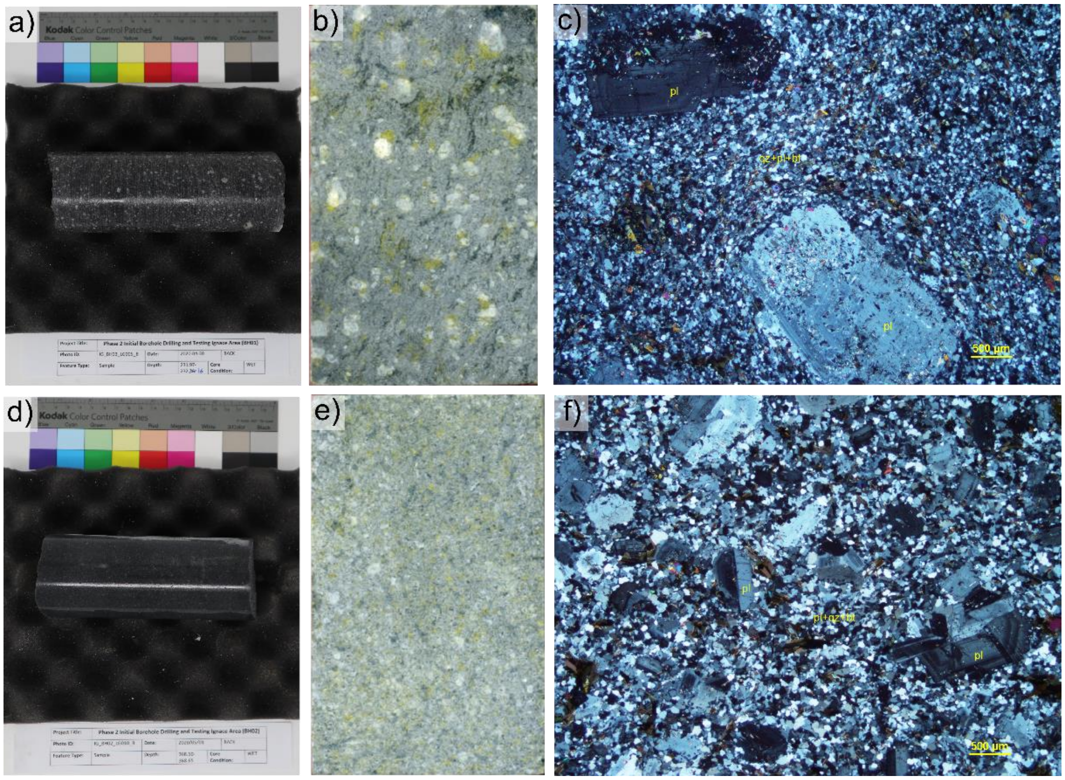

Figure 25. Representative samples of feldspar-phyric tonalite (IG_BH03_LG005; a-c) and aphanitic tonalite (IG_BH02_LG010; d-f) dykes. a) Hand-sample showing dark grey aphanitic matrix and visible mm-size albite phenocrysts. b) Thin section billet photograph showing foliation in groundmass wrapping phenocrysts. Billet has been etched with hydrofluoric acid and stained with sodium cobaltinitrite, which gives potassium-bearing minerals a yellow colour (interpreted as fine-grained K-feldspar, in this case; billet size is 25 x 40 mm). c) Thin section photomicrograph with 2-3 mm plagioclase phenocrysts (pl) and aphanitic groundmass composed of quartz, plagioclase, and biotite (qz+pl+bt). Groundmass foliation wraps the phenocrysts; crossed polarizers transmitted light. d) Hand-sample showing dark grey aphanitic groundmass and no visible phenocrysts. e) Thin section billet photograph showing small plagioclase phenocrysts and very minor yellow staining of K-feldspar (billet size is 25 x 40 mm). f) Thin section photomicrograph shows slightly coarser grain size in groundmass compared to c) and small 0.5 – 1.5 mm plagioclase phenocrysts (pl). Groundmass is composed of plagioclase, quartz, and biotite (pl+qz+bt) and foliation is not present in this sample; crossed polarizers transmitted light.

Aphanitic and feldspar-phyric tonalite dyke contact orientations have been measured through geological core logging as alpha and beta values relative to the core axis, and also defined by a sinusoid trace overtop of a set of continuously oriented televiewer images. From the 44 aphanitic and feldspar-phyric tonalite dyke occurrences, true dip and dip direction information could be accurately obtained from 85 of 88 upper and lower contacts. One occurrence, logged in the upper five metres of IG_BH02, could not be oriented due to the installation of conductor casing in the shallow bedrock. The other contact that could not be oriented was gradational in nature and so no distinct plane could be assigned to it. The spread in the orientation data is relatively broad, however the majority of the poles cluster in the southwest quadrant, defining steep to gentle dips towards the northeast, with fewer poles clustering in the northwest quadrant, defining gentle dips towards the southeast. The majority of these dykes are logged in

IG_BH02. However, dyke contact orientations from IG_BH01 and IG_BH03 show a similarity in orientations. Overall, the poles to the aphanitic and feldspar-phyric tonalite dyke occurrences define a mean plane dipping 27º towards 047º (Figure 26).

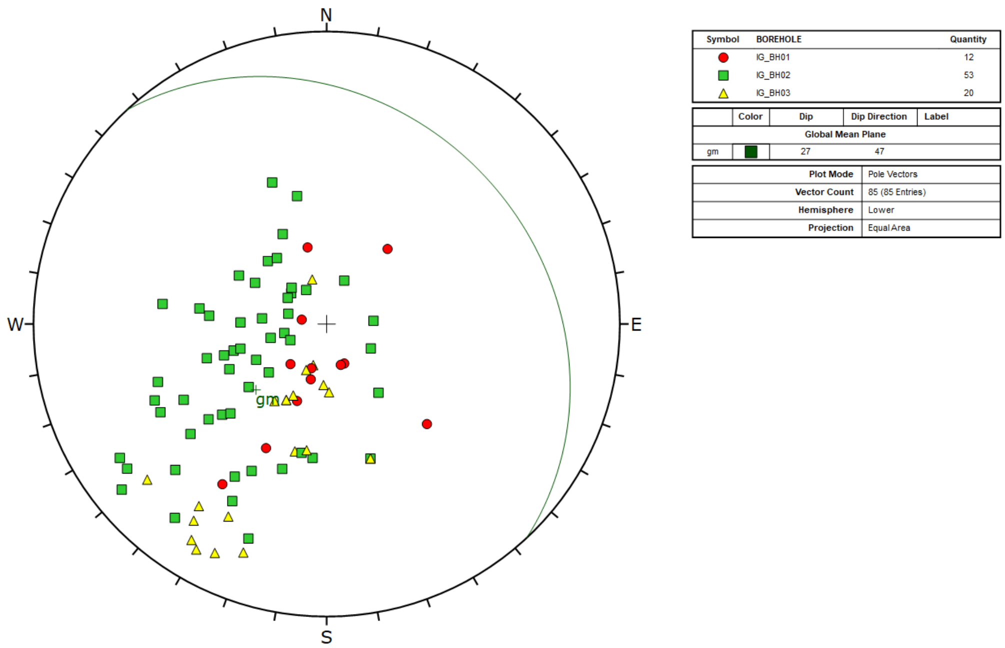

Figure 26. Aphanitic and feldspar-phyric tonalite dyke contact orientations from both upper and lower unit contacts. Orientations are defined by sinusoid trace using oriented televiewer images. Although there is a spread of contact orientations, the poles produce a tight cluster with a mean plane that dips 27º towards 047º.

Aplitic and granitic dykes

The aplitic and granitic dykes are compositionally similar, with main mineral phases of plagioclase, potassium feldspar, quartz and minor biotite. Both are equigranular, however, they are differentiated by grainsize, with the aplite occurrences being very fine-grained and the granitic occurrences being medium-grained. Representative examples of the aphanitic and feldspar-phyric tonalite dykes are shown in Figure 27. In core, the aplitic and granitic dykes appear massive and undeformed, with few (if any) internal fractures, and primarily exhibiting sharp and intact contacts with the host rock.

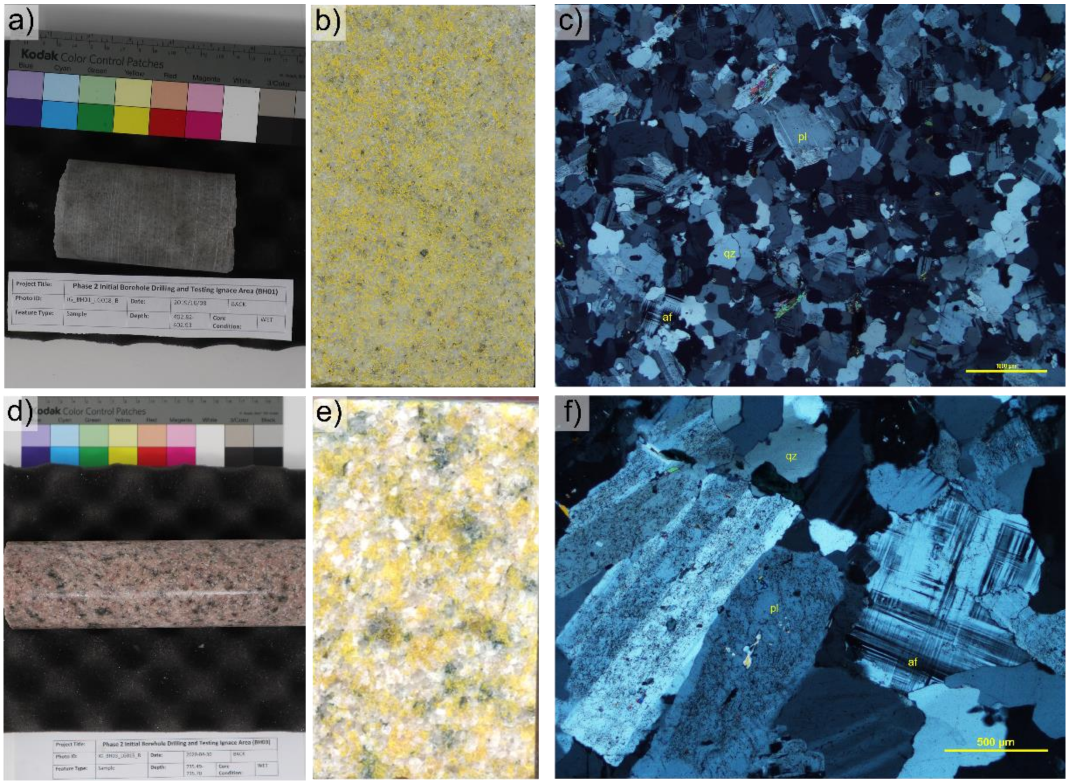

Figure 27. Representative samples of aplite (IG_BH01_LG018; a-c) and granite (IG_BH03_LG015; d-f) dykes. a) Hand-sample showing very fine grain size and white-grey colour. b) Thin section billet photograph showing massive texture and very fine grain size. Billet has been etched with hydrofluoric acid and stained with sodium cobaltinitrite, which gives potassium-bearing minerals a yellow colour (in this case, K-feldpsar; billet size is 25 x 40 mm). c) Thin section photomicrograph with rock forming minerals plagioclase (pl), quartz (qz), and K-feldspar (af). Note the fresh look of the minerals compared to the host biotite granodiorite-tonalite; crossed polarizers transmitted light. d) Hand-sample showing medium grain size and pink colour. e) Thin section billet photograph showing massive texture and medium grain size. Billet has been etched with hydrofluoric acid and stained with sodium cobaltinitrite, which gives potassium-bearing minerals a yellow colour (in this case, K-feldpsar; billet size is 25 x 40 mm). f) Thin section photomicrograph with rock forming minerals plagioclase (pl), quartz (qz), and K-feldspar (af). Note the larger grain size compared to the aplite dyke and the fresh look of the minerals compared to the host biotite granodiorite-tonalite; crossed polarizers transmitted light.

Aplitic and granitic dyke contact orientations have been measured through geological core logging as alpha and beta values relative to the core axis, and also defined by a sinusoid trace overtop of a set of continuously oriented televiewer images. True dip and dip direction information could be accurately obtained for all 24 aplitic and granitic dyke occurrences, including a total of 48 upper and lower contacts. The spread in the data is relatively broad, however the majority of the poles cluster in the southwest, with steep to moderate dips towards the northeast, or in the southeast, with steep to moderate dips to the northwest. Overall, the poles to the aplitic and granitic dyke occurrences define a mean plane dipping 43º towards 015º (Figure 28).

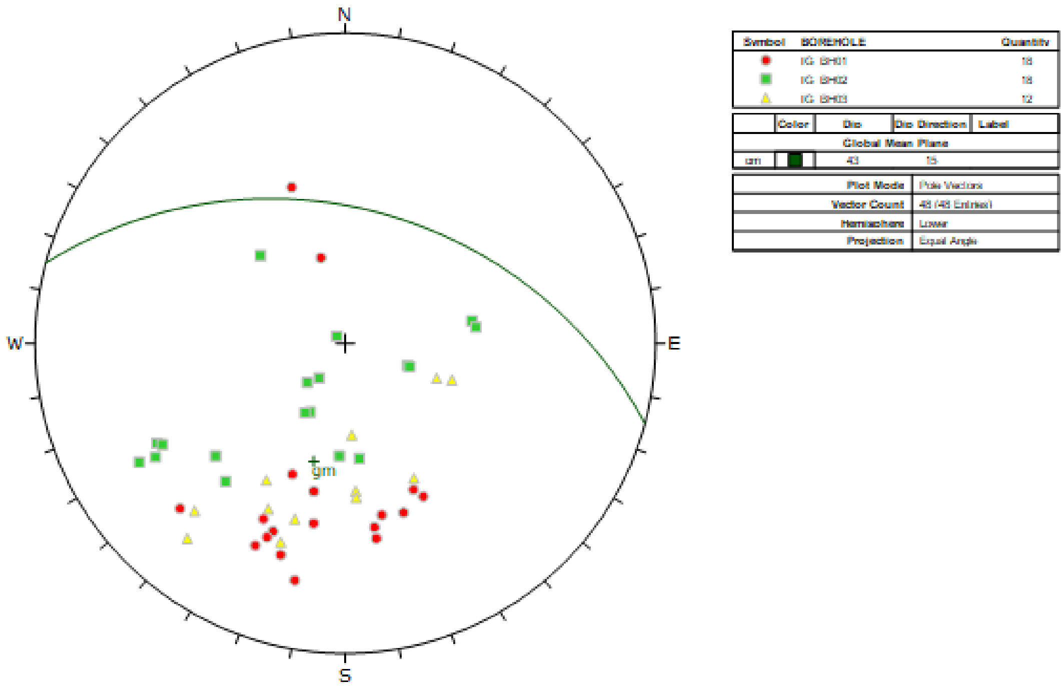

Figure 28. Aplitic and granitic dyke contact orientations from both upper and lower unit contacts. Orientations are defined by sinusoid trace using oriented televiewer images. Although there is a spread of contact orientations, the poles produce a tight cluster with a mean plane that dips 43º towards 015º.

4.2.5 Borehole Integrated Structural Characteristics

In this initial model, borehole fracture frequency data is used specifically to develop the structural unit domains which are incorporated into the geological model. In this section, fractures are described based on combined structural logs from the single borehole integration reports (Parmenter et al. 2021a, 2021b and 2021c, and Figure 29). The term fracture corresponds to a planar discontinuity in the rock, classified as a joint, fault, or vein (JN, FLT, VN). A thorough analysis of fracture sets and characteristics for the geosphere will be described in a separate report.

Figure 30a presents the combined fracture poles measured in the three boreholes and pole densities are contoured. Because each of the boreholes is drilled at different inclinations and azimuths, it is important to account for the probability of intersecting near vertical fractures in each of the boreholes separately. Therefore, prior to combining the data, fracture densities were corrected using a Terzaghi correction to reduce the bias associated with borehole orientation (Terzaghi, 1965). Figure 30b presents the Terzaghi-weighted fracture pole densities from the three boreholes combined.

In general, groupings of fracture poles can be discerned in the unweighted and weighted stereonet plots. Based on the unweighted stereonet, a shallow dipping set (a) of fracture poles is defined. This set has been logged in each of the boreholes and is present at any given depth. Although not confined to any particular rock type, their occurrences commonly cluster within and adjacent to the amphibolite units in each of the boreholes.

The Terzaghi-weighted fracture pole densities presented in Figure 30b better highlight the moderate to steeply dipping fracture poles. Set (b) presents a cluster of fracture poles that are moderately to steeply dipping in a southeasterly direction. By presenting the fractures by unique fracture types (joint, vein, and fault), fracture set (b) may have a higher proportion of veins compared to other fracture pole sets. Also noteworthy is that set (c) and set (d) represent the same subvertical to vertical set of NW-SE striking fractures, and that set (e) represents a fourth, steeply-inclined and west-dipping, fracture set. In addition, when comparing the orientations of the felsic dykes, presented above in Section 4.2.4, it is evident that the poles to the aphanitic and feldspar-phyric dykes both overlap with set (a) and set (c) fractures and are also broadly distributed between these two fracture set orientations. In addition, the poles to the aplitic to granitic dykes also tend to overlap with set (c) fractures.

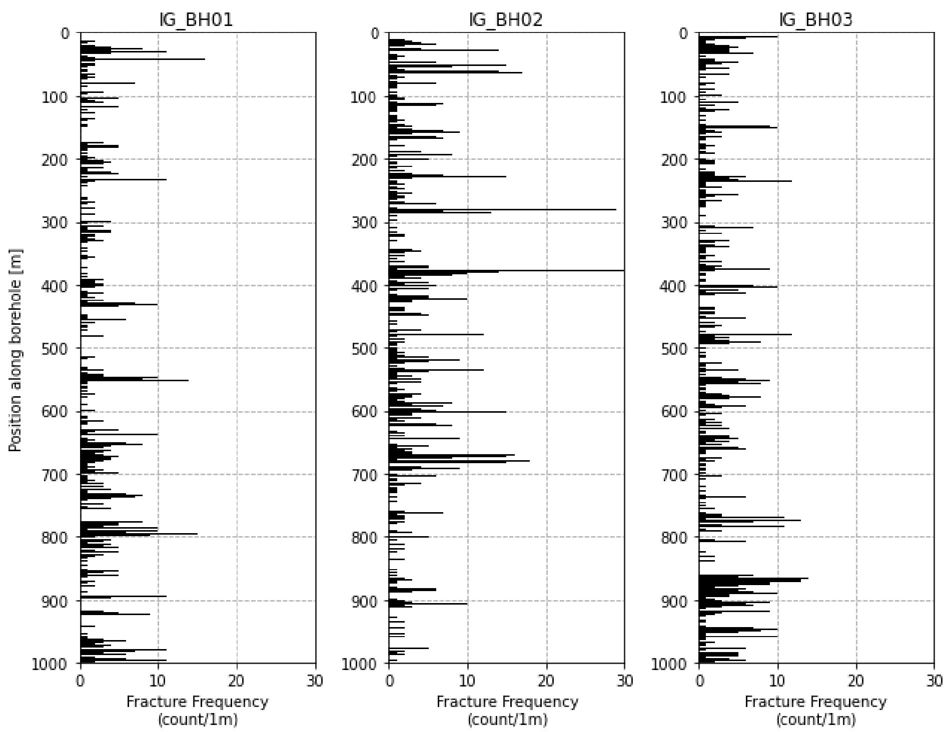

Figure 29. Fracture count per metre calculated in boreholes IG_BH01, IG_BH02 and IG_BH03. Frequency is based the integration of core logged and televiewers logged structures. The term fracture refers to joints, veins and faults. Position is along the borehole axis.

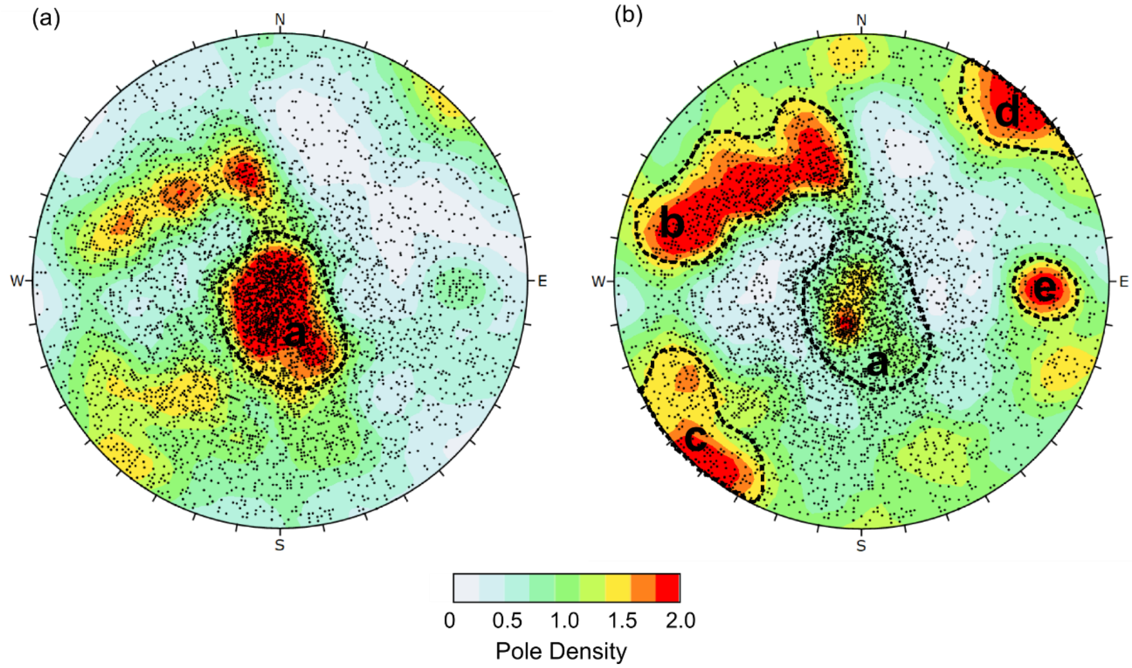

Figure 30**. Stereonet of poles to fracture planes (joint, vein and fault) from three boreholes; IG_BH01, IG_BH02, IG_BH03 combined. (a) distributions of poles with contoured pole density, and (b) distributions of poles with Terzaghi-weighted pole densities contoured. Black dashed outlines present general clusters for the purpose of discussion in the report; detailed cluster analyses will be completed in a separate report.**

4.2.5.1 Primary and Ductile Structure Characteristics

Primary and ductile structural characteristics, including igneous primary structures, a foliation, and ductile and brittle-ductile shear zones, were logged in all three deep boreholes. A summary of the characteristics of each of these structure types, including their orientations, is included below.

Igneous primary structures include features interpreted to have originated with the formation or emplacement of the igneous rock, including igneous flow foliation and igneous layering. These features are generally characterized by sharp to gradational changes in grain size or concentration of the main rock-forming minerals in the granodiorite-tonalite bedrock, including biotite, quartz, or plagioclase. There does not appear to be any inherent weakness, or competency contrast, in the bedrock at the transitions marked by these layers. Poles to the planes of these primary features are broadly distributed but predominantly concentrate in the northwest quadrant of the stereonet defining moderately inclined planes that dip towards the southeast (Figure 31a). There is very little difference between the unweighted and weighted data sets.

Foliation was primarily identified by the preferential alignment of biotite grains in the matrix of the biotite granodiorite-tonalite, or by aligned amphibole grains in amphibolite occurrences. In the majority of occurrences within the biotite granodiorite-tonalite, the foliation was logged as weak. However, a biotite foliation was locally well-developed in association with logged shear zones. In the amphibolite, the foliation was heterogeneously distributed but generally well-developed where observed. Overall, the poles to all foliation planes, from the three boreholes combined, are mostly distributed within a broad north-northwest to south-southeast trending girdle (Figure 31b). One dominant pole cluster, identified in both the unweighted and weighted data sets, defines steeply inclined foliation planes that dip towards the north-northwest. This latter pole cluster is slightly more steeply inclined than the logged amphibolite contacts.

Brittle-ductile and ductile shear zones were initially logged as separate structure types during the geological core logging. In the assessment of the entire shear zone dataset, it was determined that these structures more likely represent a continuum of ductile to brittle deformation. Shear zones identified within the biotite granodiorite-tonalite are characterized by single mm-scale shear planes, anastomosing or parallel sets of several mm-scale shear planes, or, as decimeter-scale zones of strain localization. A quartz infilling is prevalent within these occurrences. Shear zones are also typically developed in association with amphibolite occurrences. Amphibolite contacts exhibit evidence of penetrative ductile to brittle-ductile shear deformation obscuring any indication of their primary relationship with the surrounding bedrock and amphibolite contact orientations generally overlap with those of the gently inclined shear zones. Internally, amphibolites exhibit heterogeneous deformation varying between massive and undeformed through to m-scale shear zones with locally developed mylonitic layering. Some feldspar-phyric and aphanitic tonalite dykes also exhibit evidence of strain localization and shear deformation, though not as universally as the amphibolite occurrences.

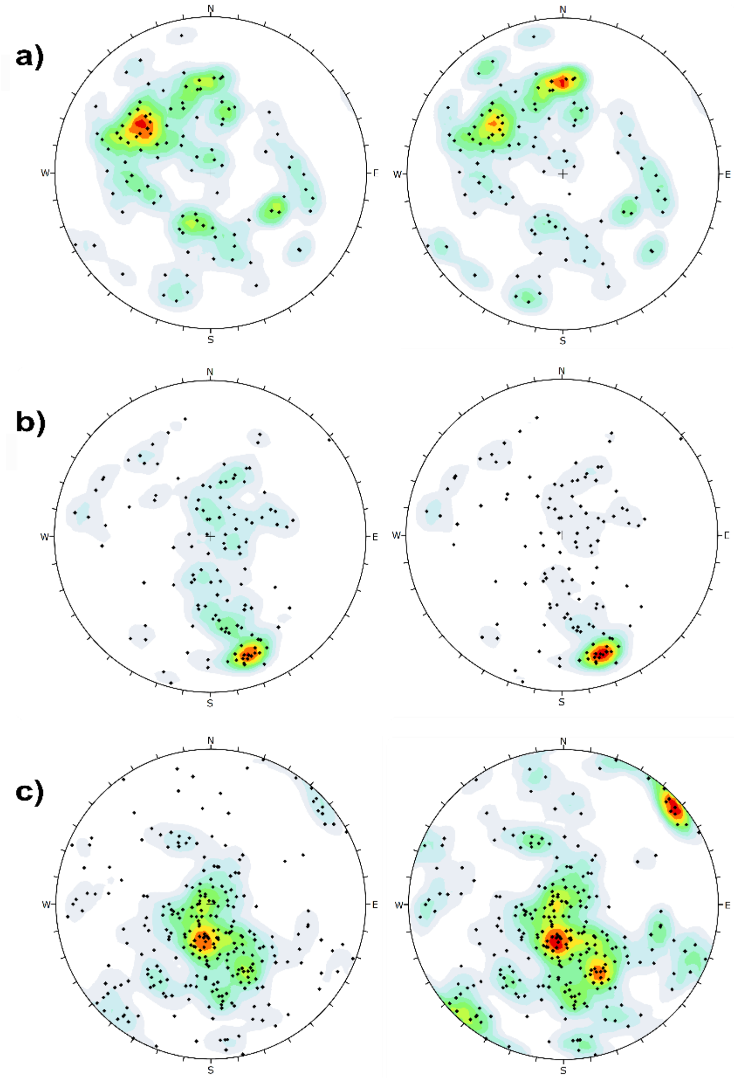

Figure 31. Compilation of poles for primary igneous and ductile planar structures from the first three boreholes (IG_BH01, IG_BH02, and IG_BH03). Unweighted data is shown on the left and Terzaghi-weighted data is shown on the right. a) Igneous primary structure which represents primary layering recognized in the bedrock; b) foliation defined by weak to moderate biotite alignment within the biotite granodiorite-tonalite unit or by aligned amphiboles in amphibolites; and c) shear zones categorized as either brittle-ductile or ductile (SHR and SHRD) plus a few logged mylonite (MYL) occurrences.

Quartz, chlorite, calcite, epidote, and hematite are common secondary minerals associated with shear zones in the amphibolite and tonalite dyke occurrences. There is a broad distribution of poles to shear zones in the combined dataset. However, one clear pattern that emerges in the combined borehole dataset is a broad, shallowly inclined to sub-horizontal, pole cluster defining shear planes that dip predominantly towards the north-northwest (Figure 31c). This pole cluster overlaps with the shallowly-dipping to subhorizontal set of fractures, presented in Figure **30**, which is also common to all three boreholes. This shear zone pole cluster also overlaps with the distribution of poles to the amphibolite occurrences, presented in Figure 27 above, though the amphibolite contacts tend to exhibit a slightly greater dip magnitude. One additional prominent pole cluster, which is emphasized in the weighted data set, defines shear plane that are steeply inclined (nearly vertical) and dip southwest. This pole cluster is also evident in both the fracture set and amphibolite contact datasets.

The relationship between the prominent pole cluster in the foliation data set and the shallowly inclined and north-northwest dipping shear zones is suggestive of a common characteristic of ductile deformation zones in heterogeneously deformed rocks, including granitoid bodies, where a foliation is developed at an oblique angle to a shear zone boundary (e.g., Berthe et al., 1979). This relationship would imply that the shallowly inclined and north-northwest dipping shear zone orientation is a fundamental structural characteristic of the Revell site. Furthermore, the overlap in orientation between several of the brittle and ductile structural trends, and the contacts of the amphibolite and felspar-phyric and aphanitic tonalite dykes, at the Revell site is consistent with the understanding that structures in deformed granitoid rocks commonly evolve through a cycle of brittle-ductile-brittle deformation throughout their history (e.g., Pennacchioni et al., 2006; Pennacchioni and Macktelow, 2007). These relationships will be explored further in presentation of a conceptual geological model for the Revell site in Section 4.3.

4.2.5.2 Linear Structures

Lineations were identified on fault planes, shear planes (including mylonite), and, to a lesser extent, foliation planes from all boreholes during geological core logging. Most lineations identified during geological core logging are characterized as slickenlines on fault planes. The most common minerals identified as defining these lineations are chlorite and epidote, with lesser occurrences defined by alignment of quartz, muscovite, and calcite. The mineral lineations associated with the shear zones and mylonite occurrences are defined by a similar assemblage of quartz, chlorite, epidote, and calcite. The mineral lineations identified on the foliation planes are defined by quartz.

The combined data set of lineations from all three boreholes are shown in Figure 32. Overall, there is a relatively variable distribution in lineation trends. However, most lineations plunge gently northwest or, less commonly, towards the north. Overall, the combined pattern of lineations broadly outlines a great circle that dips gently towards the north or northeast. Importantly, these lineations lie within the plane defined by the prominent pole cluster of gently dipping shear zones, shown in Figure 31c.

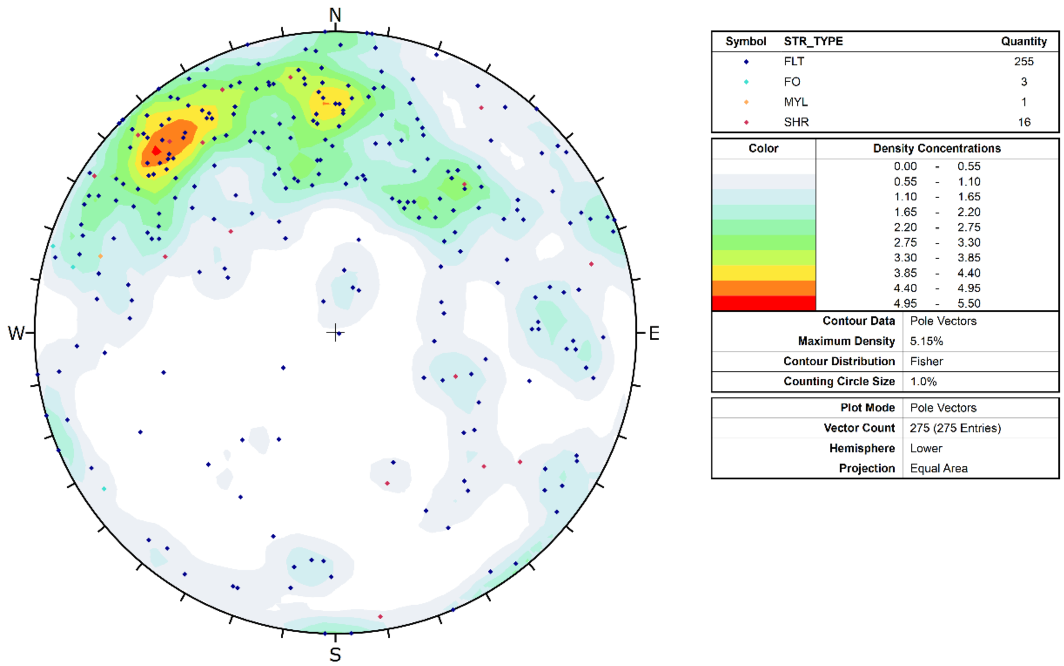

Figure 32: Compilation of lineations (n=275) from the first three boreholes (IG_BH01, IG_BH02, and IG_BH03).

4.2.6 High Fracture Frequency Intervals in Boreholes

High fracture frequency intervals (HFFI) are defined within each of the three boreholes, IG_BH01, IG_BH02 and IG_BH03, and the outcome of the analysis is summarized here. HFFI represent a cluster of faults, joints and/or veins that exceeds a minimum relative fracture intensity threshold along a distinct borehole length. Detailed analyses are documented in the individual single borehole integration reports (Parmenter et al. 2021a, 2021b and 2021c). A summary table for each of the boreholes can be found in their respective single borehole integration reports. Table 4 presents the compilation of HFFI for the three boreholes documented in this report using the same analysis procedure.

The distribution of fracture frequency (Figure 33) and their statistics over the length of each borehole provides justification for defining HFFI in the subsurface. Within the boreholes, these intervals are primarily dominated by brittle fracturing and locally may also comprise a few minor ductile shear zones. HFFI may comprise fractures that share similar orientations within a single fracture set or may comprise a range of orientations. Fracture summaries provided in the single borehole integration reports (Parmenter et al. 2021a, 2021b and 2021c) provide details on fracture sets, fracture types and fracture mineral infilling, which may support decisions on HFFI identification. In this report we attempt to correlate HFFI with lineaments that were interpreted based on remote sensing data on the ground surface (Section 5.5.2).

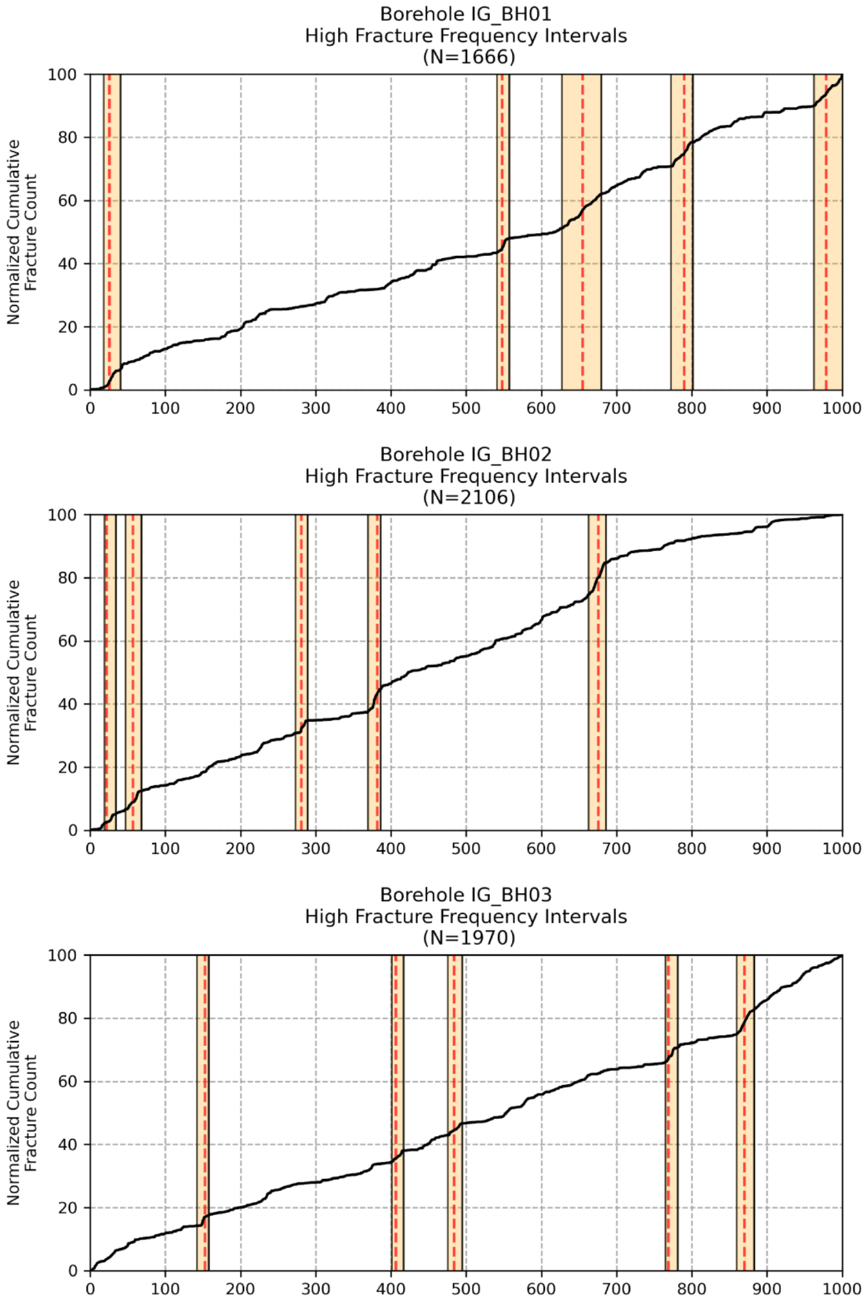

Figure 33. High fracture frequency intervals interpreted visualized with cumulative fracture logs for boreholes IG_BH01, IG_BH02, and IG_BH03. High fracture frequency intervals (HFFI) are outlined by their yellow bands. The red dashed line represents the peak location.

Table 4. High fracture frequency intervals (HFFI) identified in boreholes IG_BH01, IG_BH02, and IG_BH03 (Parmenter et al. 2021a, 2021b and 2021c).

BHID	Peak Position [m]	Top Position [m]	Bottom Position [m]	Interval Length [m]	Identifier
IG_BH01	26	18.6	40.17	21.57	IG_BH01_HFFI_1
IG_BH01	548	541	557.27	16.27	IG_BH01_ HFFI _2
IG_BH01	655	627.5	679.75	52.25	IG_BH01_ HFFI _3
IG_BH01	790	772.4	801.75	29.35	IG_BH01_ HFFI _4
IG_BH01	979	962.25	1001.18	40.61	IG_BH01_ HFFI _5
IG_BH02	22	19.11	34.38	15.27	IG_BH02_ HFFI _1
IG_BH02	57	51.06	67.94	16.88	IG_BH02_ HFFI _2
IG_BH02	281	272.84	289.33	16.49	IG_BH02_ HFFI _3
IG_BH02	382	369.78	386.62	16.84	IG_BH02_ HFFI _4
IG_BH02	676	662.94	686.14	23.2	IG_BH02_ HFFI _5
IG_BH03	153	142.3	157.7	15.4	IG_BH03_ HFFI _1
IG_BH03	407	400.83	416.5	15.67	IG_BH03_ HFFI _2
IG_BH03	484	476.75	494.58	17.83	IG_BH03_ HFFI _3
IG_BH03	769	764.33	781.6	17.27	IG_BH03_ HFFI _4
IG_BH03	870	860	882.5	22.5	IG_BH03_ HFFI _5

* *all position and length measurements here are along their respective borehole axis*

Each of the fracture intervals defined from the three boreholes are evaluated on stereonets to further determine the orientation distributions and define one or more orientations that are characteristic of the interval. Dominant orientations are interpreted manually as the maxima defined by the Terzaghi-weighted pole density and presented in the single borehole integration reports (Parmenter et al. 2021a, 2021b and 2021c). The resulting fracture orientations from within the fracture intervals can provide input into modelling such zones as surfaces in deterministic fracture network models.

4.2.6.1 Subhorizontal Fractures from boreholes

A high proportion of subhorizontal fractures were logged in the initial three boreholes and an analysis of their vertical frequency distribution and character is presented here. For this analysis, subhorizontal fractures are defined as those with dips ranging between 0 and 30° and the term fracture refers to joints, faults, and veins based on the integration of geological core logged and televiewer logged structures. Figure 34 presents the subhorizontal fracture frequency calculated per 5 metre intervals versus the depth along the borehole. Locally, these subhorizontal fractures tend to cluster within the borehole and can be interpreted on the fracture frequency log as discrete intervals. Specifically, in IG_BH02, a well-defined cluster is apparent at 375 m depth along the borehole.

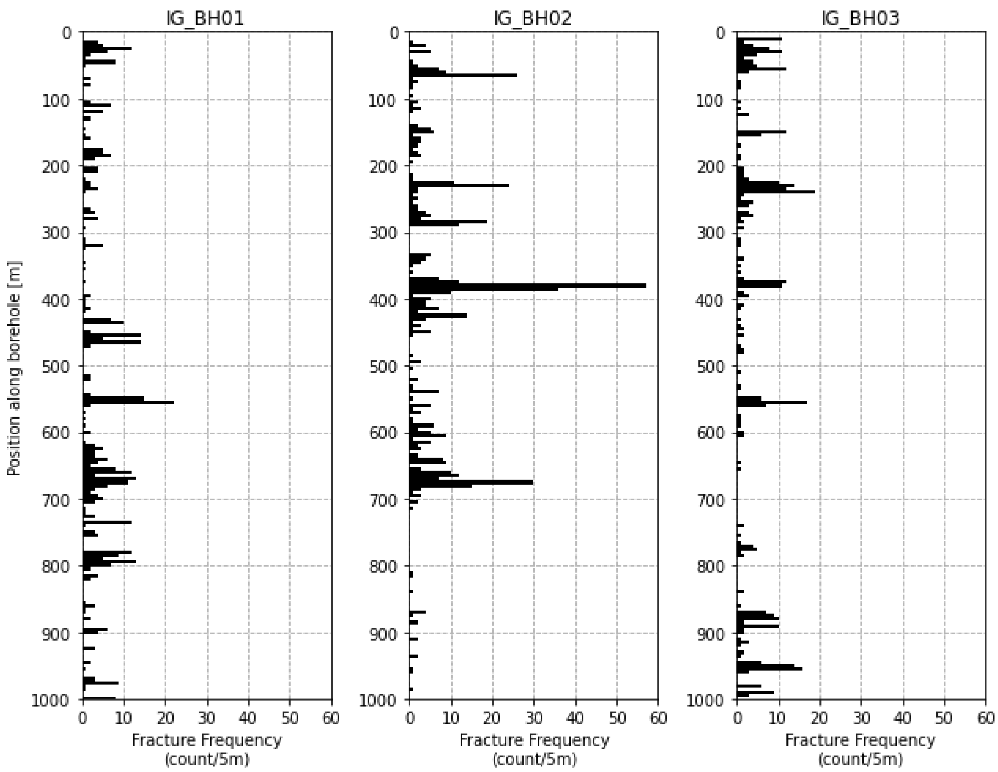

Figure 34. Vertical frequency of subhorizontal fractures per 5 metre interval calculated in boreholes IG_BH01, IG_BH02 and IG_BH03. Subhorizontal fractures here are defined with dip magnitudes ranging between 0 and 30 degrees. Frequency is based the integration of core logged and televiewers logged structures. The term fracture refers to joints, veins and faults. Depth is along the borehole axis.

Using a modified fracture frequency peak identification workflow (similar to the HFFI) several fracture intervals can be interpreted in all three boreholes. Figure 35 presents the normalized cumulative fracture count, the fracture frequency, and the moving average fracture frequency for the subhorizontal fractures from IG_BH02 as an example. The modification to the algorithm involved reducing the prominence threshold value from 4 to 2, which enables picking intervals with smaller relative peak magnitudes. As a result, 5 subhorizontal fracture frequency intervals have been identified from IG_BH02. Using the same workflow, 4 intervals are defined in IG_BH01 and 4 intervals are defined in IG_BH03. These intervals will be of particular interest when processing and interpreting seismic reflection data within the site. However, these intervals are not directly incorporated into the geological modelling workflow at this stage.

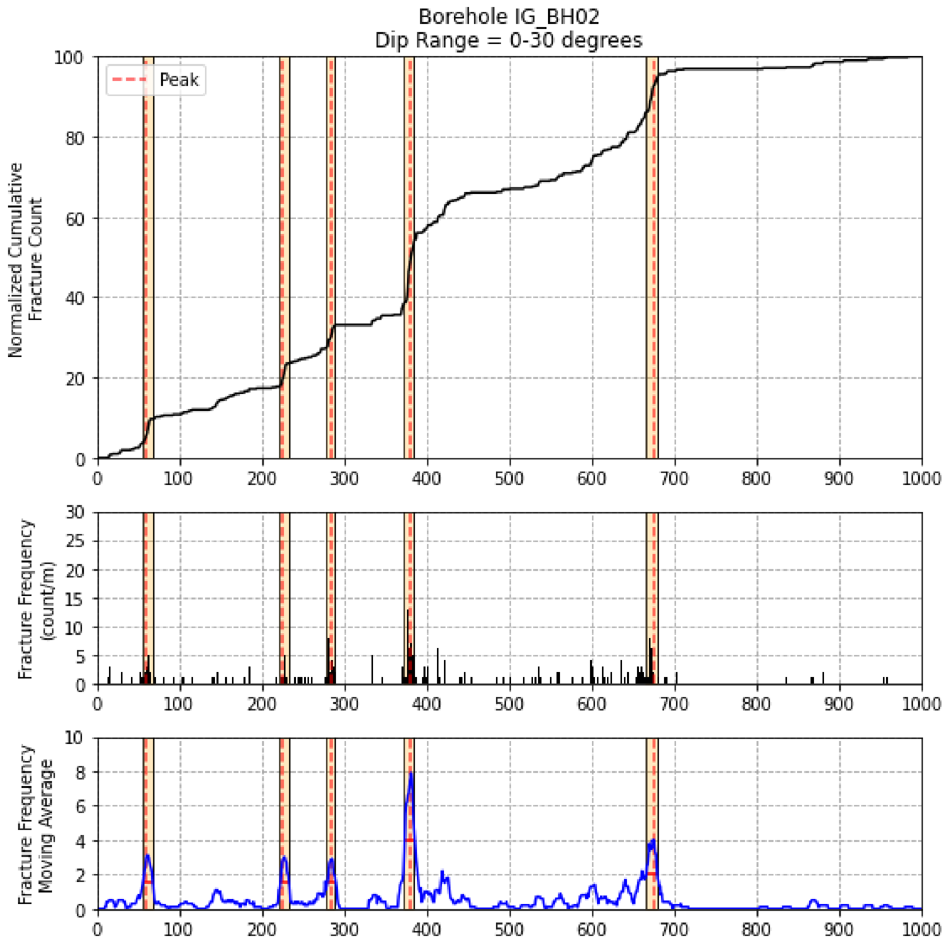

Figure 35. Normalized cumulative fracture count, the fracture frequency, and the moving average fracture frequency for the subhorizontal fractures from IG_BH02. Subhorizontal fractures here are defined with dip magnitudes ranging between 0 and 30 degrees. Frequency is based the integration of core logged and televiewers logged structures. The term fracture refers to joints, veins and faults. Depth is along the borehole axis. Five subhorizontal fracture frequency intervals have been identified (yellow)

4.2.7 Integrated Rock Unit and Structural Unit Domains

Rock unit (RU) and structural unit (SU) domains are defined for each individual borehole based on data interpreted within single borehole integration reports (Parmenter et al. 2021a, 2021b and 2021c). Interpreted rock unit and structural unit tops and bottoms are imported to the site-scale geological model at drilled depths along the trajectory of each borehole.

Rock units (RU) were defined as a borehole length primarily on the basis of dominant rock type and/or combination of rock types (and, if applicable, alteration and weathering types) that are considered distinct from adjacent parts of the borehole. Rock types within each interpreted RU are distinguished on the basis of their composition, grain size and petrophysical properties measured during geophysical logging and laboratory analysis. The geologically core logged rock types, combined with key continuous geophysical datasets, were used to distinguish distinct lithological associations within each RU and define the top and bottom interval depths.

A structural unit is a borehole length comprising a relatively uniform per metre fracture frequency that is distinct from adjacent parts of the borehole. Structural units have been defined to capture the general variation in fracture frequency along the length of the borehole, primarily on the basis of broad changes in slope visible in the cumulative fracture frequency curve (Parmenter et al. 2021a, 2021b and 2021c). This curve was derived using the fracture dataset (i.e., joints, veins, and faults, including broken and intact/partially intact structures).

The single borehole integration reports identified up to four rock units within a given borehole. Based on similarity in the rock types and geophysical characteristics presented in each unit, in some cases rock units were classified more than once within the same borehole. In such a case, multiple interpretations of the same unit in a borehole are denoted by sequential lettering appended to the end of the rock unit identifier (see Table 5 for example RU1a and RU1b occurring at different depth intervals in IG_BH01).

The input data were re-evaluated to determine appropriate rock units for the purpose of modeling between boreholes. This step requires analyzing all available input data together to determine spatial correlations of similar or differing characteristics, in particular between subsurface borehole data and surface data. Evaluation of the rock units from boreholes IG_BH01, IG_BH02 and IG_BH03, as part of this report, resulted in a reclassification of the rock units into integrated rock unit (IRU) classes. This integration is based on similarity or differences observed between multiple boreholes that were drilled. The Integrated rock units derived from boreholes IG_BH01, IG_BH02 and IG_BH03 resulted in three distinct integrated rock units (IRU1, IRU2 and IRU3) that are observable in the boreholes (see Table 5 and Figure 36a). As additional borehole integration results are developed, the data may need to be re-compiled to ensure domains are selected based on similar criteria. The single borehole integration reports identified between 3 and 5 structural units for each borehole. However, in some cases, structural units within individual boreholes resulted in classification of the same unit based on the slope of the cumulative fracture frequency curve (see Table 6 for example SU1 and SU3 occurring at different depth intervals in IG_BH03).

Table 5. Rock unit interval top and bottom depths along drilled boreholes. Rock unit (RU) represents the interpretation domain based on the single borehole integration report, whereas the integrated rock unit (IRU) represents common domains identified in each of the boreholes.

	Top Position	Bottom Position	Rock Unit (RU)	Integrated Rock Units (IRU)
IG_BH01	0	180.01	RU1a	IRU1a
	180.01	242.5	RU2	IRU2
	242.5	653.71	RU1b	IRU1b
	653.71	1001.17	RU3	IRU3
	Top Position	Bottom Position	Rock Unit (RU)	Integrated Rock Units (IRU)
IG_BH02	0	535.14	RU1a	IRU1a
	535.14	678.28	RU2	IRU3
	678.28	1001.21	RU1b	IRU1b
	Top Position	Bottom Position	Rock Unit (RU)	Integrated Rock Units (IRU)
IG_BH03	0	545.6	RU1a	IRU1a
	545.6	898.97	RU2	IRU3
	898.97	1001.21	RU1b	IRU1b

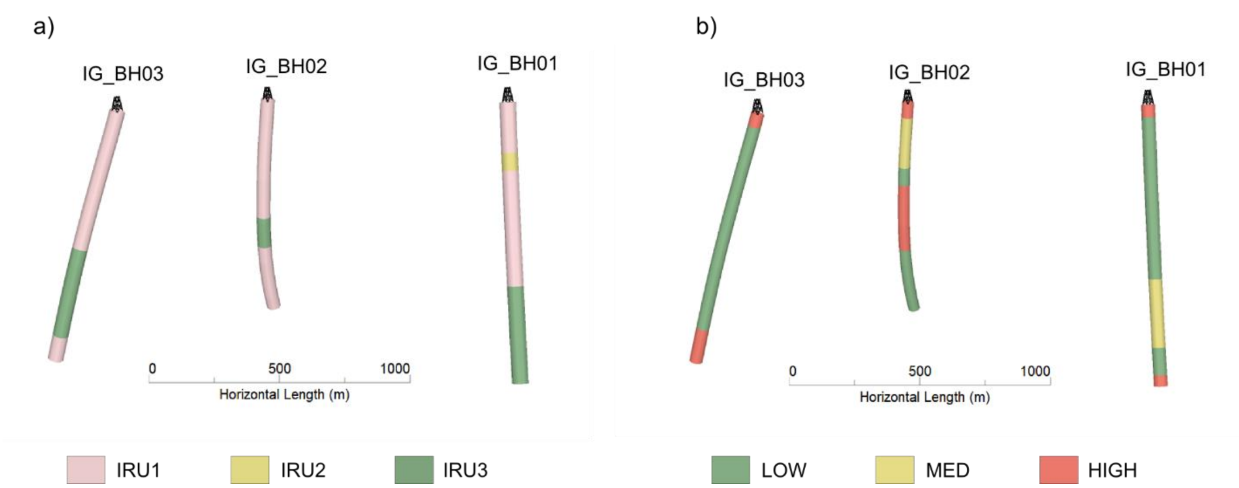

Figure 36. Borehole view showing vertical distribution of a) IRU and b) ISU model domains (bins of low, medium and high represent fracture intensity groupings based on mean fracture counts).

Similar to rock unit domains, input data for structural units were also re-evaluated to determine appropriate domains for the purpose of modeling between boreholes. This step requires analyzing the available data together to determine similar or differing characteristics between the boreholes. The evaluation involved reviewing the determined mean fracture counts and standard deviations for each of the defined structural unit intervals. These metrics were used to evaluate similarity or differences between each interval by grouping the values into bins defined by percentile thresholds. The objective here was to group these intervals into three bins of low, medium and high mean fracture counts. Evaluation of data from boreholes IG_BH01, IG_BH02, and IG_BH03 as part of this report resulted in a grouping of the structural units into integrated structural unit (ISU) classes using the 33rd and 67th percentiles as threshold values (see Table 6 and Figure 36b). However, it is acknowledged there are a variety of approaches that could be implemented to subdivide these intervals into groups, and as additional borehole integration results are developed the data may need to be re-compiled to ensure domains are selected based on similar criteria.

Table 6. Structural unit interval top and bottom depths along drilled boreholes. Mean fractures per metre and standard deviations are presented as metrics to compare the units between boreholes. Structural unit (SU) represents the interpretation domain based on the single borehole integration report, whereas the integrated structural unit (ISU) represents common domains identified in each of the boreholes.

	Top Position	Bottom Position	Mean Fracture/m	Standard Deviation (counts/m)	Structural Unit (SU)	Integrated Structural Unit (ISU)
IG_BH01	0	44.06	3.11	3.56	SU1	HIGH
	44.06	619.45	1.21	1.89	SU2	LOW
	619.45	862.68	2.43	2.51	SU3	MED
	862.68	961.2	0.74	1.93	SU4	LOW
	961.2	1001.18	4.15	2.98	SU5	HIGH
	Top Position	Bottom Position	Mean Fracture/m	Standard Deviation (counts/m)	Structural Unit (SU)	Integrated Structural Unit (ISU)
IG_BH02	0	65.5	4.05	4.46	SU1	HIGH
	65.5	291	2.1	3.05	SU2	MED
	291	370.5	0.81	1.53	SU3	LOW
	370.5	683	3.12	4.11	SU4	MED
	683	1001	1.06	1.82	SU5	LOW
	Top Position	Bottom Position	Mean Fracture/m	Standard Deviation (counts/m)	Structural Unit (SU)	Integrated Structural Unit (ISU)
IG_BH03	0	51	3.42	3.01	SU1	HIGH
	51	860.5	1.61	2.48	SU2	MED
	860.5	1000.54	3.51	2.97	SU3	HIGH

4.3 Conceptual Geological Integrated Summary

Based on the data sets available and described in the previous section, we present an early conceptual understanding of the bedrock geology at the site. The development of this conceptual model provides a starting point for 3-dimensional geological model development. The current conceptual understanding and resulting geological model are based on limited data availability and are expected to be updated as future information is collected through additional site investigations.

The main geological characteristics that inform the development of an initial site-scale conceptual geological model for the Revell site are described below and shown in Figure 37. This includes an extremely homogeneous, Archean granitoid rock association composed primarily of biotite granodiorite-tonalite to biotite tonalite (representing more than 97% of the bedrock encountered in the three drilled boreholes), accessory felsic dykes and amphibolite. Though minor by volume, the amphibolite occurrences in all boreholes represent marker units that are useful to subdivide the otherwise homogeneous bedrock into distinct, gently dipping rock units. The integrated rock unit labelled IRU3 is characterized by the presence of biotite granodiorite-tonalite + amphibolite. Correlation of the upper and lower rock unit boundaries to neighbouring boreholes results in surfaces that dip gently towards the north at ~5-10º. As noted above, the average amphibolite contact orientation across the site has a slightly steeper mean dip angle of 30º towards the north (348º).

A low volume of felsic dykes is also present at the site-scale, as described above in Section 4.2.4. There appear to be at least two distinct suites of felsic dykes, including a suite of aphanitic to feldspar-phyric tonalite dykes, and a suite of dykes with a more granitic composition, including aplitic and granitic dykes, with much lesser pegmatite. The aphanitic to feldspar-phyric tonalitic dykes are overprinted by varying degrees of ductile to brittle deformation. In some occurrences primary intrusive relationships are preserved at the bedrock interface and these dykes look fresh and unaltered. In other occurrences, they are overprinted by weak to intense ductile and/or brittle deformation, and weak to intense alteration, similar to the character of the amphibolites. The contact orientations of the tonalitic dykes vary from gently to moderately inclined, overlapping with those of the amphibolites, to more steeply inclined occurrences. The granitic dykes, in contrast, do not appear to exhibit evidence of ductile deformation. They are generally steeply to moderately inclined, weakly altered, and sparsely fractured.

Regarding a conceptual presentation of the bedrock structure at the site-scale, a gently inclined, north-dipping to subhorizontal structural grain in the bedrock is prominent in the borehole shear zone and fracture data sets, as well as the surface mapping fracture data set. In the conceptual model below, this structural grain is represented by a discontinuous network of subhorizontal to gently inclined fracture zones. This representation is consistent with the understanding that subhorizontal fractures are clustered as discrete intervals along all three boreholes. A more connected network of intact, localized, ductile shear zones is inferred to be present in the rock mass but is not explicitly shown in the conceptual model below. The overall geometry of the rock units follows approximately the same structural grain. With the relative sparsity of subsurface information available, (only three deep boreholes in a crystalline rock environment), this gently inclined structural grain is a valuable guide for defining the shape and geometry of the rock unit and structural unit domain models away from the borehole locations where they are observed.

Steeply inclined fracture zones that represent the combined surface traces of interpreted lineaments and their subsurface projections are a prevalent feature of the conceptual model. These inferred fracture zones are characterized by narrow haloes of increased fracture density and a degree of alteration that is higher than that of the majority of the bedrock, which itself typically exhibits minor alteration. Where inferred fracture zones intersect boreholes, they define high fracture frequency intervals (HFFI), which exhibit the same characteristics of increased fracture and alteration intensities. In some locations, notably in IG_BH02, the HFFIs are spatially coincident with steeply to moderately inclined, and northeast-dipping, aphanitic and feldspar-phyric tonalite dykes. The upper portion of the bedrock (~100 m) tends to have a slightly increased frequency of fractures and the highest presence of moderately altered rock.

The Paleoproterozoic diabase dykes of the Wabigoon swarm intrude the bedrock at the site-scale as a relatively late geological feature. Detailed examination of one 18 m wide Wabigoon dyke at the site suggests that, unlike the inferred fracture zones, any increase in fracture intensity or alteration is limited to a m-scale zone immediately adjacent to the dyke margins.

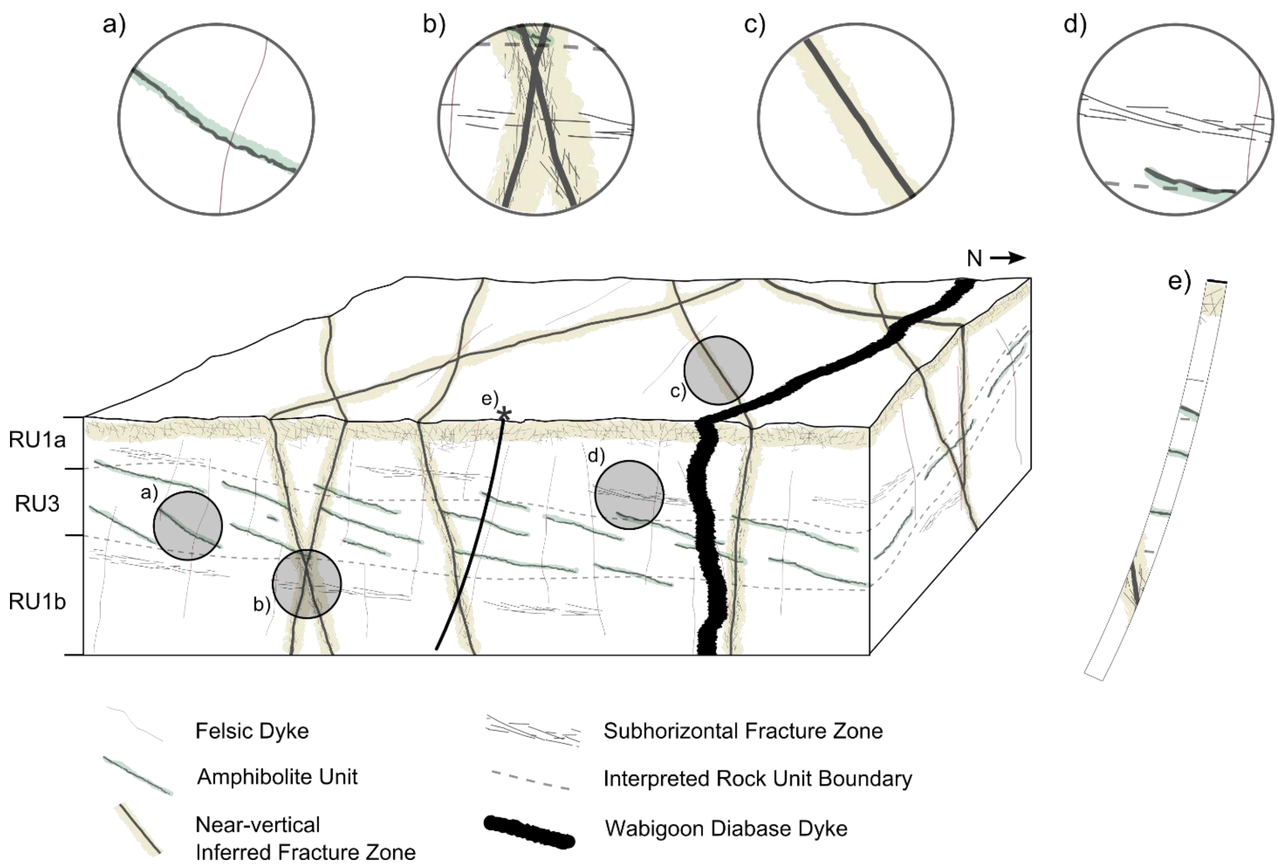

Figure 37. Current conceptual understanding of site-scale bedrock geology based on integrated geological and geophysical data from surface and initial three boreholes. The main rock type is biotite granodiorite-tonalite and is intruded by various suites of high-angle felsic dykes, and moderately dipping amphibolites. Bedrock can be subdivided into rock unit domains based on intervals identified in single borehole integration reports. Rock unit subdivisions are largely based on presence, or a relative absence, of (a) gently inclined and north-dipping amphibolite occurrences throughout the bedrock. Relatively pervasive alteration is present along the shallow fractured subsurface (upper ~100 m) and is hypothesized to collocate along the ((b) and (c)) near vertical fracture zones associated with interpreted lineaments. Subhorizontal fracture zones (d) tend to be identified in borehole logs at various depths. e) presents a hypothetical borehole log through

the conceptualized model. The borehole shows the shallow fracture zone near the ground surface with weak alteration, intersection of amphibolite units, and a near vertical fracture zone with alteration.

5. Geological Model

5.1 General Principles and Overview

Three-dimensional geological modelling in this study involves integration of geological and geophysical data types, including direct data (e.g., data based on direct observation and measurement) and indirect data (e.g., information based on inferences and interpretations based on expert judgement). These input data can be used to construct, edit and visualize the geological data as different objects (e.g. points, lines, surfaces, volumes, wells). Geological models are typically developed to represent the distribution of surface and subsurface geology and the associated physical rock properties, which can vary from simplistic geometries to complex patterns. Because geological model information is based on glimpses of the subsurface from borehole data, currently without the use of geophysical imaging (e.g. seismic), it is important to iterate the model development as additional information is obtained. Eventually, as additional data is acquired and used in the model, remaining uncertainties will be minimized. Continually updated models will ultimately inform other geoscientific disciplines and will form the framework used in the design of an underground repository and the assessment of long-term safety of the site.

5.1.1 Model Extent

The 3D geological model is constructed using the geological modelling software GOCAD-SKUA v19 coupled with the MIRA Mining suite module. The site-scale model is 5000 m by 5000 m covering an area of 25 km^2 (Figure 38a). The targeted vertical extent includes 1500 m of bedrock between the mean topographic elevation of 419.6 masl and -1080.4 masl. As such, the model was constructed with a vertical extent of 1600 m from 500 masl to -1100 masl (Figure 38b), which provides a sufficient buffer beyond what is needed for other numerical assessments. Easting of 553,500 m and Northing of 5,483,000 m describes the southwestern coordinate of the model extent (NAD83, UTM zone 15N).

The majority of the acquired geological data used to build the model are in the central part of the model extent, including drilled boreholes and related in-hole testing. The boreholes were drilled to approximately 1000 m along the planned trajectory. In order to interpolate physical rock properties and develop a geological block model, the model extent was discretized into a regular grid with 1,642,361 cells each with 50 x 50 x 10 m dimensions. Grid cell sizes can be modified during future model updates.

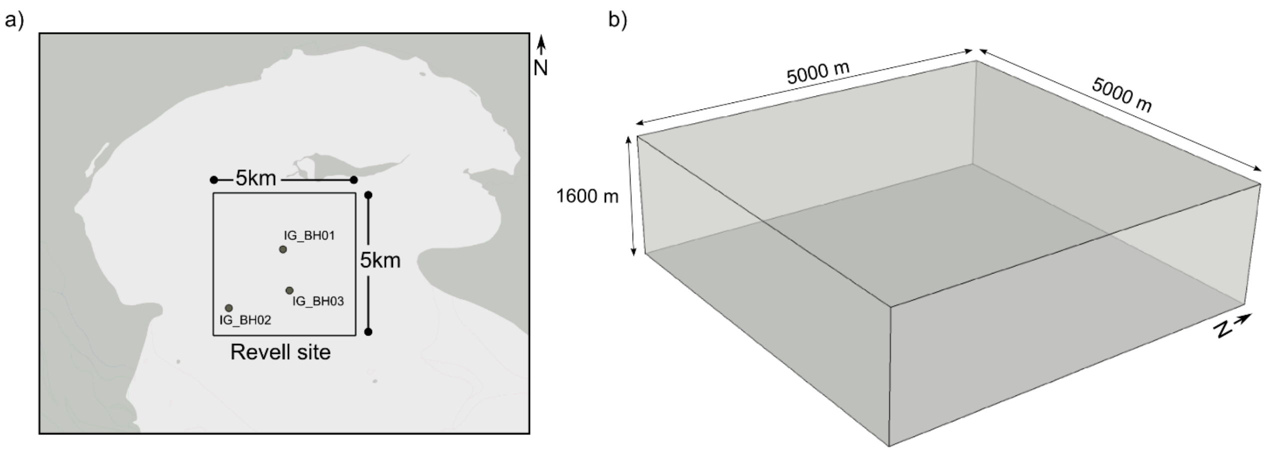

Figure 38. Extent of the site-scale model. a) model outline on simplified bedrock geology. Pale grey shows the Revell batholith and dark grey shows the surrounding greenstone belt; b) model boundaries in 3D oblique view.

5.2 Geological Modelling Approach

The following bullets summarized in Figure 39 describe the generalized approach to geological modelling used to develop the initial site-scale model for the Revell site area. Methodologies for the integrated rock unit, integrated structural unit and deterministic fracture zone modelling are described in more detail in Sections 5.3, 5.4, and 5.5, respectively.

a) *Data review, compilation, and data pre-processing* - review and compilation of geological and geophysical data, as described above in Sections 3 and 4. Data includes recorded surface and borehole rock types and fracture characteristics from surface bedrock mapping; airborne magnetic, airborne gravity and derived inversion results; LiDAR and derived DEM results, and orthoimagery. Data pre-processing involves appropriate reformatting of data currently residing on the NWMO Geoscientific Database (e.g. DAP and AcQuire). Formatting involves manipulating the data structure to an appropriate format for GOCAD importer functions. To ensure spatial consistency, data first had to be similarly georeferenced. For the Revell site, NAD83 UTM15N is the local coordinate system. Much of the data exists as points, curves and surfaces, and 2D rasterized grids.

b) *Surface- and voxel-based modelling* - surface-based modelling involves the construction of surfaces to represent topography, fracture zones and rock unit domain boundaries. Surfaces can be interpolated from input data such as points from boreholes or field mapping, or curve traces such as interpreted lineaments or boundaries. Surfaces can be used to subdivide a model into voxel regions. Voxel-based modelling involves the rasterization of the surface-based model into a 3D grid that can be further parameterized as categorical or numerical properties.

c) *Model integration* – compilation of the surface- and voxel-based models produces a unified model including the rock unit and structural unit domains, and inferred fracture zones that can be used in additional evaluations (e.g. repository design, hydrogeological modelling, etc.).

d) *Model review and verification* – visualizing model results as horizontal and vertical cross-sections, grid-value isosurfaces, geobodies and regions, etc. These model visualizations are evaluated to ensure that input data, surface topology and geometry are honoured. The model is also evaluated against our geological conceptualization of the subsurface and is reviewed by other internal subject matter experts.

A last step of the modelling procedure and reporting is to summarize the model uncertainty. Model uncertainty can be described in terms of uncertainty in the input data (e.g. data type, data density, etc.), and/or uncertainty associated with the modelling approach (e.g. deterministic or stochastic). In this report, the assessment includes a description of uncertainty related to different levels of interpretation, data quality and modelling efforts, as well as quantifying the input data density. Other forms of model uncertainty will be evaluated in future modelling reports.

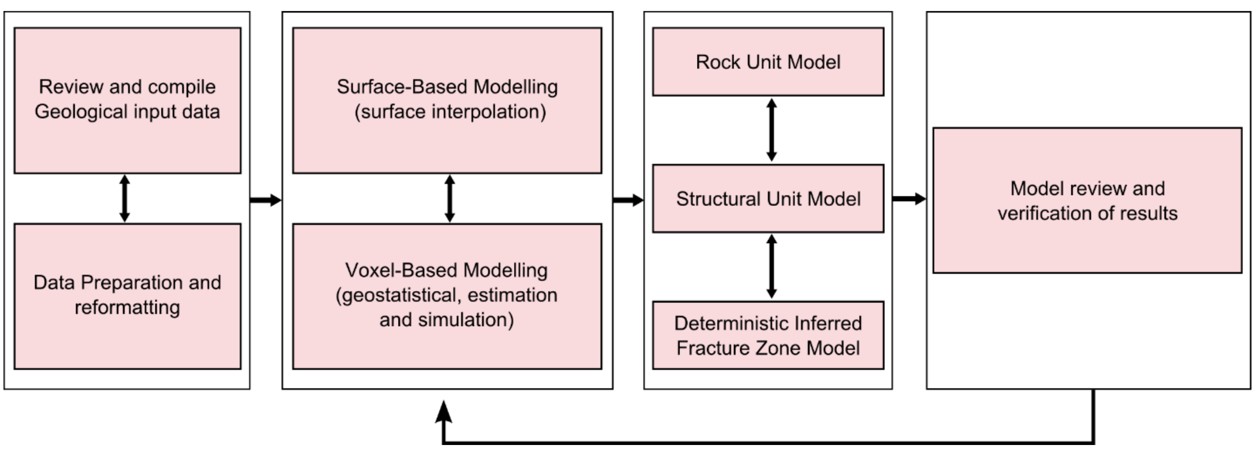

Figure 39. Modelling workflow followed to develop a site-scale geological model. a) includes the review and preparation of geoscientific data, b) input of prepared data into surface-based and voxel-based modelling approaches, c) output of integrated rock unit, integrated structural unit, and inferred fracture zone models, and d) review of each model component.

5.3 Integrated Rock Unit Modelling

In this initial version of the geological model, a 3D integrated rock unit (IRU) model is developed honouring the top and bottom locations of rock unit domains defined as part of the single borehole integration reports for IG_BH01, IG_BH02, and IG_BH03 summarized in Section 4.2.7 (see also Parmenter et al. 2021a, 2021b and 2021c). Rock unit domains are imported along the borehole path as categorical interval logs (e.g. from and to depths) with categorical labels

IRU1a, IRU1b, IRU2 and IRU3, previously discussed in Section 4.2.7. Interval boundaries are defined by borehole markers denoting the tops and bottoms of each integrated rock unit.

Several assumptions are made with regards to developing this initial integrated rock unit domain model. Rock unit (RU) domains were defined for each borehole primarily based on the dominant rock type and the degree of accessory rock types encountered in the interval. As described under the conceptual model understanding (Section 4.3), the rock unit boundaries are largely based on clustering of amphibolite occurrences along the length of the boreholes. As a result, the locations of these rock unit boundaries are fairly subjective. Despite this uncertainty, these rock unit subdivisions adequately parse the boreholes into domains that capture the general changes in the rock types that may be important in characterizing the geosphere. For each of the three boreholes, it is assumed that rock unit boundaries are correctly interpreted based on the available geoscientific information (Parmenter et al. 2021a, 2021b and 2021c).

It is also assumed that the rock unit domain boundaries extend laterally between the three boreholes, do not intersect with the topographic surface and are not offset by faults. However, this assumption may change as more information is collected. Due to the presence of overburden and water features covering much of the site, distinguishing rock unit boundaries on the ground surface has not yet been attempted. For this iteration, the rock type mapped at the topographic surface in the model is correlated with the main biotite granodiorite-tonalite unit identified in surface mapping and in the shallow portion of all boreholes. Ongoing field mapping may assist with connecting subsurface rock unit domains to the topographic surface for future model iterations.

In this report, we implement explicit modelling which involves directly building geological surfaces by interpolating between sets of points, or sets of curves. Using this approach, domain boundaries are built independent of each other and, as needed, surfaces are manually truncated along intersections. Interpolation can result in angular and blocky surfaces, so this is followed by surface smoothing using the SKUA-GOCAD discrete smoothing interpolator (DSI) function. This function minimizes the surface roughness, while maintaining the spatial accuracy of the surface passing through the location of available data. Once a surface is constructed using the available data, surfaces can easily be updated as new data becomes available by locally stretching and warping the surface towards the new data points. Once the surface is fitted to the appropriate points, the nodes at each point can be locked so they remain fitted during any future modifications. The generalized surface-based modelling workflow is presented in Figure 40 honouring the spatial position of rock unit domain boundaries in the boreholes, the borehole path, and the topographic ground surface. The surfaces derived by interpolation are used to segregate a voxel model and assign categorical properties based on the rock unit domains.

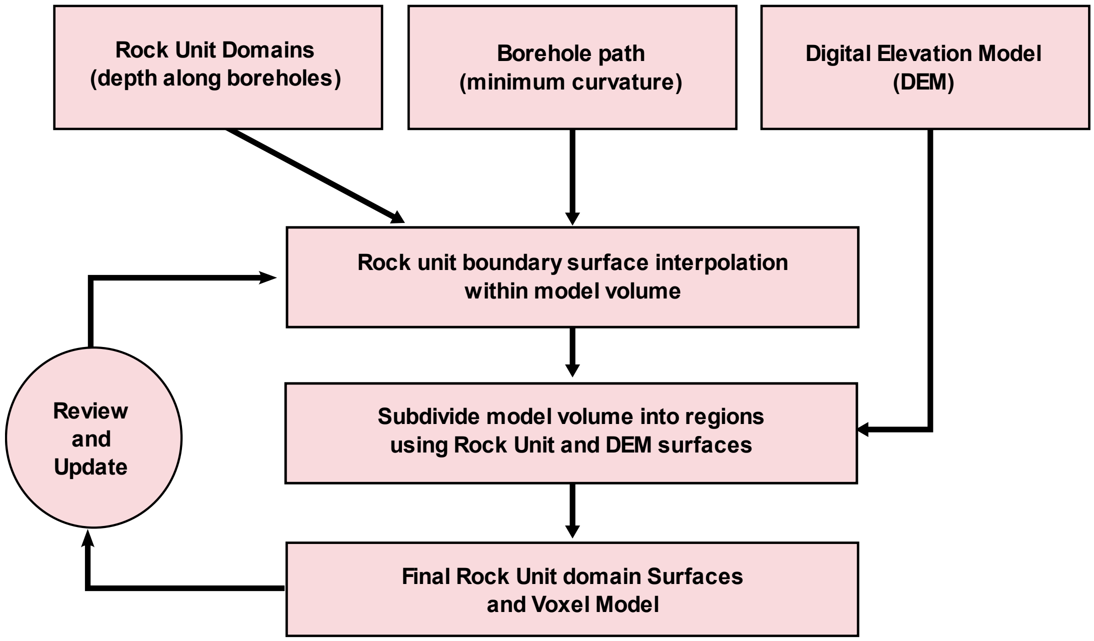

Figure 40. Surface-based modelling workflow used to interpolate rock unit domain boundaries between boreholes to develop the Integrated Rock Unit (IRU) model.

Based on the results of the single borehole integration reports, the model volume is subdivided into three unique rock units (previously summarized in Section 4.2.7). The units IRU1a and IRU1b show consistent characteristics between each of the boreholes: the dominant bedrock is biotite granodiorite-tonalite, and the occurrences and proportions of subordinate accessory rock types are narrow, mostly felsic dykes. Rock unit IRU2 has only been interpreted from 180.01 m to 242.50 m depth in IG_BH01 and consists of predominantly biotite tonalite with two cm-scale, coarse-grained pegmatite dykes and two cm-scale, medium-grained biotite granodiorite-tonalite dykes. The upper boundary of this unit appears gradational in core, but the lower boundary appears sharp and dips steeply towards the southeast (72° towards 136°). This contact information can be assigned to the upper and lower boundaries and the domain surfaces can be extrapolated away from the borehole. Due to the lack of spatial constraints in other boreholes and the similar composition of the biotite tonalite and the biotite granodiorite-tonalite, IRU2 has been modelled together with the IRU1a and IRU1b units. This unique rock unit can be evaluated further as additional borehole are drilled in the area.

Rock unit IRU3 comprises very similar characteristics to the previous rock units. However, it includes an increased presence throughout of narrow amphibolites on sub-metre to metre scale. Based on geological and geophysical core logging, this rock unit is still predominantly biotite granodiorite-tonalite with subordinate felsic dykes, but approximately 5 percent of the unit is amphibolite. This is the main factor differentiating IRU3 from the other IRU’s.

As shown in Figure 41, the initial surfaces representing rock unit domain boundaries are interpolated using borehole markers as constraints. Markers are positioned along the borehole depth based on an integrated interpretation process documented in the single borehole integration reports. Because each surface is only constrained by 3 points, the surfaces are perfectly fitted to the data with zero curvature along the surface. As more data is used in future iterations of the rock unit boundaries, these surfaces are expected to curve and form smoothed planes that fit through all the data points.

In general, the top and bottom surfaces of IRU3 are shallowly dipping (~10°) towards the north. Overall, surface geometry is somewhat consistent with the dominant orientation of the amphibolite contacts that are located within IRU3, which are moderately to gently dipping towards the north (Section 4.2.3). In addition, the orientation of the rock unit boundaries shares a similar dip geometry and magnitude as the subhorizontal fracture set defined in all three boreholes, and the overall shallowly-dipping structural grain identified in the borehole data set. Overall, subdividing the model into discrete integrated rock unit domains is straightforward based on the integration of data from three boreholes. However, as rock unit domains are interpreted in future boreholes, the current distribution of the integrated rock unit boundaries may include additional, potentially complex geometries. Despite the possibility of increased apparent complexity, we expect to decrease the degree of uncertainty as more boreholes are drilled and more spatial information is acquired.

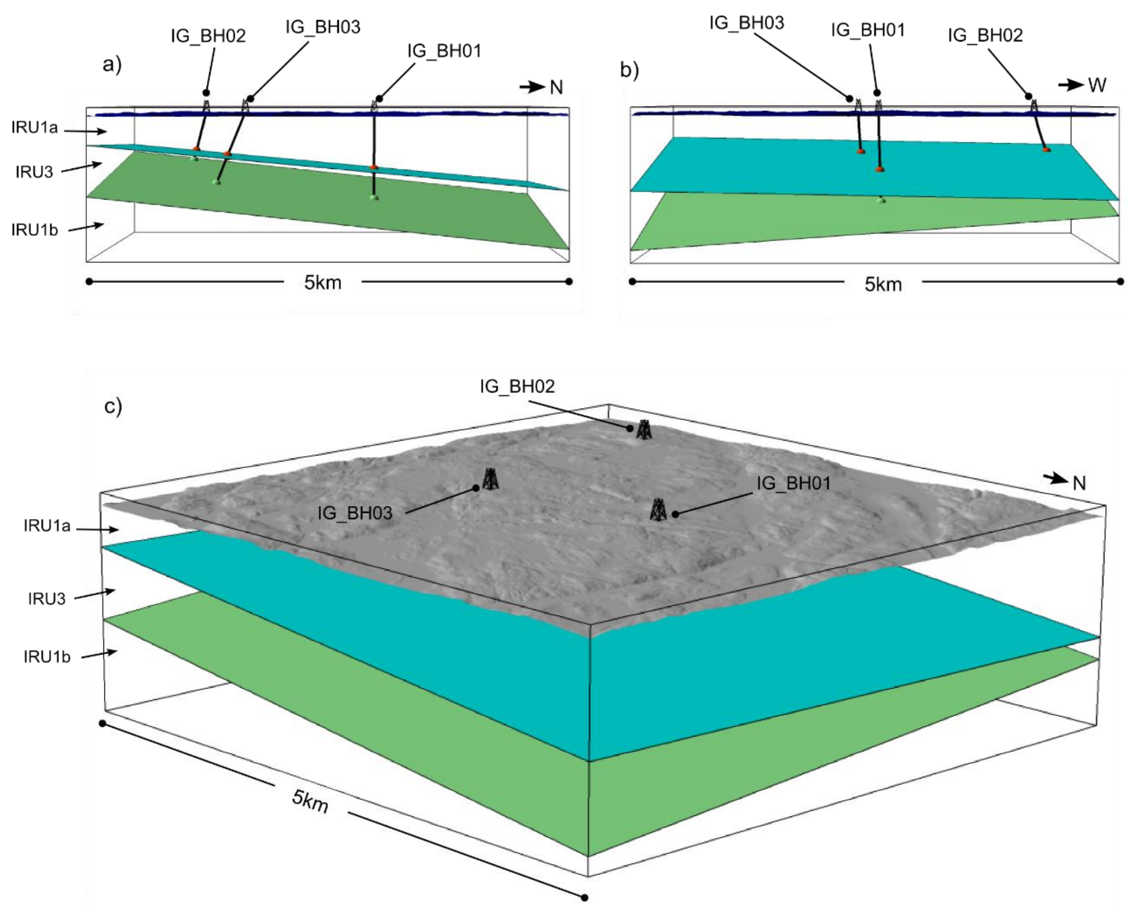

Figure 41. Surface based representation of geological domain boundaries subdividing the integrated rock units and crossing through borehole markers. Borehole markers are defined based on the rock units identified in the single borehole integration reports.

Using the geological domain boundaries, the thickness of each IRU domain are calculated. Figure 42 shows the vertical thickness of each modelled rock unit. Figure 42a presents the thickness of IRU1a from the ground surface to the top of IRU3. The IRU1a unit thickens towards the north, extending to greater than 800 m thick with much of the variability in thickness due to local scale topographic relief. Figure 42b presents the thickness of IRU3 which gradually thickens towards the east from approximately 100 m thick in the southwest corner of the model to greater than 600 m thick in the northeast corner. Figure 42c shows the thickness of IRU1b, which increases from approximately 300 m thick in the northeast corner of the model to just over 1000 m thick in the southwestern corner of the model. The minimum, maximum and mean thicknesses of each of the integrated rock units is summarized in Table 7.

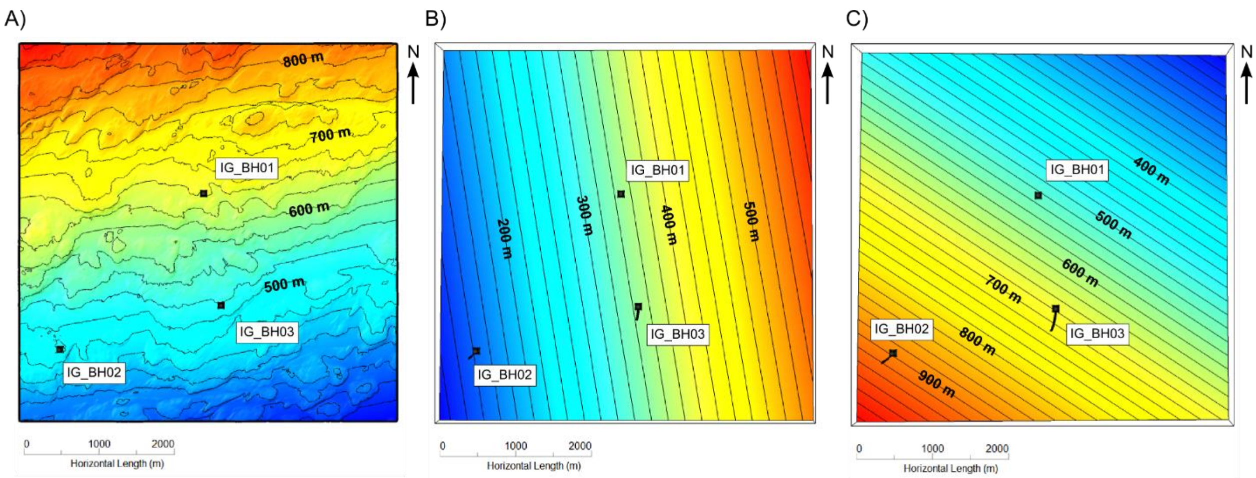

Figure 42. Vertical thickness of the integrated rock units. A) IRU1a, B) IRU3, and C) IRU1b. IRU3 represents the biotite granodiorite-tonalite with the inclusion of approximately 5 percent amphibolite.

Table 7. Summary statistics for integrated rock unit thicknesses derived from the model.

Thickness	IRU1a	IRU3	IRU1b
Minimum (m)	300.83	86.84	131.16
Maximum (m)	880.05	606.67	1028.37
Mean (m)	590.47	346.75	579.76

Using the integrated rock unit boundary surfaces presented in Figure 42, a voxel model with 50 x 50 x 10 m cell dimensions is parameterized with the categorical integrated rock unit identifier (e.g. IRU1a, IRU1b and IRU3). Figure 43 shows an oblique view towards the northwest of the voxel model presenting the spatial distribution of the integrated rock unit domains. The top surface of the voxel model represents the coarse surface topography based on intersecting the voxel cells with the topographic DEM surface.

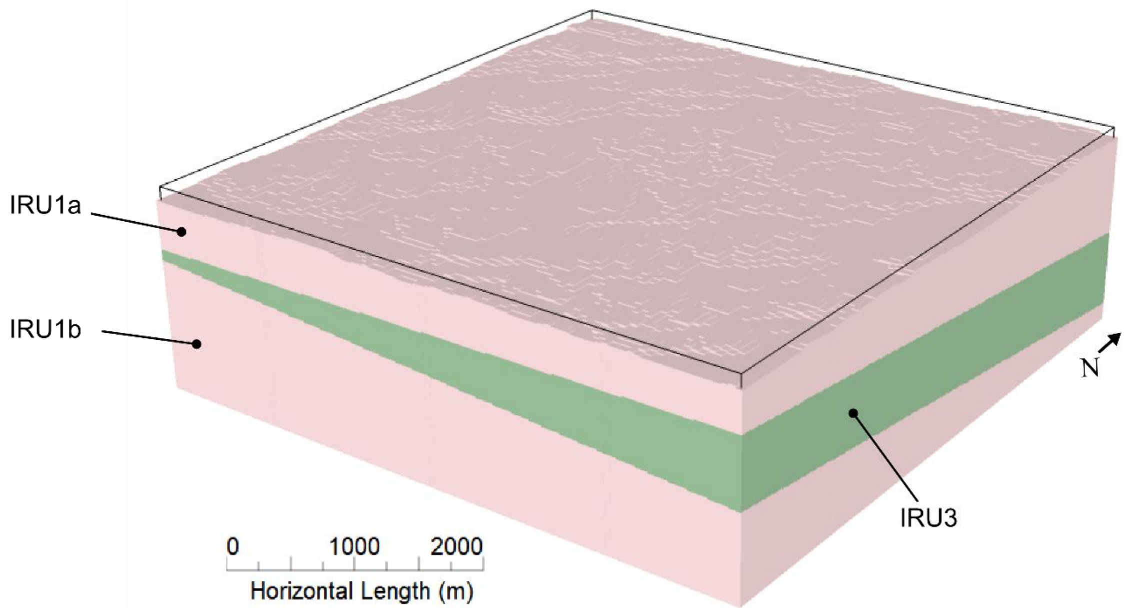

Figure 43. Voxel representation of the integrated rock unit model. IRU1a and IRU1b present predominantly biotite granodiorite-tonalite with subordinate narrow felsic dykes, and IRU3 represents a similar biotite granodiorite-tonalite with felsic dykes and the addition of approximately 5% amphibolite.

Even though a 3D integrated rock unit model has been developed, there remains a degree of uncertainty in the spatial distributions of these IRU volumes due to a lack of available input data. As additional field investigation data sets are acquired, they will iteratively support the update to our 3D understanding of the site bedrock geology. Future borehole data will be used to verify the accuracy of the model by comparing spatial model predictions to the drilling results.

5.4 Integrated Structural Unit Modelling

In this report, the integrated structural unit (ISU) model is developed through geostatistical modelling of the location and proportions of structural units defined as part of the integration and synthesis of each individual borehole (Parmenter et al. 2021a, 2021b and 2021c). Instead of applying a surface-based modelling approach here, geostatistical voxel-based modelling was implemented using indicator kriging estimation and simulation methods (e.g. Journel, 1983; Journel and Alabert, 1988; Gomez-Hernandez and Srivastava 1990; Pyrcz and Deutsch, 2014). In this case, the indicators represent the unique integrated structural units.

Several assumptions are made with regards to developing the early version of the integrated structural unit domain model. Structural units (SU) have been defined to capture the general variation in fracture frequency along the length of each individual borehole with their boundaries based on broad changes in slope visible in the cumulative fracture frequency curve. Each structural unit is then grouped into a categorical bin (high, moderate, low) based on the quantile range. As with the rock units defined previously, the criteria for defining the structural units and their categorical value may be modified once additional fracture data is collected in future boreholes. The model presented here represents an interpretation based on general broad trends in the available data and is therefore assumed to adequately subdivide the borehole into domains that capture the spatial complexity of the subsurface. For the purpose of this initial model, it is assumed that the integrated structural unit boundaries correctly reflect the structural unit domains defined on the basis of the available geological information (Parmenter et al. 2021a, 2021b and 2021c). This assumption can be updated as additional data is incorporated into the model.

Given the amount of available borehole data, it is also assumed that the voxel-based modelling approach is adequate to capture the complex structural unit geometries between the boreholes. This approach assumes stationarity of properties across the site and that the spatial variogram applied can be adequately modelled. In addition, it is also assumed that lateral continuity can be applied to the site to accurately interpolate the structural unit domains between boreholes. Each of these assumptions shall be evaluated in future model iterations and may be updated based on new findings from additional field investigations.

Structural unit modelling follows an approach presented in Figure 44. The structural unit domains embedded along the borehole as categorical interval logs (e.g., from and to depths) are used as input data. Based on the characteristics of these domains, they have been subdivided into classes of low, medium, and high fracture intensity relative to each other (previously discussed in Section 4.2.7). For use in voxel modelling, the structural unit categories are extracted along a defined interval along the borehole that is appropriate for the voxel grid cells (e.g. Figure 45). As such, categorical properties were composited from the top to bottom of the well at a fixed interval of 5 meters where the category that spans the majority of the interval length is assigned. The composited categorical log is then converted to a set of points with their ISU properties assigned. At this point, the categorical properties are ready to be used in variogram, estimation and simulation analyses.

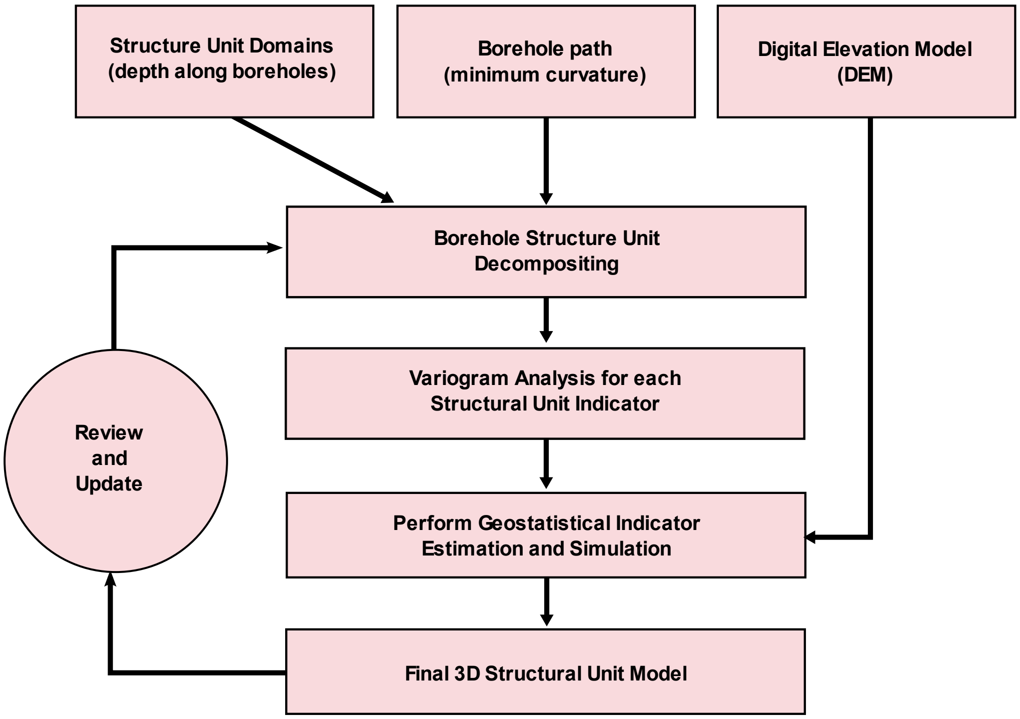

Figure 44. Voxel-based modelling workflow used to interpolate structural unit domains in the model extent and develop the Integrated Structural Unit (ISU) model.

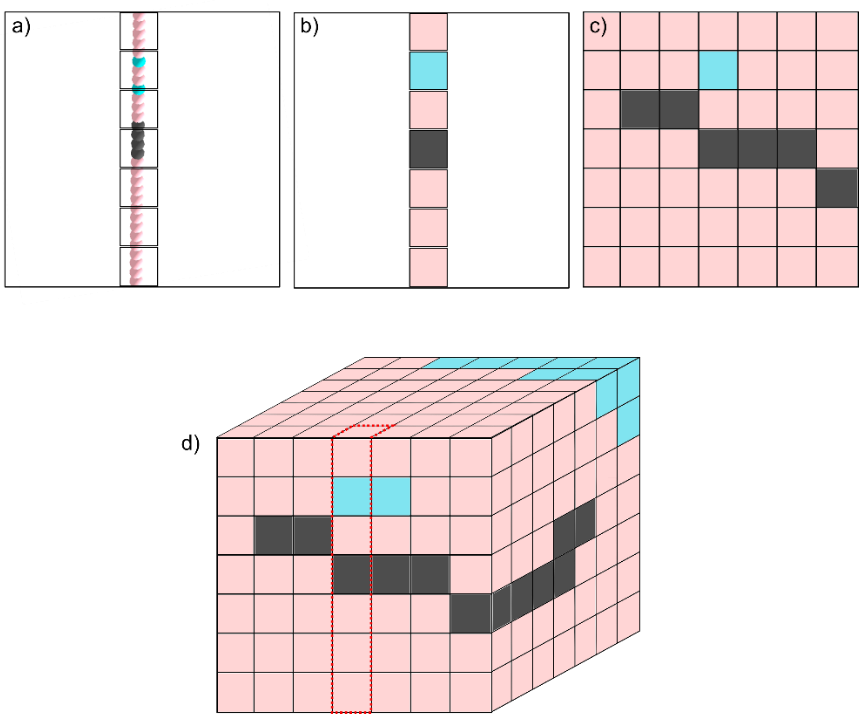

Figure 45. Schematic diagram of data representation as (a) indicator values along decomposited borehole as points, (b) upscaled indicator values to grid cells based on most probable, (c) indicator interpolated on a 2D view, and (d) indicator interpolated on a 3D grid view

5.4.1 Indicator Variography

Data from the structural units of only three boreholes is considered to be too sparsely distributed to model the spatial variability (i.e., variogram analysis) and therefore variogram assumptions are required. Pyrcz and Deutsch (2014) indicate that one of the difficulties of variogram interpretation is a lack of data to calculate the spatial variability between sample locations. It is likely that the true nature of the bedrock exhibits a spatial connection of the structural units, but the lack of data available in the subsurface currently masks the interpretation. Despite this limitation, we attempt to model an experimental variogram to each indicator type in the structural unit data set. There is a significant uncertainty at this stage. It is expected that as we collect more data from additional boreholes the variogram model will become increasingly reliable.

Variogram analysis for indicator values requires each of the indicators to be evaluated separately. As a result, the data used in each variogram consists of binary values of 1s and 0s, marking the presence or absence of the indicator (e.g. Pyrcz and Deutsch 2014). The expected transitions between the variogram results for each indicator should be smooth in terms of their modelled range and variance. The experimental vertical variogram (Rv) for the structural units was fitted with an exponential model for each of the indicators separately. However, due to the sparsity of data, a horizontal model was not fitted, and an alternative omni-directional horizontal model was approximated based on the geometry of the rock unit model and the shallowly dipping structural grain of both ductile and brittle structures. The proposed horizontal model assumed a horizontal to vertical ratio of 10:1 with the dip and azimuth set to 10 degrees towards the north, respectively. The azimuth and dip of the variogram model is consistent with that of the general orientation of the integrated rock unit boundaries observed in boreholes. Table 8 presents the final variogram model used for the structural unit model.

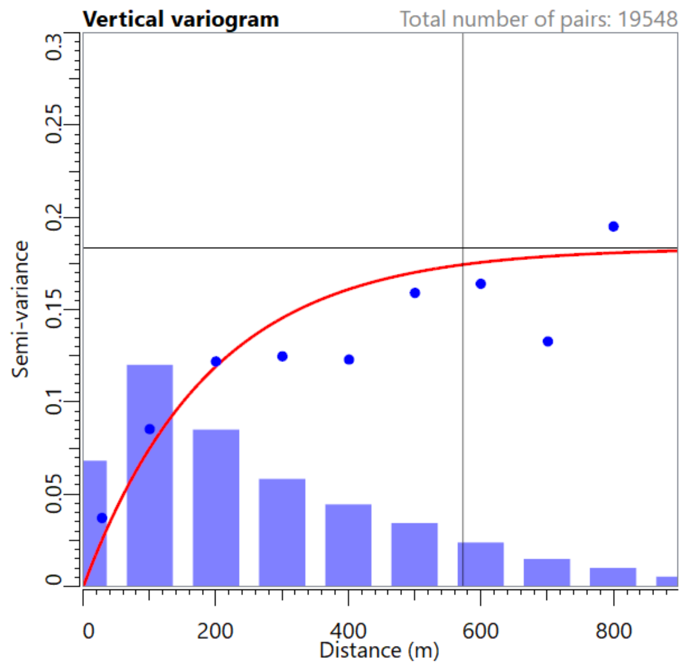

Figure 46. Vertical semi-variogram model fitted to the composited borehole log for the High structural unit indicator.

Table 8. Vertical and horizontal variogram model parameters

Indicator	R_v Vertical	Contribution	H:V ratio	R_h Omni-directional
High	575	0.18	10:1	5750
Med	615	0.32	10:1	6150
Low	495	0.16	10:1	4950

5.4.2 Estimation

Kriging provides a means to estimate modelled geologic trends between data points, where spatial variability is specified by variograms. Indicator kriging (IK) is a spatial interpolation technique devised for estimating a conditional cumulative distribution function at an unsampled location. Therefore, this approach can be used to estimate trends in categorical data between data points, where spatial variability is specified by variograms. Indicator kriging of categorical data has been completed as part of this study to evaluate spatial trends in available borehole and surface data for the structural unit domains.

Indicator kriging was performed in SKUA-GOCAD using a voxel grid with cell dimensions 50 m x 50 m x 10 m. The structural unit indicators along the borehole were first composited along 10 m interval lengths along the borehole path to align with the voxel grid dimensions. Borehole compositing occurred from the top of the borehole to the bottom where the value assigned to each point was based on the majority indicator in the corresponding 10 m interval. The model was conditioned using the defined proportions of each structural unit indicator from the three boreholes (Section 4.2.7). Indicator Kriging was performed using the Ordinary Kriging method and search parameters were defined to use all data points in order to produce a smooth result and minimize the mean squared error.

Overall, the spatial estimation of the integrated structural units based on indicator kriging shows a preferred geometry that is shallowly dipping towards the north (Figure 47). The geometry and spatial correlation are defined from input assumptions provided in the variogram model. The overall shallow dip towards the north is based on an interpretation of the surface geometry bounding the rock unit model and the presence of north-dipping shallow-dipping fracture zones identified throughout all three boreholes (Section 4.3). As expected, the estimated indicator domains honour the borehole data along their intersection locations. The main difference is that the shapes of the simulated structural unit domains are irregular.

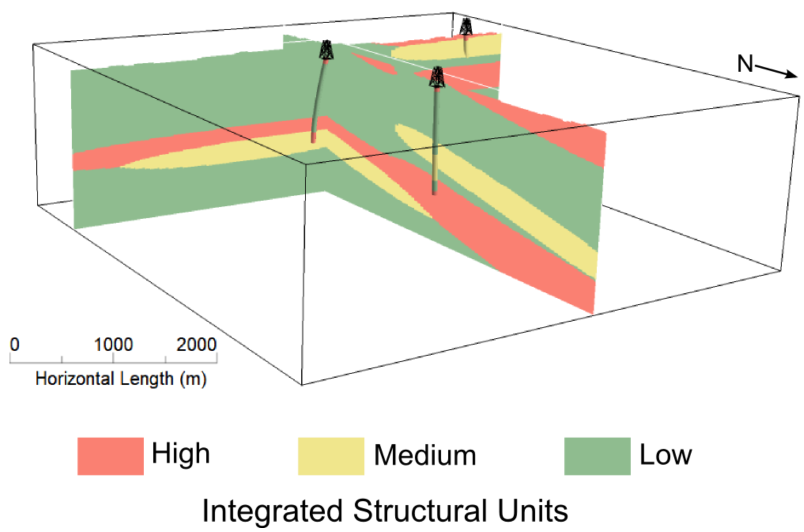

Figure 47. Integrated structural unit (ISU) model showing High, Medium, and Low domains. Bins of High, Medium, and Low represent fracture intensity domains based on mean fracture counts. Domains were estimated by ordinary Indicator Kriging (IK), honouring composited borehole structural units at 10 m intervals, and the variogram model. Due to a sparse distribution of boreholes, the horizontal variogram was approximated to allow the integrated structural unit boundaries to be smooth and laterally continuous across the entire model extent (with a 10:1 horizontal to vertical ratio used to assign the horizontal range).

5.4.3 Simulation

In addition to indicator kriging, stochastic simulation of the structural units was also conducted in order to capture spatial heterogeneity and to assess uncertainty. Geostatistical simulations add randomness to the sequence of indicator kriging by visiting grid nodes sequentially in a random path. At each random grid node visited, the simulator searches for nearby input data or previously simulated data and derives the new indicator value for the given spatial location. As a result, simulation algorithms typically do not possess the smoothness of kriging but allows the generation of multiple equiprobable realizations to account for uncertainty in the subsurface. The use of multiple realizations can be compiled to assess spatial uncertainty metrics, such as entropy, cardinality, diversity and probability for each indicator value. As more data is used to condition the model, these uncertainty metrics can provide a means to quantify the degree of uncertainty that remains within the subsurface.

Running the sequential indicator simulation (SIS) in SKUA-GOCAD followed many of the same input parameters as indicator kriging. SIS was performed in SKUA-GOCAD using a voxel grid with cell dimensions 50m x 50m x 10m. The structural unit indicators along the borehole were first composited along 10 m interval lengths along the well path to align with the voxel grid dimensions. Borehole compositing occurred from the top of the borehole to the bottom where the value assigned to the point was based on the majority indicator in the 10 m interval. Similarly, the model was conditioned using the define proportions of each structural unit indicator from the three boreholes (Section 4.2.7). A variogram was defined based on information provided in Section 5.4.1. SIS was performed using Ordinary Kriging method and search parameters were defined to use a large number of data points (60) in order to produce a smooth result and minimize the mean squared error. A higher the number of data points selected will result in a longer simulation time. The number of realizations defined is 25 with a random seed of 101.

The indicator simulation involved generating 25 realizations of the integrated structural unit model. Each realization spatially honours the borehole structural unit values and the variogram model. Based on the collection of realizations the most probable indicator and indicator probability are calculated at each grid cell. The most probable indicator represents the structural unit value that has the highest probability of occurring in a given cell. The results from the indicator simulation produced an irregular body for each of the integrated structural unit domains. Overall, the integrated structural units have a preferred geometry that is shallowly dipping towards the north based on input assumptions provided in the variogram model. Where the simulated domains intersect the boreholes the spatial positions of the domains are correlated to the indicator. Results from all 25 realizations are combined to determine the expected integrated structural unit distributions based on the highest probable indicator in each cell. Figure 48 presents three of the modelled realizations (Figure 48a to c) and shows the spatial probability of each of the structural unit values (Figure 48d to f). Figure 49 presents the expected structural unit distributions based on the highest probable indicator in each cell from the ensemble of realizations. Overall, the results produced are similar to those of the estimated distribution from indicator kriging. The main difference is that the shapes of the simulated structural unit domains are irregular, and there is substantial heterogeneity at the base on the model volume despite there being no borehole control.

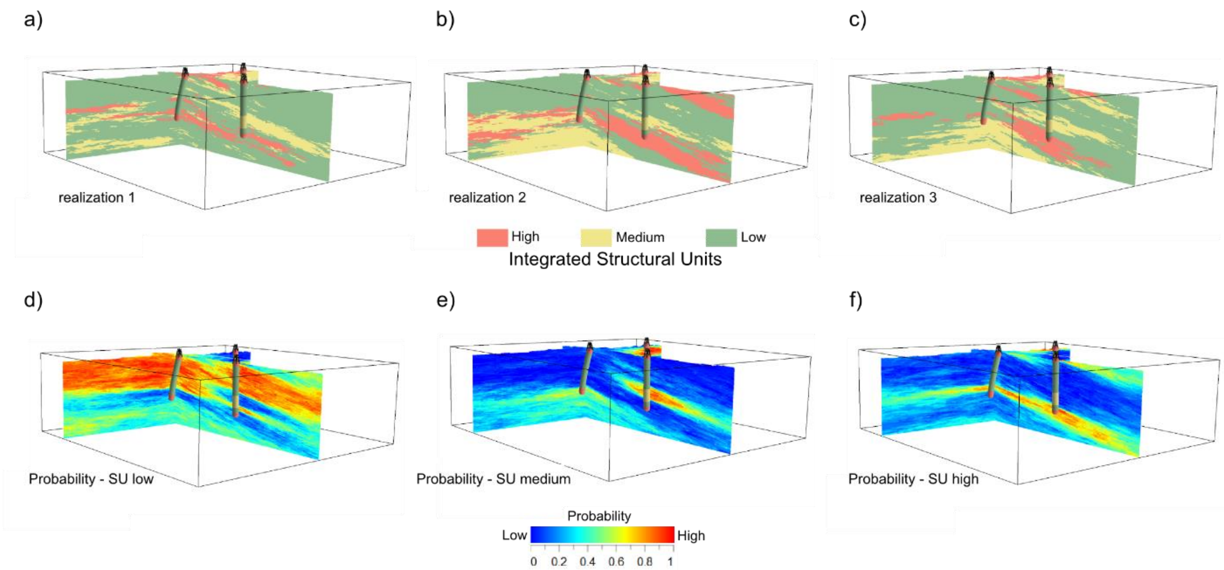

Figure 48. Three example realizations of the integrated structural unit model showing High, Medium, and Low domains shown in a), b) and c). A total of 25 realizations were simulated. Using all realizations d), e) and f) show the probability distributions for the Low, Medium and High indicator for each model cell.

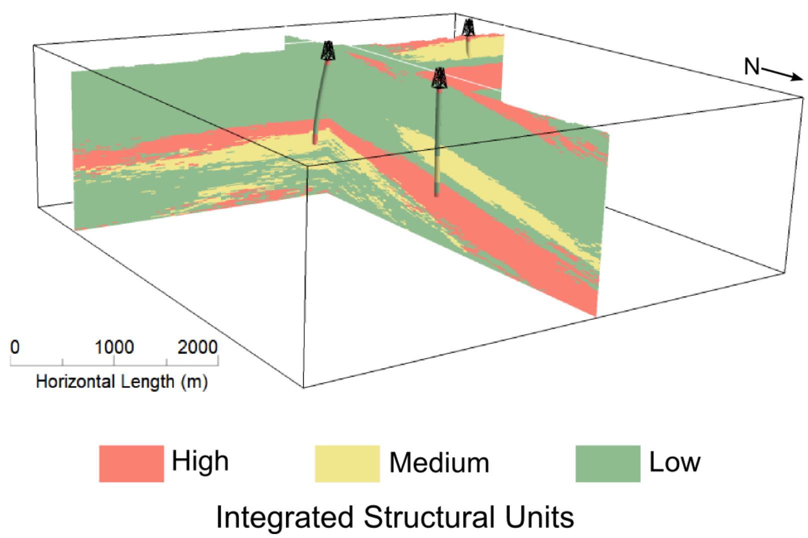

Figure 49. Integrated structural unit model showing High, Medium, and Low domains. Domains were simulated using the sequential Indicator simulation (SIS) with ordinary Kriging (IK) algorithm, honouring composited borehole structural units at 10 m intervals, and a vertical variogram model. Due to a sparse distribution of boreholes, the horizontal variogram was approximated to allow integrated structural unit boundaries to be smooth and laterally continuous across the entire model extent (with a 10:1 horizontal to vertical ratio used to assign the horizontal range). SIS results provide multiple probable realizations (n=25) and allow the model to incorporate some degree of spatial heterogeneity in the distribution of units.

Inspection of the indicator proportions from the three boreholes, indicator kriging and indicator simulation are presented in Figure 50. Based on the results, the proportions derived from estimation and simulation approaches both approximate well the proportions recorded in the composited 10 m intervals of the borehole structural unit indicator logs. Despite the similarities, both the estimation and simulation results slightly overestimate the proportion of the low indicator by 4 to 5%, and slightly underestimate the proportion of high indicator by 5 to 6%. A possible reason for this discrepancy is the use of the upscaling approach to map the borehole structural unit proportions to individual grid cells.

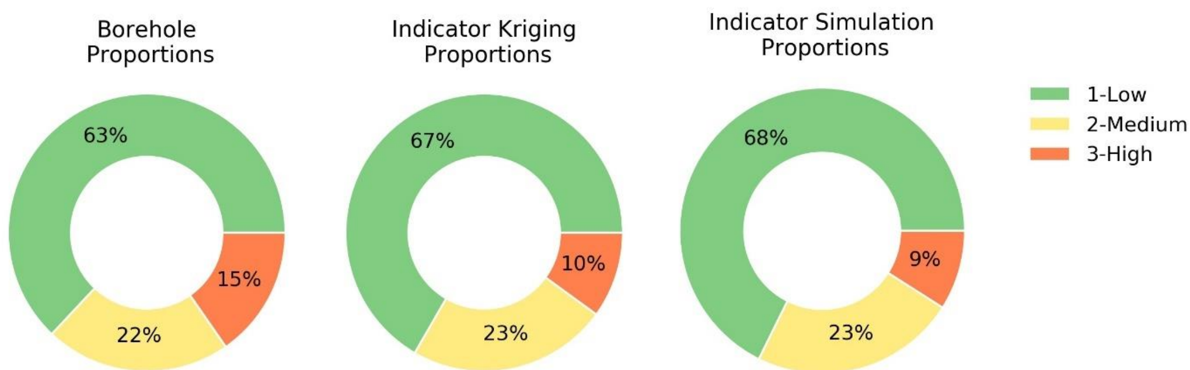

Figure 50. Relative structural unit proportions presented in the composited borehole log, and as a result of indicator estimation and simulations. Estimation and simulation results perform well at simulating the relative proportions of each structural unit in the model.

Both the indicator estimation (Figure 47) and simulation (Figure 49) produce a discontinuous high fracture intensity domain in the shallow subsurface of the integrated structural unit model. This result is a function of the sparse distribution of borehole data used to constrain the model and the spatial correlation assumptions used to define the variogram. However, the shallow bedrock domain over the entire site-scale model is expected to have an increased fracture intensity zone that is continuous in the shallow bedrock to a depth of 50 to 100 m below ground surface. An increased fracture intensity near ground surface is consistent with results from our first three boreholes and is consistent with conceptual fractured bedrock model developed at the Lac Du Bonnet underground research laboratory (Everitt et al., 1996). As a result, a surface is interpolated across the entire upper portion of the site-scale model representing the base of the near-surface high intensity structural unit. This surface is defined as a smoothed version of the topographic surface with a mean depth of 53.5 m below ground surface. The depth is chosen based on the mean depth to the bottom of the high fracture intensity structural unit in the three boreholes. The final estimation and simulation results are presented in Figure 51 with the continuous shallow fracture zone interpreted to extend across the entire model domain.

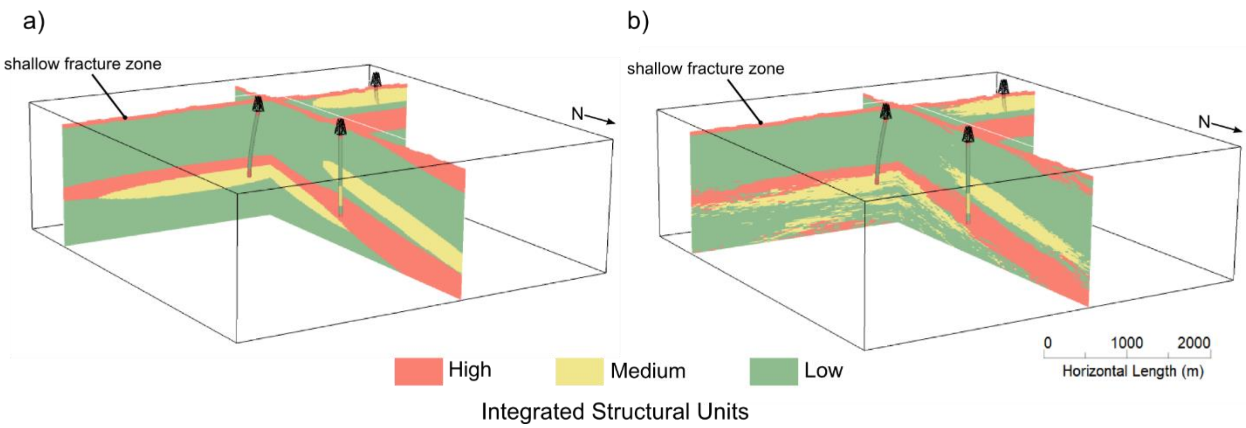

Figure 51. Compilation of the integrated structural unit models showing High, Medium, and Low domains. Estimation (a) and simulation (b) results are overprinted with an interpreted continuous shallow fracture zone based on a mean thickness of 53.5 m over the entire site-scale model domain.

5.5 Deterministic Fracture Zone Modelling

5.5.1 Inferred Fracture Zones (IFZ) Guided by Lineament Traces

Fracture zones play an important role in controlling fluid transport in fractured crystalline bedrock environments (e.g. Evans et al 1997; Achtziger-Zupancic et al, 2016; Scibek, 2020). To understand the geological factors that are responsible for transport, it is important to understand the geometry of such fracture zones and visualize their 3-dimensional shape through geological modelling. This process allows the fracture zones to be evaluated to assess their spatial distributions, intersections, terminations, geometry, thickness, etc. In this section, we present the approach to fracture zone modelling, and the 3D geological analysis of the Revell site-scale model. During development of this initial site-scale model, we assume that all inferred fracture zones are real geological structures and that they all act as potential fluid flow pathways. However, the assumed fracture zones need to be confirmed by field data and drilling. As more data are collected, the fracture zone model will be revised by fine tuning geometries, terminations, etc.

The fracture zone model presented here is in the very early stages of development and, at this stage, little is known about the subsurface geometry, damage zone width or depth extent of any individual fracture zone. Their occurrences are inferred from the lineament interpretations, combined, in a few cases, with information from borehole drilling and field mapping. As described in Section 4.1, and in DesRoches et al (2018), lineaments were interpreted using high-resolution remote sensing data sets, such as LiDAR, airborne magnetic data and orthoimagery. However, due to the low magnetic susceptibility of the Revell batholith bedrock, the airborne magnetic data did not produce clear linear anomalies that could be associated with expected magnetization reduction along inferred fracture zones. As a result, topographic data derived from LiDAR was the primary component in the interpretation of the fracture zone traces. As to be expected, there remains uncertainty whether some of the lineament traces based on the topographic surface are true fracture zones or a consequence of glacial erosion and geomorphological processes. Only in a few cases can a high frequency of brittle structures be confidently linked to the inferred fracture zones. However, our current approach assumes all these lineaments are true brittle structures until evidence from field investigations suggests otherwise.

Fracture zone modelling throughout the site-scale model is a stepwise approach as presented in Figure 52. Initial input data used to model the fracture zones include the interpreted lineament traces described in Section 4.1, which are inferred to represent true fracture zones which extend from the ground surface into the subsurface. The initial fracture zone network is modelled following an explicit approach within the site-scale volume by deterministically assigning orientation and geometry information (e.g. dip, azimuth, depth extent) to individual traces, and fitting the surfaces to available control data such as borehole intersections. In this study we focus on lineaments within the site-scale extent that are greater than 500 m in length. It is assumed that these features represent the main brittle fracture zones within the model extent, and will be used to guide data analysis in other geoscientific disciplines and the future development of underground repository layouts.

All lineaments are imported as curves into SKUA-GOCAD with their maximum trace length recorded as a property. We allowed their physical traces to extend up to 500 m beyond the model boundary to accommodate for potential fracture zones that may have variability in their dip geometry. Lineament traces are reviewed to ensure traces do not form disconnected segments, and that the topological consistencies were properly imported from the shapefile (i.e. check abutting relationships of traces). Interpreted curves are initially linked to zero elevation horizon and are draped onto a LiDAR-derived digital elevation model (DEM). Prior to draping the curves onto the DEM, nodes of the lineament traces are densified to have a maximum node spacing of 25 m, with original trace nodes preserved to honour their location. The topographic surface is defined by the high-resolution Lidar point cloud data re-interpolated to a 10 x 10 m grid, with a vertical and spatial accuracy of 0.3 m. The imported lineament traces contain a well-constructed list of attributes for each interpreted fracture zone, documenting important geometrical details such as azimuth (strike), dip magnitude, length, etc. The workflow honours the lineament traces on ground surface and propagates them as a triangulated surface, with 25 m element sides, above and below the topographic surface. Each fracture zone surface is then cut by the topographic surface to form a connected link between the two surfaces along the intersection curve. Along this curve, the node spacing honours the nodes of the topographic surface resulting in a densified triangular mesh near the ground surface.

The subsurface propagation geometry and size of the fracture zones are defined using individual feature properties assigned to each fracture zone trace (e.g. azimuth (strike), dip magnitude, depth extent). Each of the attributes are carried from the lineament trace onto the final constructed inferred fracture zone surface. At the early stage of developing the fracture zone model, very little is known about the subsurface geometry of the fracture zones. Where no information is available for a feature, the baseline assumption is that the dip is vertical (90 degrees). In addition, since there is uncertainty at this stage regarding the downward extension of the fracture zones, we assume a depth extent equal to their interpreted trace length. Similar assumptions have been made in subsurface fault rupture modelling by Johri et al. (2014) in an effort to predict fracture intensity decay within the fracture zone associated with a 3 km long fault. Nur (1982) suggested that for lineaments of tensile stress origin it is very unlikely the depth extent of fracturing will exceed its length. However, the lineament length can be greater than the depth extent by any amount. As a result, the assumption of an equal depth to length relationship may overestimate the subsurface propagation extent into the model.

In addition, an initial assumption is that these inferred fracture zones have varying widths which may be proportional to their trace length. The correlation between fault zone width, length and displacement has been the subject of much research and several empirical relationships have been established (e.g. Walsh and Watterson, 1988; Hull, 1988; Kolyukhin and Torabi, 2012). Despite these relationships, it is unclear if their scaling rules will be transferable to the fracture zones in the Revell batholith, nor whether there is a clear length to width relationship that can be defined. As site-specific investigations continue, an effort will be made to establish an empirical relationship for the Revell batholith. Such a relationship could become useful in defining possible fracture zone volumes incorporated into the geological model.

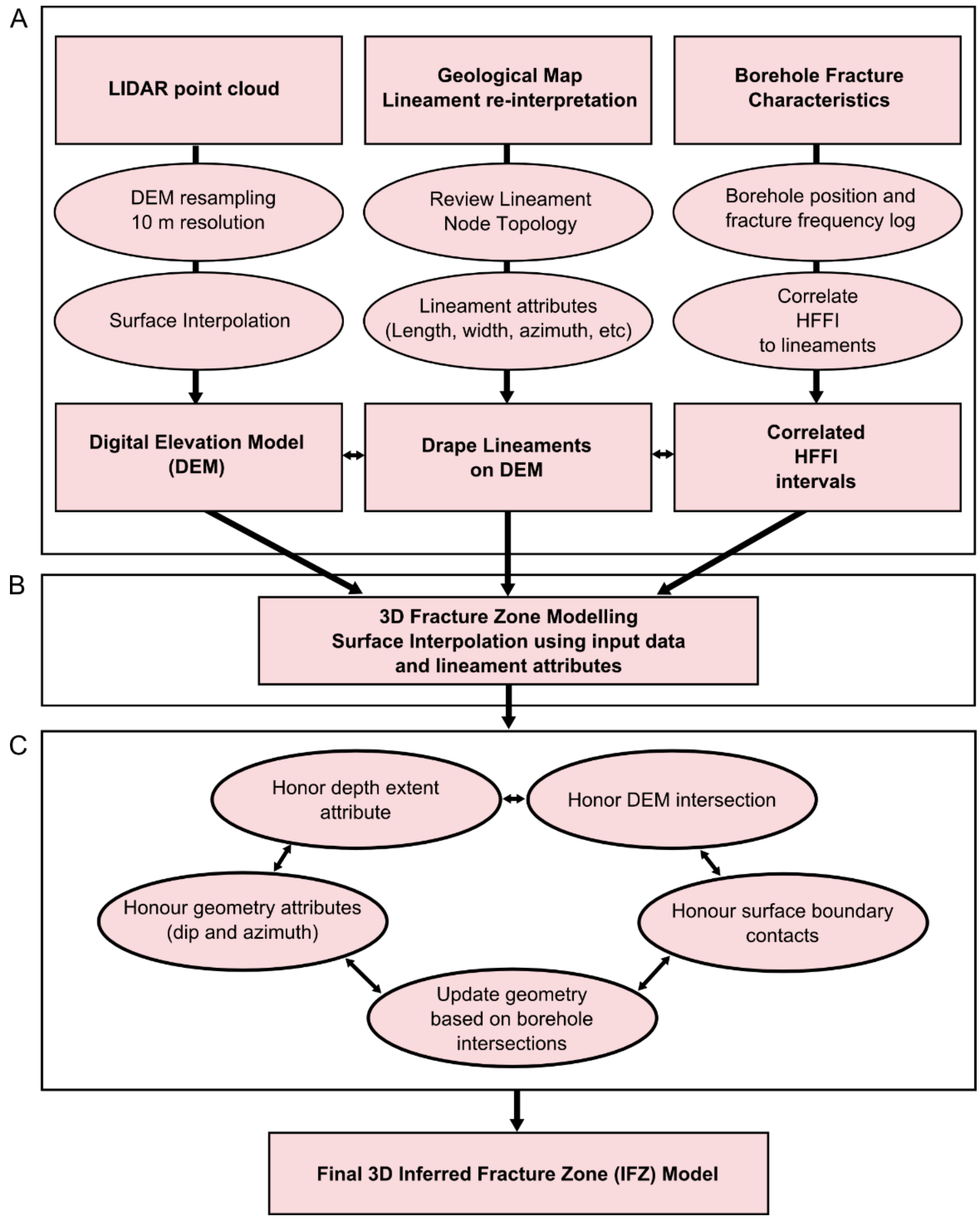

Figure 52. Workflow for modelling lineament traces as 3D inferred fracture zone surfaces.

Based on the reassessment of lineaments in Section 4.1, a total of 81 lineaments with trace lengths greater than 500 m occur within the site-scale volume and have been incorporated into the deterministic fracture zone model. Lineaments that are less than 500 m in length will be included in separate semi-deterministic and stochastic discrete fracture network models. Regarding three additional lineaments classified as diabase dykes, a decision has been made to include these features within the rock unit model (see Section 5.3), instead of the fracture zone model. These diabase dykes are interpreted as the Wabigoon dyke swarm and trend W-

NW through the site-scale model extent. Based on field mapping they do not show increased fracture intensity, and the dyke contacts are largely undeformed (Golder and PGW, 2018). The deterministic modelling procedure for the dykes is addressed separately in Section 5.6.

Results of the site-scale fracture zone model are presented in Figure 53. Figure 53a presents the fracture zones categorized based on their assigned fracture order (as discussed in Section 4.1.2), and Figure 53b shows the fracture zones grouped into separate orientation sets. As further information is determined by targeted fracture zone drilling or through ground and downhole seismic reflection surveys, their interpreted dip magnitudes and depth extents will be updated in the properties field of the fracture zone feature and their surfaces can be modified. These modelling results provide the initial deterministic fracture zone model, which will be iteratively updated as more information becomes available.

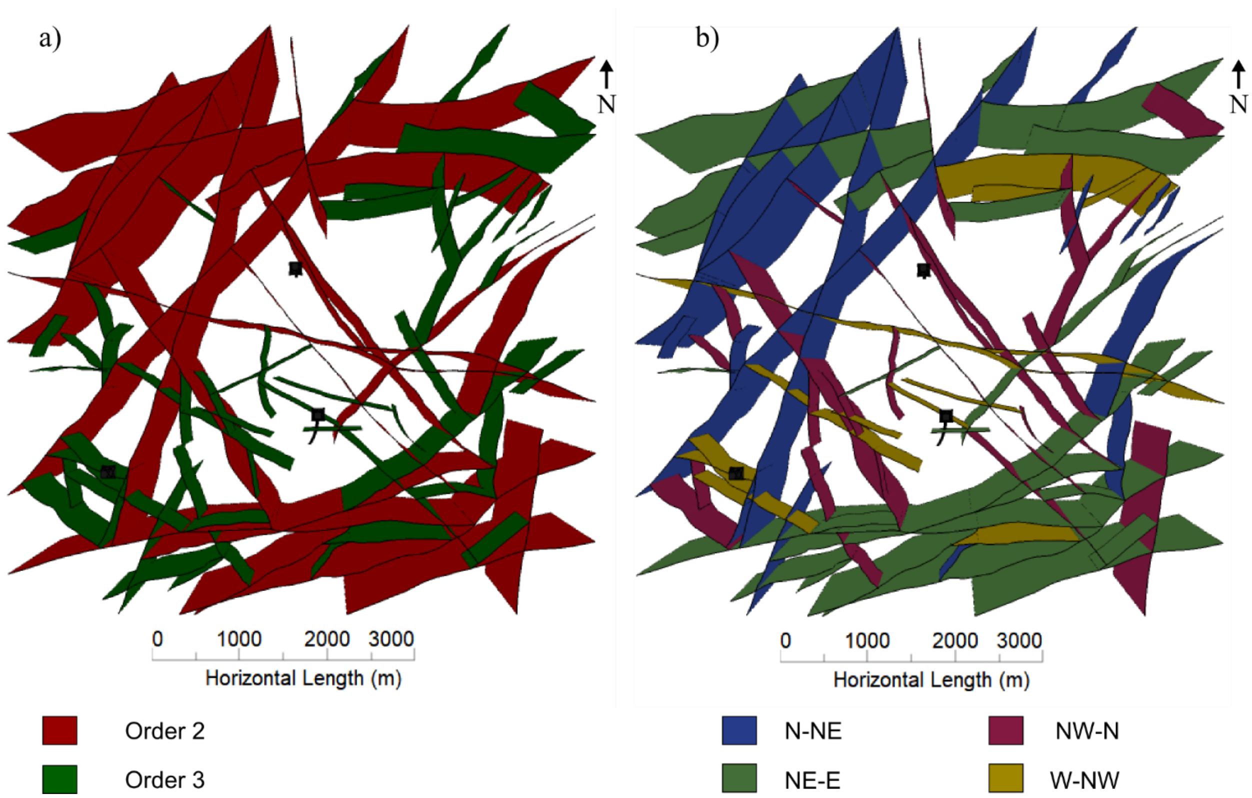

Figure 53. Spatial distribution of deterministically modelled inferred fracture zones in top view categorized in a) by order; and in b) by orientation set. Inferred fracture zones extend from ground surface to a depth equal to their total trace length (1:1 length to depth ratio). Unique identifier labels for each IFZ are displayed on Figure 19.

With the documented assumptions above, the fact remains that few of the interpreted lineaments have been confirmed by field data, either through borehole drilling or outcrop mapping. There remains uncertainty whether many of the resulting inferred fracture zones are truly bedrock structures within the subsurface and whether they are pathways for groundwater flow. As such, these model results will be iterative as additional field testing is acquired to address remaining questions.

5.5.2 Inferred Fracture Zones Guided by High Fracture Frequency Intervals in Boreholes and Lineament Traces

In addition to our initial vertical subsurface geometry assumptions assigned to the inferred fracture zones (IFZ), the following section describes how high fracture frequency intervals (HFFI) defined in boreholes (Section 4.2.6), envisaged below as potential fracture zone markers, are incorporated to update the geometry of the inferred fracture zone (IFZ) model previously presented in Section 5.5.1. As a result, borehole information has been used to update the geometry of fracture zones intersected in the subsurface.

Based on findings from the single borehole integration reports, five of the 81 lineament fracture zones (~6%) have been confirmed by intersection through borehole drilling (i.e., IG_BH02 and IG_BH03). Despite the intersections, correlating the lineament fracture zone traces to borehole high fracture frequency intervals still has its challenges. Based on results from surface mapping of outcrop-scale fractures, an initial assumption was made that lineaments extend vertically into the subsurface. Therefore, in associating identified HFFI's in the borehole to interpreted lineaments, the initial approach was to evaluate whether a surface projected vertically downward from the lineament trace intersects one of the interpreted HFFI's. If a vertical surface can not be correlated directly to any HFFI, then the dip of the surface is modified until the surface does intersect a fractured interval. Once the projected traces are correlated to borehole HFFI's, the characteristics of the HFFI, based on detailed logging information, are applied as characteristics of the inferred fracture zone. Regardless of whether or not the mean strike of an inferred fracture zone agrees with the dominant strike orientation of fracture clusters within a correlated HFFI, the dominant strike orientation based on the HFFI-IFZ intersection is honoured to represent the modelled strike of the IFZ.

Although each inferred fracture zone is modelled to a depth equal to its trace length, its dip magnitude and dip direction are now updated based on the intersection location of the borehole fracture zone marker. Similar to the strike, the mean dip orientation of the fracture zone surface may not agree with the dip magnitude of fractures in the borehole zone. However, the mean dip geometry of the fracture zone surface is inferred by matching the lineament to the borehole marker and calculating the mean dip over the entire surface. This is assumed to provide the best representation of the broader fracture zone geometry. Any fracture zones that are not correlated to borehole fracture zone markers, and lack other information on their subsurface geometry, are still assumed to be vertical.

As summarized in Section 3.3, IG_BH02 was drilled at ~70º inclination towards the southwest. Based on the borehole path, and the initial assumption of the vertically projected lineaments, the borehole was expected to intersect three inferred fracture zones, IFZ050, IFZ051 and IFZ072 (Figure 54 and Figure 55). However, based on the borehole fracture data, five fracture zone markers along the HFFIs have been interpreted within IG_BH02. Using the marker depths along the borehole, fracture intensity and fracture orientation from each HFFI, an attempt is made to correlate lineament traces to the borehole HFFI based on expert judgement and thereby update the geometry of some fracture zones.

Based on a comparison of fracture orientations with lineament trend, IFZ050 is interpreted to correlate with IG_BH02_HFFI_1 at a depth of 22 m along borehole IG_BH02. This high fracture frequency interval is dominantly composed of biotite granodiorite-tonalite with a 0.53 m feldspar-phyric tonalite dyke from 28.65 – 29.18 m. There are visible pink-coloured alteration halos (logged as potassic alteration and hematization) around the feldspar-phyric tonalite dyke. The tonalite dyke contacts cluster with the major fracture orientation peak that dips 85° toward the northeast (Figure 54a). The fractures in this interval are mainly joints with four logged faults and five logged veins. Fractures are well-spaced, and most are at a relatively low angle to the core-axis, indicating a steep dip. The intersection of these steep fractures and minor shallow dipping fractures create intervals of broken core, especially visible around the upper and lower contacts of the dyke. There are three shear zones associated with the major fracture peak (045/85) and one associated with the minor peak at 108/77 (Figure 54a). All shear zones are minor, discrete structures and are in the biotite granodiorite-tonalite with the exception of one logged at 28.91 m in the tonalite dyke. The increase in fracture frequency is almost certainly related to the tonalite dyke, as evidenced by the similar orientation of the contacts to the main fracture orientation peak. The lack of notable faults or shear structures suggests it is not a structurally significant interval. Figure 55 shows IFZ050 correlated surface with a mean dip magnitude of ~70º degrees inclined towards the north-northeast (007º).

IFZ051 is interpreted to correlate with IG_BH02_HFFI_4. This high fracture frequency interval is characterized as a 16.84 m long interval at a depth of 382 m along the borehole path. It contains a heterogeneous mix of dykes (i.e. aphanitic tonalite, feldspar-phyric tonalite, and pegmatite) at sub-metre to metre scale within the main biotite granodiorite-tonalite. There is visible pink-coloured alteration associated with the dykes, which is logged as hematization and potassic alteration. Significant silicification is also logged in association with the dykes, as well as minor chloritization and bleaching. IG_BH02_HFFI_4 has a broad cluster of fractures that dip shallowly toward the east (Figure 54b). Eight of the 12 dyke contacts are oriented parallel to the fracture peak, three are steeply inclined toward the northeast, and one is moderately inclined toward the east. There are 19 ductile shear zones logged in this interval, and 17 of them cluster with the main fracture peak. Fracture intensity and alteration visually increases around the dykes, in particular the thick feldspar-phyric tonalite dyke at 376.34 m. There are several ductile shear zones and one interval that is logged as sheared but appears to be infilled breccia in the middle of the feldspar-phyric tonalite dyke, around 380.25 m. The infill material is red, potentially iron oxide, suggesting a later-stage brittle overprint of the initially ductile fracture that involved iron-rich fluids. Eight faults and one broken core zone are logged in this interval, mainly associated with the dykes; seven of the eight faults and the broken core zone all cluster with the main orientation peak (061/18). The most common infill mineral logged is calcite, with iron oxide and quartz the next most common. As there is such a strong cluster of structures in this interval, all of the logged infill is associated with the main cluster. Muscovite infill shows the greatest spread in logged orientation, some instances cluster with the main fracture orientation peak while more than half (9/16) are randomly oriented.

Overall, IG_BH02_HFFI_4 is characterized by a strong cluster of brittle structures, an association of ductile structures that are similarly oriented, the presence of alteration around the dykes, and the brittle overprinting of ductile structures with iron oxide infill minerals. Despite the main cluster of fracture poles in IG_BH02_HFFI_4 being shallow dipping, the interval also contains a modest pole cluster with a high dip angle and a northwest trend consistent with the trend of the lineament linked to IFZ051. The resulting inferred fracture zone IFZ051 has a mean dip and dip direction of 87.5º towards 221º (Figure 55).

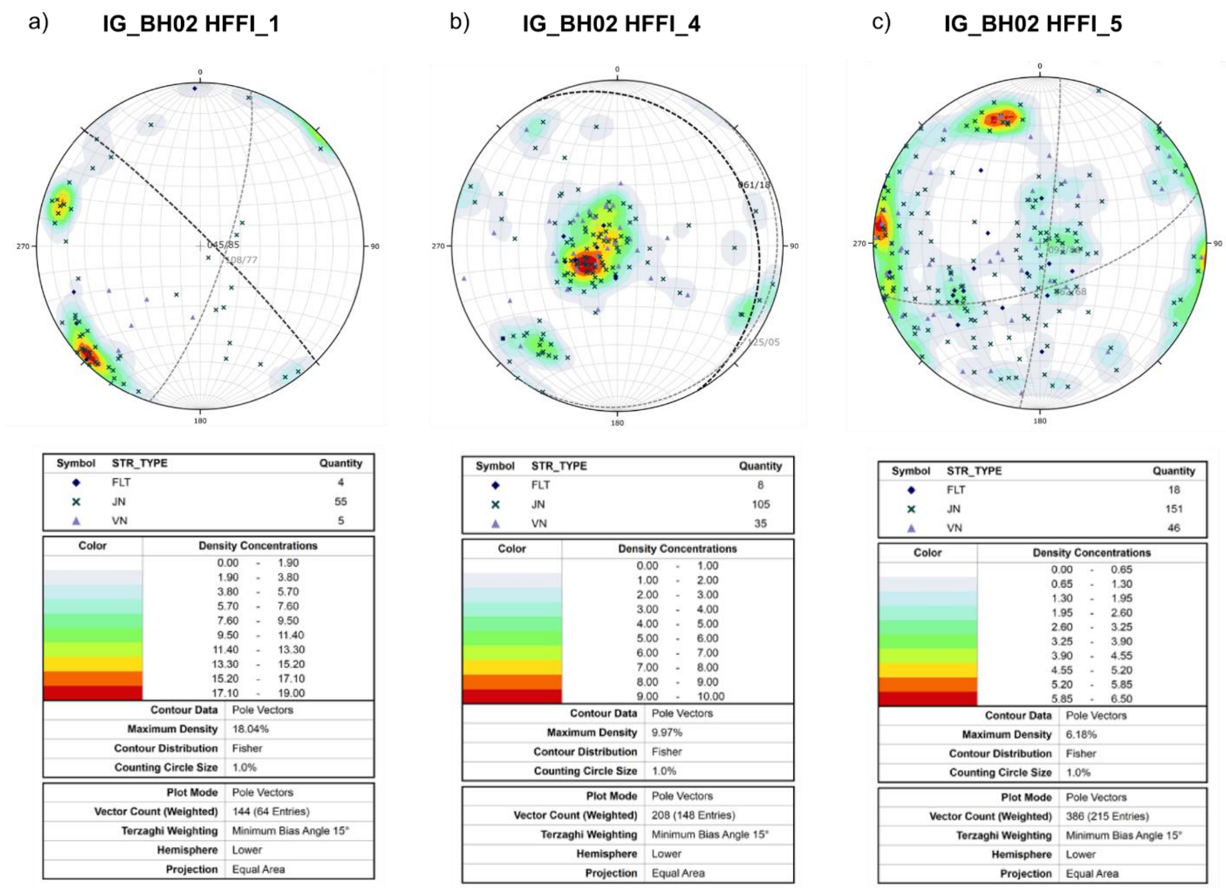

Figure 54. Stereonet plots of fracture orientations within the correlated high fracture frequency intervals.

IFZ072 is interpreted to correlate with the high fracture frequency interval IG_BH02_HFFI_5 within IG_BH02. Overall, the interval comprises several feldspar-phyric tonalite dykes, quartz dykes and amphibolites on metre scale hosted within the main biotite granodiorite-tonalite. There is pinkish alteration visible around the dykes and the amphibolite, logged as potassic alteration and some minor hematization, and a pale grey alteration that was logged as silicification and bleaching at the bottom of the interval. A sample of this grey alteration was sent for lithogeochemical and petrographic analysis and it was found to be almost 100% secondary albite, making this albitized interval the strongest alteration observed in IG_BH02. Minor chloritization is logged in association with the amphibolite.

Fractures within IG_BH02_HFFI_5 show a wide range in orientations with two dominant peaks defined, both steeply dipping, one toward the southeast and the other toward the east (Figure 54c). Of the ductile structures logged, one of 19 structures (a shear zone) is associated with one of the fracture peaks. The other 11 shear zones, single logged mylonite, and six foliation measurements are all clustered around the centre of the stereonet, dipping shallowly toward the north, northeast, and east, respectively. The most common infill mineral in the interval is calcite, followed by quartz, epidote, and chlorite. As with all structures in the interval, there is a significant spread in orientations with all of these infill types. The cluster defining planes that dip moderately toward the southeast does seem to have dominantly quartz infill logged, but otherwise there are no strong associations between orientation and mineral infill. Despite the broad spread in structural orientations, the presence of highly altered host rock (albitized biotite granodiorite-tonalite), the amphibolite, and the quartz dykes (interpreted as hydrothermal veins) suggest that this potentially is, or was in the past, an important zone of fluid movement. The overall strike of the fracture clusters does not directly correlate to the strike of IFZ072. However, the trend of IFZ072 bisects the mean orientation of the two fracture clusters. Using the depth projection assumption (i.e. 1:1 length to depth ratio) results in the bottom of the surface terminating at the borehole intersection. The resulting inferred fracture zone IFZ072 correlated with IG_BH02_HFFI_5 remains as near vertical with a mean dip and dip direction of 89.1º towards 210º (Figure 55).

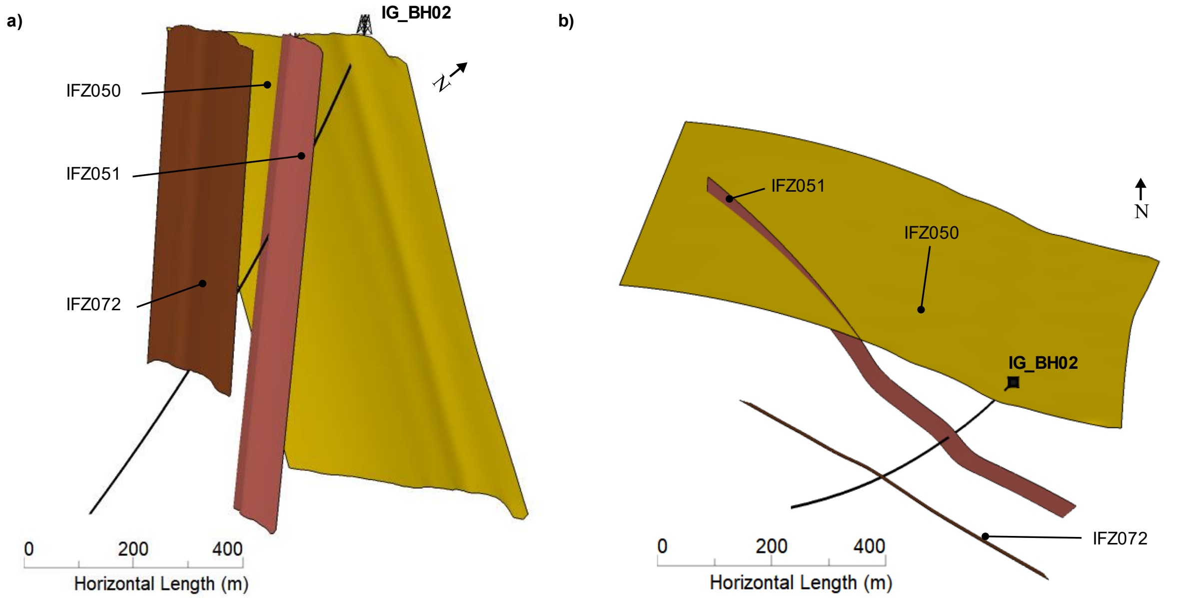

Figure 55. Lineament fracture zones IFZ050, IFZ051 and IFZ072 intersected by IG_BH02. a) presents an oblique view looking towards the NW at the fracture zones, and b) shows the top-view of the fracture zones. Black line shows the path of IG_BH02.

As summarized in Section 3.3, IG_BH03 was drilled at ~70º inclination towards the south which deviated slightly towards the southwest during drilling. Based on the borehole path, and the initial assumption of the vertically projected lineaments, the borehole was expected to intersect the vertical projection of two interpreted lineaments, i.e. the inferred fracture zones IFZ044 and IFZ071.

IFZ044 crosses the borehole path approximately 10 m south of the collar location and is initially approximated to be intersected by the borehole at roughly 25 m along drilled depth based on a vertically projected surface. However, based on the methodology currently used to define high fracture frequency intervals, no interval was defined in this shallow portion of the borehole. Despite this, a broad interval can be manually interpreted with a high fracture intensity that is just below the threshold for the peak picking analysis (Parmenter et al. 2021c). Fracture orientations within this interval shows consistent northwest strikes, which correlate well with the northwest trend of the lineament coupled to IFZ044. Therefore, based on these criteria, IFZ044 is interpreted to correlate with a peak in the fracture frequency log at approximately 35 m depth along the borehole. IFZ044 is modelled with a depth extent equal to its interpreted trace length, a dip magnitude of 84º and a dip direction 209º that are constrained based on the new interpreted borehole marker located at 35 m depth along the borehole.

IFZ071 is interpreted to correlate with the high fracture frequency interval IG_BH03_HFFI_3 along IG_BH03. The interval is primarily composed of biotite granodiorite-tonalite with metre-scale aplite and aphanitic tonalite dykes. The contacts of the aphanitic tonalite dyke cluster with the major fracture orientation peak dipping 85° toward 222, while the aplite dyke orientation does not have any association to the cluster defined. The strike direction of the main fracture cluster is roughly northwest trending, approximately 45º from the westerly strike of the lineament coupled to IFZ071. Moderate to highly pervasive potassic alteration is logged throughout this interval, and the fractures are well-spaced and predominantly steeply-dipping. Overall, there does not appear to be an increase in fracture intensity around either of the dykes. Despite these observations, the location of the IG_BH03_HFFI_3 along the borehole path at 484 m correlates well with the intersection of a near-vertical surface representing IFZ071. In addition, approximately 20 m shallower in the borehole, there is a cluster of fractures that share the same strike direction as the trend of the lineament coupled to IFZ071. It is possible that the IFZ071 surface may be better suited to intersect the borehole 20 m shallower based on the correlation of fracture trends. This is a local uncertainty that remains within the model and can be explored through further testing.

Borehole IG_BH01 was drilled vertically and therefore was not expected, based on its trajectory, to intersect a vertically-projected inferred fracture zone. However, the borehole is positioned in proximity to two northwest-trending lineaments located 130m and 180m to the northeast of the borehole collar identified in the model as inferred fracture zones IFZ030 and IFZ012. At a depth of approximately 800 m to 850 m in the borehole, there is a pronounced cluster of fractures dipping steeply towards the southwest, with a strike direction consistent with the trend of both the lineaments coupled to IFZ030 and IFZ012. This may suggest that at least one of these IFZ's is not vertical and, further, did indeed intersect IG_BH01 with an acute intersection angle. However, regardless of the fracture cluster, the core in this interval remains largely intact and does not show significant signs of brittle fracturing. Therefore, it is believed that the surface of the fracture zones remains somewhere to the northeast of borehole IG_BH01 and that the borehole may only intersect a margin of the potential damage zone. Future boreholes are planned to intersect both of these IFZ's to confirm their subsurface geometry and the model will be updated at that time.

From the three boreholes used in this report, a total of 15 high fracture frequency intervals have been identified based on a peak detection analysis using the total fracture frequency logs. Identification of the high fracture frequency intervals are described in detail in the single borehole integration reports and summarized in Section 4.2.6. Eleven of the 15 high fracture frequency intervals have not been correlated to a surface lineament trace. These remaining HFFI's have not been incorporated into this initial version of the IFZ model. However, these intervals are interpreted to represent fracture zones in the subsurface and will be included as part of the site-scale discrete fracture network model and incorporated in future model iterations.

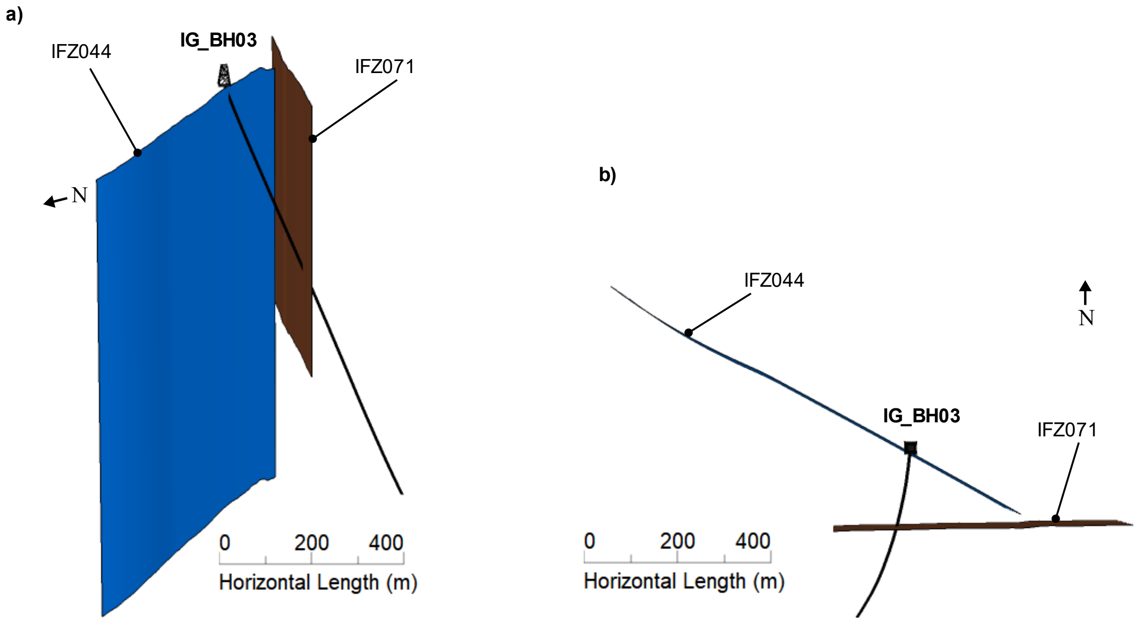

Figure 56. Lineament fracture zones IFZ044 and IFZ071 intersected by IG_BH03. a) presents an oblique view looking towards the NE at the fracture zones, and b) shows the top-view of the fracture zones. Black line shows the path of IG_BH03.

5.5.3 Inferred Fracture Zones Guided by Surface Fracture Mapping

Subsurface projection of inferred fracture zones is difficult with the sparsity of data currently available from the three initial boreholes. In some cases, fracture orientations from surface mapping data can be used to support decisions on the subsurface projection with the assumption that the associated fractures are correlated with the inferred fracture zone. This section describes an attempt to apply such a correlation to the subsurface projection of one inferred fracture zone by using the GSC/MIRA Sparse module in GOCAD.

Outcrop-scale fracture data from Golder and PGW (2018) has been extracted in proximity to a lineament coupled to the inferred fracture zone IFZ012 within 300 m from the interpreted lineament trace. Field data are filtered to include only those fractures with strikes ±45º degrees relative to the mean lineament trend, and dips greater than 45º degrees.

Figure 57a presents the top view of the fractures (as discs) and their spatial proximity to the lineament trace. Using the Sparse module, the fracture orientations are transferred to the lineament trace by using an averaged inverse distance weighted function to assign mean orientations to the trace within a search radius of 2000 m to generate a smooth dip and strike geometry. The lineament trace is then projected into the subsurface as a gripframe using 6 frame nodes (vertical) with a minimum separation of 250 m along the strike length (Figure 57b).

A triangulated surface with an approximate triangle element size of (25m sides) is interpolated through the gripframe representing the best-fit subsurface geometry of the fracture zone based on proximal fracture orientations (Figure 57c). The triangulated surface is linked to the original lineament trace at ground surface, and shares the same node spacing as the topographic surface along its intersection.

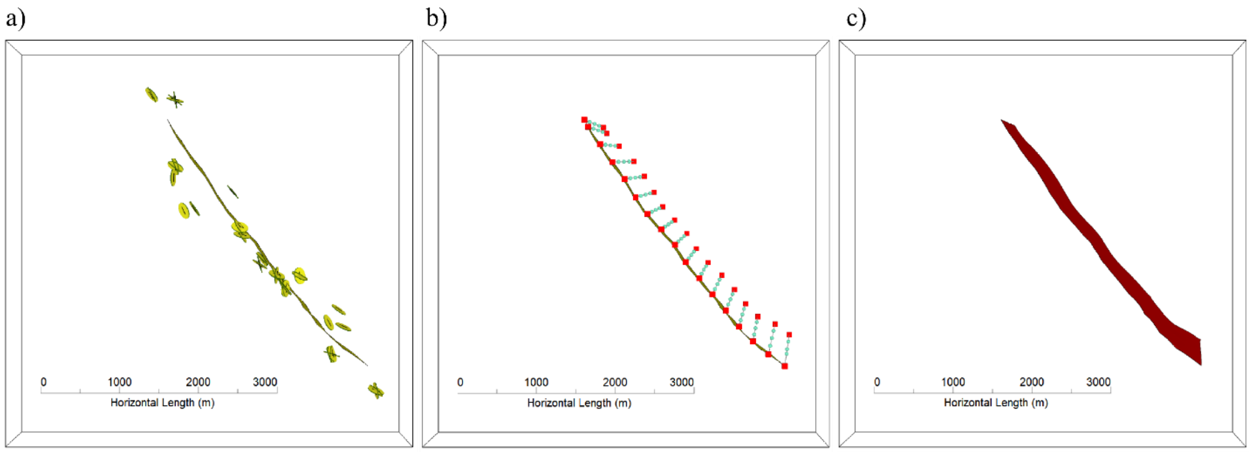

Figure 57. Interpreted subsurface projection of inferred fracture zone IFZ012 based on field fracture mapping orientations. a) lineament trace and fracture orientations in proximity to the trace. Field data are filtered to include only those fractures with strikes ±45º degrees of lineament trend, and dips greater than 45º. Filtered fracture orientations are transferred to lineament trace by neighbourhood search of 2000 m to generate a smooth dip and strike geometry. b) surface lineament trace projected into the subsurface using a gripframe from the GSC/Mira sparse module. c) final triangulated surface is interpolated through the gripframe representing the best-fit subsurface geometry of the inferred fracture zone based on proximal fracture orientations.

Figure 58 presents an oblique view looking towards the northwest of IFZ012. The resulting surface for IFZ012 has a calculated has a mean dip of 84º ±3.2º and a mean strike of 316º ±26º (mean dip direction towards 046º).

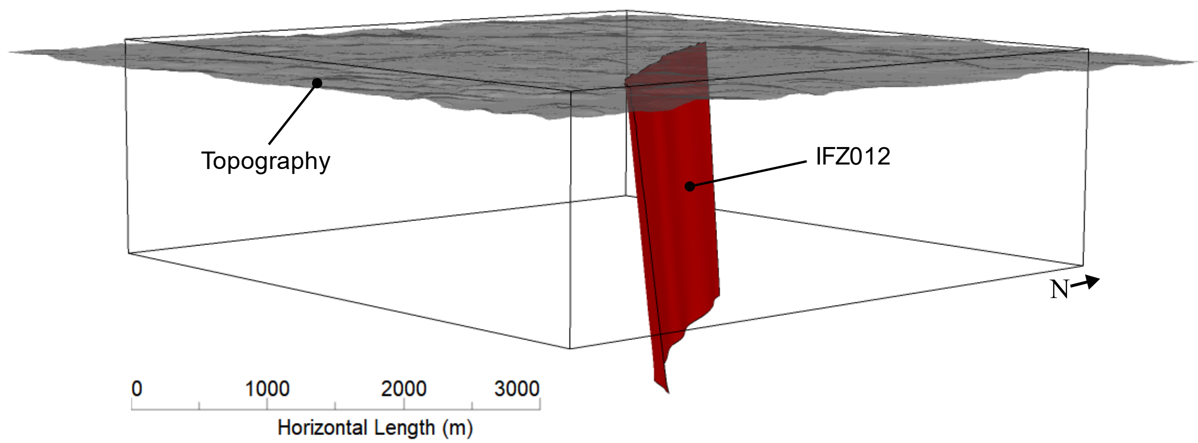

Figure 58. Oblique view of IFZ012 fracture zone looking towards the northwest. IFZ012 has a mean dip of 84º ±3.2º and a mean strike of 316º ±26º (mean dip direction of 46º).

5.6 Diabase Dyke Surface Model

Apart from the inferred fracture zones coupled to lineaments, other tabular bodies can be represented in the 3D geological model. Diabase dykes are modelled here as surfaces following the same workflow as that used for the fracture zones. However, at this stage, they are not considered to have undergone significant brittle deformation and their contact relationships are largely intact relative to the host rock (e.g. Golder and PGW 2018). Based on surface mapping, the diabase dyke contacts and lithology have similar fracture intensities as the biotite granodiorite-tonalite rock mass. The contacts have been observed with chilled margins. Future boreholes are planned to intersect the diabase dyke to evaluate their fracture characteristics and hydraulic properties in more detail. The diabase dyke model will be updated at that time.

The diabase dykes trend W-NW through the site-scale model extent and have been mapped on ground surface with a nominal width of 25 m based on a range from 18 m to 30 m (Golder and PGW, 2018). They are modelled as surfaces with a vertical extent from ground surface to the base of the model (Figure 59). This depth extent assumption differs from the fracture zone modelling. Based on Ernst et al. (2019), regional-scale diabase dyke swarms extend through much of Northern Ontario and are interpreted to have an extensive vertical and lateral geometry. Therefore, it is likely that these regional scale structures have a depth extent that far exceeds the base of the model even if their individual trace lengths are short (e.g. Dyke03 trace length is less than 2000m).

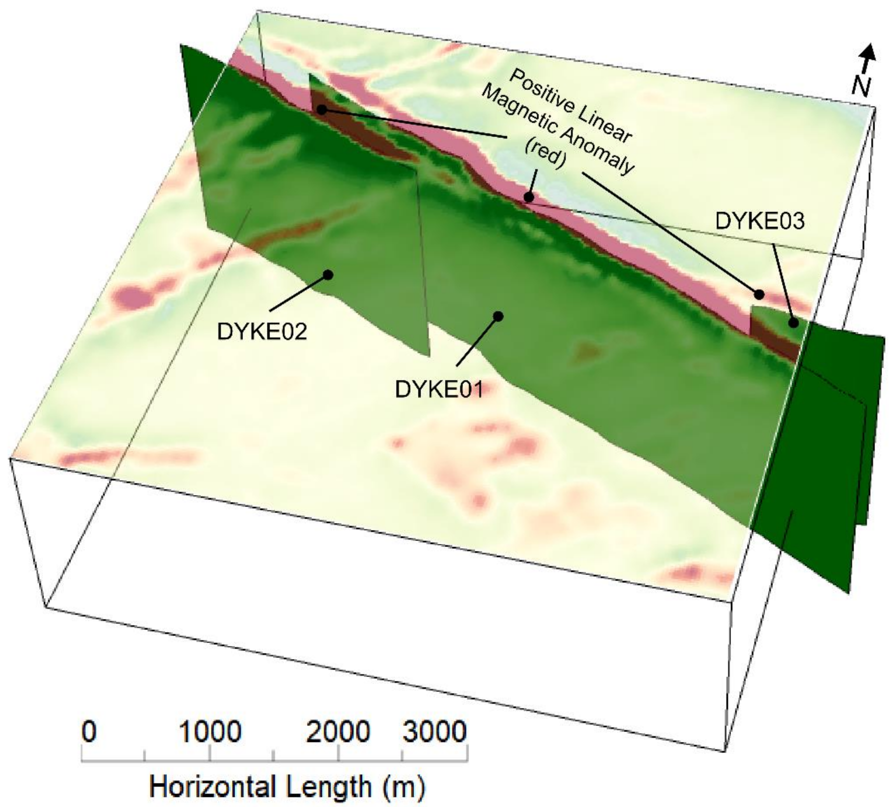

Figure 59. Wabigoon diabase dykes interpreted from airborne magnetic data and field mapping are represented as vertically projected surfaces. All dykes extend from ground surface to the base of the model domain.

5.7 Combined Models

The outcome of the integrated rock unit, integrated structural unit and inferred fracture zone modelling can be combined into two integrated models. Either of these volumetric models may be used, as needed, in future geoscientific studies.

For this purpose, a 3D regular voxel grid is generated with cell dimensions of 50m x 50m x 10m resulting in just over 1.6 million cells. The voxel grid is first subdivided based on the surfaces defining the rock unit domain boundaries and the separate regions are categorized into the rock unit regions where each cell is parameterized with the unique rock unit identifier. Once the IRU voxel model is established, it is overprinted with the diabase dykes. Each voxel cell that is intersected by the dyke surface is categorized as the voxel grid property.

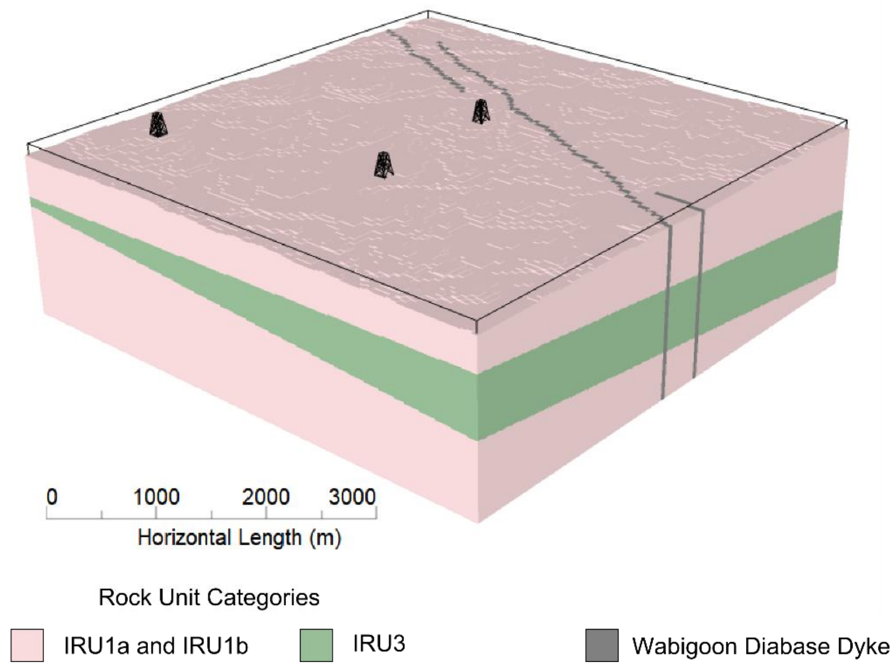

Figure 60. Voxelized integrated rock unit model overprinted with Wabigoon diabase dykes.

Similarly, for the second integrated model, a 3D voxel grid is subdivided into discrete structural units and each cell is parameterized with the structural unit identifier. In this case, the voxel grid is overprinted with the lineament-based fracture zone model. Each voxel cell that is intersected by a fracture zone surface is categorized as the voxel grid property.

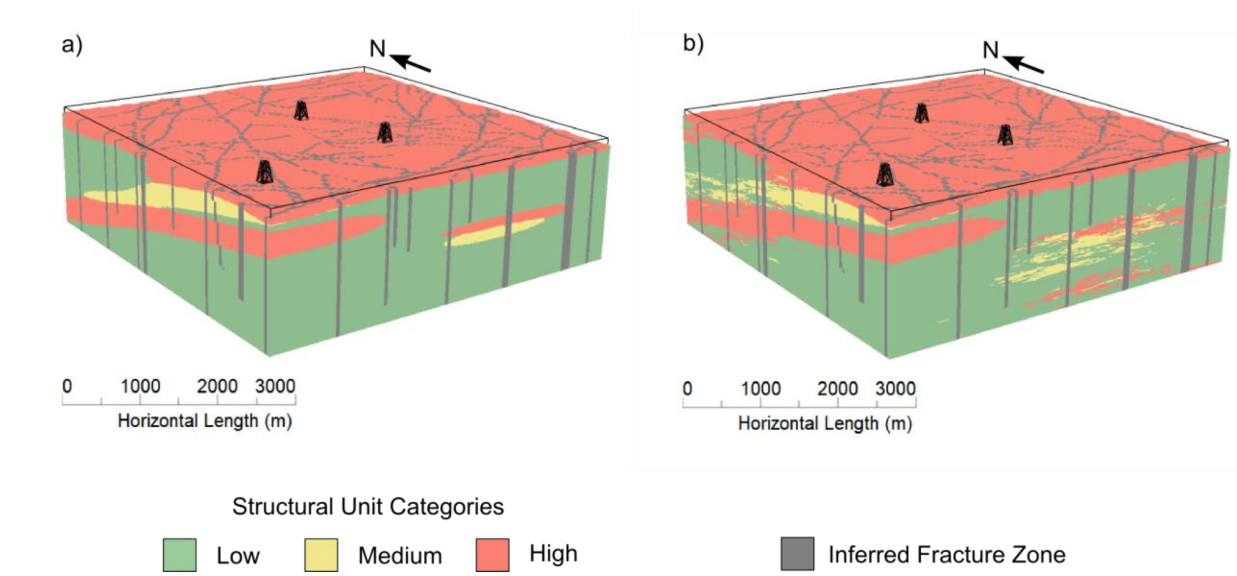

Figure 61. Voxelized integrated structural unit model based on a) indicator kriging and b) indicator simulation. Each model is overprinted with inferred fracture zone model.

6. Confidence Assessment

In the context of developing a robust 3D geological model to be used in evaluating the safety case for a used nuclear fuel repository, it is important to understand how data and model uncertainty impact the performance of a site. In recent years, numerous studies have focused on quantifying the uncertainties inherent in geological modelling (e.g. Suzuki and Caers 2008; Cherpeau et al. 2010; Caumon et al. 2009 Lindsay et al. 2012; Wellmann et al. 2010; Wellmann and Regenauer-Lieb 2012; Schweizer et al. 2017). This report presents the first iteration of the site-scale geological model, which incorporates a significant amount of information measured from the ground surface and subsurface information collected mainly from three drilled boreholes within the site-scale extent. This 3D model is considered to be sparsely constrained. It is acknowledged that building a 3D model with sparse data will have a high degree of uncertainty, and the projected information will most likely include inaccuracies. The process of acquiring additional data, and updating the model is an important step which allows the model to be iteratively evaluated. This step is considered critical in the process to validate the 3D model.

Sources of uncertainty can include inaccurate input data, poor data quality and data density, suboptimal model resolution, human error, etc. This uncertainty forecasted onto the model development can have a major impact on the 3D representation of the subsurface geology and will impact future drilling plans and subsurface predictions. In an ideal situation, enough boreholes would be drilled to sufficiently reproduce the exact reality (e.g. rock properties, lithological boundaries, etc.) of the subsurface. However, this is not feasible due to a number of factors (cost, time required, etc.). The ability to construct geologically realistic models is, therefore, facilitated through the use of modelling tools, such as surface and property interpolation methods, and through the collection of additional data sources (e.g. seismic reflection, gravity). As part of NWMO QA strategy, the geomodelling team document the use of the data sets in constructing the model and the assumptions used to make interpretations of the subsurface. Prior to developing the model, we aim to minimize the uncertainty associated with the input data by having the data independently reviewed and collected with a rigorous quality assurance plan.

The main source of uncertainty in this early version of the geological model is the sparsity of available input data. Figure 62 presents the density of data used to construct the initial geological model. Data considered here is defined as hard data and is either a direct measurement or field observation (geological core logging or field mapping data), or a feature that is derived from a geological interpretation (lineaments or cross-sections). As a visual metric, data density is derived by calculating the distance to each data object in a voxel grid. Distance from mapping data at outcrop and interpreted lineaments, all acquired at the ground surface, and from borehole data is calculated through the 3D voxel grid. The distance grids derived from each object are summed and presented as the log of the summed values. The results indicate that some regions of the 3D model tend to be well-constrained by hard input data (high data density), suggesting that geological model interpretations in these regions may have higher certainty. Areas of lower data density may require additional information to be collected if those areas are critical to the overall understanding of the site. Confidence in the geological model is expected to increase as a result of increasing data density.

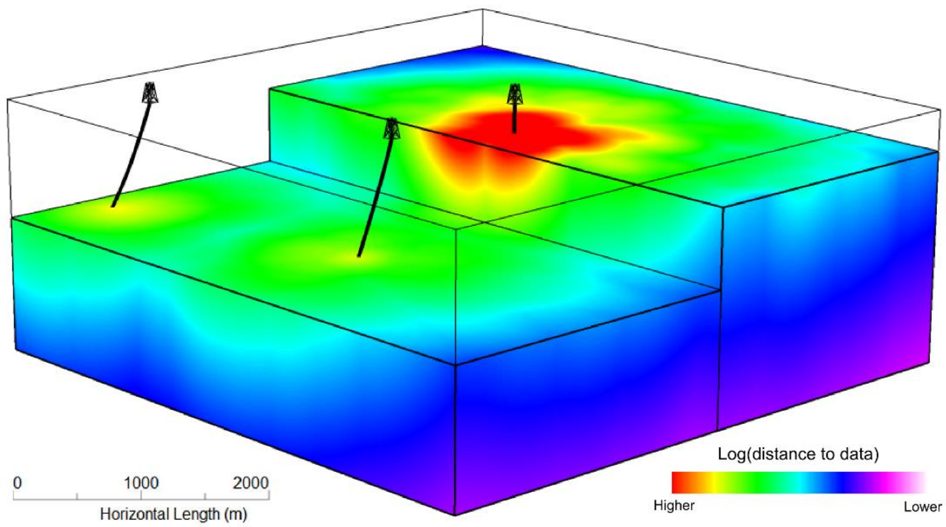

Figure 62. Uncertainty metric quantified by log distance to measured and interpreted input data. Metric indicates regions of the model that have a higher or lower degree of data density.

6.1 Main Uncertainties

6.1.1 RU and SU Modelling

Using methodologies described in each single borehole integration report rock unit (RU) and structural unit (SU) domain boundaries were defined. One uncertainty associated with the initial borehole interpretation of these geological elements is the precise location where they have been interpreted. It is possible that with the same raw data inputs, alternative approaches or other interpreters may have defined different domain boundaries and ultimately produced a different geological model for each borehole. With regards to the rock units, they are predominantly composed of biotite granodiorite-tonalite and there is no sharp contact that can be used to differentiate the rock units. The rock unit boundaries are largely based on the spatial clustering of amphibolites along the length of the borehole. As a result, the boundaries have a fair amount of subjectivity embedded in their locations. Despite this uncertainty, it is likely that these rock unit subdivisions adequately parse the borehole into domains that capture the general changes in the rock types that may be important in characterizing the geosphere. It will be important to evaluate whether additional geoscientific information from the other boreholes will fit within this rock unit framework or if a different picture will emerge.

There also exists a level of uncertainty associated with the choice of methods used for modelling the RU and SU domains between boreholes. The RU domains were modelled using a surface-based method where the domain boundaries are interpolated over large areas guided by the markers positioned in the boreholes. The SU domains were modelled using a voxel-based approach that relied on assumptions of the spatial variability and continuity of the SU domains between boreholes. The main drawback of each method in this initial model is the lack of geological information between boreholes.

6.1.2 Difficulty Linking Borehole HFFI to Lineaments to form Fracture Zones

One of the main uncertainties with the inferred fracture zone (IFZ) model is related to the initial process of tracing linear features from remote-sensing data: it is possible that different interpreters may result in a variety of different lineament traces. This level of uncertainty was somewhat reduced by the lineament tracing process that took into consideration the agreement of multiple interpreters on the location, truncation relationships and classification of each lineament. Subsequently, a decision was made to select lineament traces with a length greater than 500 m to represent fracture zones, with the assumption when using a depth extent equal to its trace length, the fracture zone surfaces will extend to a repository at a depth of 500 m below ground surface. To model these fracture zones several initial assumptions are made concerning the geometry, thickness, and down dip extension. These assumptions comprise additional levels of uncertainty that have the potential to impact the fracture zone intensity at potential repository depth, and will need to be investigated through additional field work and subsequent modelling work (e.g. flow and transport modelling, repository design, etc.).

An initial assumption, partly based on the relative straightness of the lineaments, is that the interpreted fracture zones are steep. Therefore, these were initially modelled as being vertical. Another assumption, less supported, is that the vertical extent is equal to the zone trace length. Both assumptions can have cascading impacts in the model results. Dip of fracture zones can be updated through borehole drilling or other geoscientific data (e.g. seismic reflection, etc.). Despite having drilled through five interpreted fracture zones, correlating lineament traces on surface to borehole derived high fracture frequency intervals remains a difficult task. High-fracture frequency intervals were defined along the boreholes using a statistically robust method, which is described in each of the single borehole integration reports (Parmenter et al. 2021a, 2021b and 2021c). However, this approach is non-unique as different intervals can be defined by modifying the parameters of the peak picking algorithm. Each high fracture frequency interval is comprised of fractures with a range of orientations that may or may not correlate with the dominant trend of the lineament correlated to the fracture zone. The ideal conceptualization of a fracture zone would include a borehole fractured interval with fracture geometries that are consistent with the larger scale lineament structure; in reality, this similarity in orientation is rarely observed. It is possible that in some cases, the lack of correlation with the fracture sets may be because the lineament trace associated with the IFZ is not truly a fracture zone, or that the fracture zone may terminate shallower then the borehole intersection. Overall, linking the high fracture frequency intervals to lineament traces is, therefore, a difficult task that requires significant judgement. In some cases, some proportion of the fracture orientations in the interval share a trend similar to the lineament, but the correlation is not always clear.

The uncertainties and assumptions summarised above provide a basis for evaluating the level of confidence in this initial site-scale geological model. It is acknowledged that this early model is developed using a sparse set of subsurface information. To reduce uncertainty, the desired solution is to acquire more data, such as additional borehole drilling, seismic reflection studies and field mapping, in an attempt to address issues of data sparsity. Prior to incorporating the new data into the model, data can be used to validate the current state of the model by measuring the spatial differences between the input data and the model data. After iterating the model based on new data inputs, the amount of spatial variation can be assessed by comparing the new model results against previous model versions. As the site is further investigated through additional borehole drilling, seismic reflection studies and field mapping, it is anticipated that the differences between subsequent model iterations will be reduced over time and the overall level of confidence in the model will increase.

Despite all the uncertainties described above, results from the subsurface information to date suggests the bedrock largely comprises an unaltered to weakly altered homogeneous biotite granodiorite-tonalite. Locally, where accessory rock types are encountered, they are relatively thin (typically less than 2 m along borehole length) and make up less than 5% of the overall bedrock. With the exception of the localized high fracture frequency intervals, the overall fracture intensity is low and fracture orientations seem to cluster fairly well into predictable fracture sets. All of this information suggests that, despite the inherent uncertainty in some of the modelling elements (e.g. RU, SU), these elements may not play a significant role in the ability of the site to host a deep geological repository. However, the role of these geological elements will continue to be investigated through future studies.

7. Summary

Developing a site-scale 3D geological model is an essential part of the Descriptive Geoscientific Site Model. The objective of this report and the 3D geological model is to develop a numerical representation of the subsurface that can be further used to evaluate the site for its potential to host a deep geological repository. This geological model forms the site framework to be used in associated geoscientific studies to develop discipline-specific sub-models, including geomechanical, thermal, hydrogeological, hydrogeochemical, and transport property models. This report defines the first iteration of the site-scale geological model, which incorporates a significant amount of information measured from the ground surface and subsurface information collected mainly from three drilled boreholes within the site-scale extent.

Main model inputs include:

1. Available data - water features, overburden cover;

2. Collected data - surface mapping, borehole geological and geophysical logging, and airborne geophysics and imagery; and

3. Integrated data - lineament mapping, single borehole integration reports, high fracture frequency intervals (HFFI), and integrated rock and structural units.

This initial version 1.0 of the 3D model is considered to be sparsely constrained. It is acknowledged that building a 3D model with sparse data will have a high degree of uncertainty, and the projected information will most likely not be completely accurate. The main sources of uncertainty in this iteration of the 3D model are sparsity of data, integrated rock unit and structural unit modelling, poorly defined variogram, and the difficulty linking borehole HFFI to surface lineaments. Eventually, as additional data is acquired and used in the model, remaining uncertainties will be minimized. Continually updated models will ultimately inform other geoscientific disciplines and will form the framework used in the design of an underground repository and the assessment of long-term safety of the site.

8. References

Achtziger-Zupančič, P., S. Loew, A. Hiller and G. Mariethoz. 2016. 3D fluid flow in fault zones of crystalline basement rocks (Poehla-Tellerhaeuser Ore Field, Ore Mountains, Germany). Geofluids, 16, 688–710.

ATLIS 2018. Ignace Revell Batholith LiDAR and orthoimagery survey, Ontario.

Berthe, D., Choukroune, P., Jegouzo, P. 1979. "Orthogneiss, mylonite and non coaxial deformation of granites: the example of the south Armorican shear zone", J. Struct. Geol., 1, p. 31-42.

Bethune, K.M., Helmstaedt, H.H. and McNicoll, V.J. 2006. Structural analysis of the Miniss River and related faults, western Superior Province: post-collisional displacement initiated at terrane boundaries; Can. J. Earth Sci., v. 43, p. 1031–1054.

Blackburn, C.E. and Hinz, P. 1996. Gold and base metal potential of the northwest part of the Raleigh Lake greenstone belt, northwestern Ontario-Kenora Resident Geologist's District; in Summary of Field Work and Other Activities 1996, Ontario Geological Survey, Miscellaneous Paper 166, p.113-115.

Brown, A., R.A. Everitt, C.D. Martin and C.C. Davison, 1995. Past and Future Fracturing In AECL Research Areas in the Superior Province of the Canadian Precambrian Shield, with Emphasis on The Lac Du Bonnet Batholith; Whiteshell Laboratories, Pinawa, Manitoba

Brown, J.L., 2002. Neoarchean evolution of the western—central Wabigoon boundary zone, Brightsand Forest area, Ontario. Unpublished M.Sc. thesis, University of Ottawa, Ottawa.

Caers, J. 2011., Modeling Uncertainty in the Earth Sciences. Wiley. pp 246.

Caumon, G., P. Collon-Drouaillet, C. Le Carlier de Veslud, S. Viseur and J. Sausse. 2009. Surface-Based 3D Modeling of Geological Structures. Mathematical Geosciences, 41, 927–945.

Cherpeau, N., G. Caumon and B. Lévy. 2010. Stochastic simulations of fault networks in 3D structural modeling. Comptes Rendus Geoscience, 342, 687–694.

Curtis, P., J. Petersson, C.-A. Triumf and H. Isaksson. Site Investigation SFR Deformation Zone Modelling. Model Version 0.1. SKB. Report P-09-48.

Davis, D.W., 1989. Final report for the Ontario Geological Survey on precise U–Pb age constraints on the tectonic evolution of the western Wabigoon subprovince, Superior Province, Ontario. Earth Science Department, Royal Ontario Museum, 30 p.

DesRoches, A., Sykes, M., Parmenter, A., Sykes, E., 2018. Lineament Interpretation of the Revell Batholith and Surrounding Greenstone Belts (No. NWMO-TR-2018-19). Nuclear Waste Management Organization.

Easton, R.M. 2000. Metamorphism of the Canadian Shield, Ontario, Canada. Volume I, The Superior Province. The Canadian Mineralogist, v. 38, p. 287-317.

Easton, R.M., Hart, T.R., Hollings, P., Heaman, L.M., MacDonald, C.A. and Smyk, M. 2007. Further refinement of the timing of Mesoproterozoic magmatism, Lake Nipigon region, Ontario; Canadian Journal of Earth Sciences, v.44, p.1055-186.

Ernst, R.E., D.A. Liikane, S.M. Jowitt, K.L. Buchan and J.A. Blanchard. 2019. A new plumbing system framework for mantle plume-related continental Large Igneous Provinces and their mafic-ultramafic intrusions. Journal of Volcanology and Geothermal Research, 384, 75–84.

Evans, J.P., C.B. Forster and J.V. Goddard. 1997. Permeability of fault-related rocks, and implications for hydraulic structure of fault zones. Journal of Structural Geology, 19, 1393–1404.

Everitt, R, Murray, J., Brown, A., Davison, C. 1996. Geology of the Lac Du Bonnet Batholith, Inside and Out: AECL's Underground Research Laboratory, Southeastern Manitoba (field B5). Geological Association of Canada, Winnipeg Section. p. 78, Geological Association of Canada, Winnipeg Section.

Fahrig, W.F. and T.D. West, 1986. Diabase dike swarms of the Canadian Shield; Geological Survey of Canada, Map 1627A.

Golder (Golder Associates Ltd.) and PGW (Paterson, Grant, and Watson), 2017. Phase 2 Geoscientific Preliminary Assessment, Geological Mapping, Township of Ignace and Area, Ontario. Prepared for Nuclear Waste Management Organization (NWMO). NWMO Report APM-REP-01332-0225. Mississauga, Canada.

Golder Associates Ltd., 2018a. Phase 2 Initial Borehole Drilling and Testing, Ignace Area: WP2 Data Report - Borehole Drilling and Coring for IG_BH01 (No. APM-REP-01332-0229). Nuclear Waste Management Organization.

Golder Associates Ltd., 2018b. Phase 2 Initial Borehole Drilling and Testing, Ignace Area: WP3 Data Report - Geological and Geotechnical Core Logging, Photography and Sampling for IG_BH01 (No. APM-REP-01332-0230). Nuclear Waste Management Organization.

Golder Associates Ltd., 2019a. Phase 2 Initial Borehole Drilling and Testing, Ignace Area: WP5 Data Report - Geophysical Well Logging for IG_BH01 (No. APM-REP-01332-0234). Nuclear Waste Management Organization.

Golder Associates Ltd., 2020a. Phase 2 Initial Borehole Drilling and Testing, Ignace Area. WP02 Data Report - Borehole Drilling and Coring for IG_BH303 (No. APM-REP-01332-0241). Nuclear Waste Management Organization.

Golder Associates Ltd., 2020b. Phase 2 Initial Borehole Drilling and Testing, Ignace Area. WP05 Data Report - Geophysical Well Logging for IG_BH03 (No. APM-REP-01332-0248). Nuclear Waste Management Organization.

Golder Associates Ltd., 2020c. Phase 2 Initial Borehole Drilling and Testing, Ignace Area. WP03 Data Report - Geological and Geotechnical Core Logging, Photography and Sampling for IG_BH03 (No. APM-REP-01332-0250). Nuclear Waste Management Organization.

Golder Associates Ltd., 2020d. Phase 2 Initial Borehole Drilling and Testing, Ignace Area. WP02 Data Report – Borehole Drilling and Coring for IG_BH02 (No. APM-REP-01332-0240). Nuclear Waste Management Organization.

Golder Associates Ltd., 2020e. Phase 2 Initial Borehole Drilling and Testing, Ignace Area. WP03 Data Report – Geological and Geotechnical Core Logging, Photography and Sampling for IG_BH02 (No. APM-REP-01332-0249). Nuclear Waste Management Organization.

Golder Associates Ltd., 2020f. Phase 2 Initial Borehole Drilling and Testing, Ignace Area. WP05 Data Report – Geophysical Well Logging for IG_BH02 (No. APM-REP-01332-0269). Nuclear Waste Management Organization.

Gómez-Hernández, J. and Srivastava, M. 1990. ISIM3D: An ANSI-C three-dimensional multiple indicator conditional simulation program. Computers & Geosciences, 16, 395–440.

Halla, J. 2018. Highlights on Geochemical Changes in Archaean Granitoids and Their Implications for Early Earth Geodynamics. Geosciences, 8, 353. https://doi.org/10.3390/geosciences8090353

Halla, J., van Hunen, J., Heilimo, E., Hölttä, P. 2009. Geochemical and numerical constraints on Neoarchean plate tectonics. Precambrian Research, 174, 155–162. https://doi.org/10.1016/j.precamres.2009.07.008

Hanes, J.A. and Archibald, D.A. 1998. Post-orogenic tectonothermal history of the Archean western Superior Province of the Canadian Shield by conventional and laser Ar-Ar dating. Abstracts with programs - Geological Society of America, v. 30(7), p.110-110.

Hartley, L. et al. 2017. Discrete Fracture Network Modelling (Version 3) in Support of Olkiluoto Site Description 2018. Posiva Oy Report WR-2017-32.

Haus, M. and Pauk, T. 2010. Data from the PETROCH lithogeochemical database; Ontario Geological Survey, Miscellaneous Release---Data 250. ISBN 978-1-4435-3732-2 [CD] ISBN 978-1-4435-3731-5

Heaman, L.M. and Easton, R.M. 2006. Preliminary U-Pb geochronology results from the Lake Nipigon Region Geoscience Initiative; Ontario Geological Survey, Miscellaneous Release—Data 191.

Hull, J. 1988. Thickness-displacement relationships for deformation zones. Journal of Structural Geology, 10, 431–435.

Johri, M., E.M. Dunham, M.D. Zoback and Z. Fang. 2014. Predicting fault damage zones by modeling dynamic rupture propagation and comparison with field observations: Modeling Fault Damage Zones. Journal of Geophysical Research: Solid Earth, 119, 1251–1272.

Journel, A. G., 1983, Nonparametric estimation of spatial distributions: Math Geol. v. 15, no. 3, p. 445–468.

Kamineni, D.C., Stone, D. and Peterman, Z. E. 1990. Early Proterozoic deformation in the western Superior province, Canadian Shield, Geological Society of America Bulletin, v. 102, p. 1623-1634.

Kolyukhin, D. and A. Torabi. 2012. Statistical analysis of the relationships between faults attributes. Journal of Geophysical Research: Solid Earth, 117.

Kresz, D.U., 1987. Geology of the Kawashegamuk Lake area, District of Kenora; Ontario Geological Survey, Open File Report 5659, 201p.

Larbi, Y., Stevenson, R., Machado, N., and Breaks, F. 1995. Isotopic evolution of Late Archean leucogranites and progressive cratonization in the western Superior Province. Abstracts, Western Superior Lithoprobe Second Annual Workshop, Lithoprobe Report 53, p.47-53.

Lindsay, M.D., L. Aillères, M.W. Jessell, E.A. de Kemp and P.G. Betts. 2012. Locating and quantifying geological uncertainty in three-dimensional models: Analysis of the Gippsland Basin, southeastern Australia. Tectonophysics, 546, 10–27.

Nur, A. 1982. The origin of tensile fracture lineaments. Journal of Structural Geology, 4, 31–40.

OGS (Ontario Geological Survey), 2005a. Digital Northern Ontario Engineering Geology Terrain Study (NOEGTS). Ontario Geological Survey, Miscellaneous Release of Data 160.

OGS (Ontario Geological Survey), 2011. 1:250 000 scale bedrock geology of Ontario, Ontario Geological Survey, Miscellaneous Release Data 126 - Revision 1.

Parmenter, A., Waffle, L., DesRoches, A. 2020. An updated bedrock geology map and geological database for the northern portion of the Revell batholith (No. NWMO-TR-2020-08). Nuclear Waste Management Organization.

Parmenter, A., Waffle, L., DesRoches, A. 2021b (*in prep*). Phase 2 Initial Borehole Drilling and Testing, Ignace Area. WP10 – Geological Integration Report for Borehole IG_BH02 (no. APM-REP-01332-0265). Nuclear Waste Management Organization

Parmenter, A., Waffle, L., DesRoches, A. 2021c (*in prep*). Phase 2 Initial Borehole Drilling and Testing, Ignace Area. WP10 – Geological Integration Report for Borehole IG_BH03 (no. APM-REP-01332-0266). Nuclear Waste Management Organization.

Parmenter, A., Waffle, L., DesRoches, A., Carvalho, J., Neufeld, A. 2021a (*in prep*). Phase 2 Initial Borehole Drilling and Testing, Ignace Area. WP10 – Geological Integration Report for Borehole IG_BH01 (no. APM-REP-01332-0260). Nuclear Waste Management Organization.

Pennacchioni, G., and Mancktelow, N.S. 2007. Nu-cleation and initial growth of a shear zone net-work within compositionally and structurally heterogeneous granitoids under amphibolite fa-cies conditions: Journal of Structural Geology, v. 29, p. 1757–1780, https://doi .org/10.1016/j.jsg.2007.06.002.

Pennacchioni, G., G. Di Toro, P. Brack, L. Menegon and I.M. Villa. 2006. Brittle–ductile–brittle deformation during cooling of tonalite (Adamello, Southern Italian Alps). Tectonophysics, 427, 171–197.

Percival, J.A. and R.M. Easton, 2007. Geology of the Canadian Shield in Ontario: an update. Ontario Power Generation, Report No. 06819-REP-01200-10158-R00 and Ontario Geological Survey, Open File Report 6196, 65p.

Percival, J.A., McNicoll, V.J., Brown, J.L. and Whalen, J.B. 2004. Convergent margin tectonic, central Wabigoon subprovince, Superior Province, Canada. Precambrian Research, v. 132, p. 213-244.

Pyrcz, M.J. and Deutsch. C.V. 2014. Geostatistical Reservoir Modeling. p. 450, Oxford university press USA.

Raymond, L.A., 2002. Chapter 6: Basalt and Ultramafic Rocks, in: Petrology: The Study of Igneous, Sedimentary, and Metamorphic Rocks. McGraw-Hill Science, Engineering & Mathematics.

Sanborn-Barrie, M., and Skulski, T. 2006. Sedimentary and structural evidence for 2.7 Ga continental arc-oceanic-arc collision in the Savant-Sturgeon greenstone belt, western Superior Province, Canada. Canadian Journal of Earth Sciences, v. 43, p. 995-1030.

Sanborn-Barrie, M., and Skulski, T. 2006. Sedimentary and structural evidence for 2.7 Ga continental arc-oceanic-arc collision in the Savant-Sturgeon greenstone belt, western Superior Province, Canada. Canadian Journal of Earth Sciences, v. 43, p. 995-1030.

Sander Geophysics Limited (SGL), 2020. 3D Geophysical Forward and Inversion Modelling of the Revell Batholith and Surrounding Greenstone Belt. (No. APM-REP-01332-0270). Nuclear Waste Management Organization.

Satterly, J. 1960. Geology of the Dyment area, Ontario Department of Mines, Annual Report Vol. 69, pt. 6, 32p.

Schweizer, D., P. Blum and C. Butscher. 2017. Uncertainty assessment in 3-D geological models of increasing complexity. Solid Earth, 8, 515–530.

Scibek, J. 2020. Multidisciplinary database of permeability of fault zones and surrounding protolith rocks at world-wide sites. Scientific Data, 7, 95.

SGL (Sander Geophysics Ltd.). 2015. Phase 2 Geoscientific Preliminary Assessment, Acquisition, Processing and Interpretation of High-Resolution Airborne Geophysical Data, Township of Ignace, Ontario. Prepared for Nuclear Waste Management Organization (NWMO). NWMO Report APM-REP-06145- 0002. Toronto, Canada.

SRK (SRK Consulting Inc.) and Golder (Golder Associates Ltd.), 2015. Phase 2 Geoscientific Preliminary Assessment, Observation of General Geological Features, Township of Ignace, Ontario. Prepared for Nuclear Waste Management Organization (NWMO). NWMO Report APM-REP-06145-0004. Toronto, Canada.

Stephens, M.B. et al. 2007. Geology Forsmark Site Descriptive Modelling Forsmark Stage 2.2. SKB. Report R-07-45.

Stone, D., 2009. Geology of the Bending Lake Area, Northwestern Ontario (Open File Report No. 6240), Summary of Field Work and Other Activities 2009. Ontario Geological Survey, Sudbury, Canada.

Stone, D., 2010a. Geology of the Stormy Lake Area, Northwestern Ontario, Project Unit 09-003 (Open File Report No. 6260), Summary of Field Work and Other Activities 2010. Ontario Geological Survey, Sudbury, Canada.

Stone, D., 2010b. Precambrian geology of the central Wabigoon Subprovince area, northwestern Ontario (Open File Report No. 5422). Ontario Geological Survey.

Stone, D., Davis, D.W., Hamilton, M.A., Falcon, A., 2010. Interpretation of 2009 Geochronology in the Central Wabigoon Subprovince and Bending Lake Areas, Northwestern Ontario, Project

Unit 09-003 (Open File Report No. 6260), Summary of Field Work and Other Activities 2010. Ontario Geological Survey.

Stone, D., Halle, J., Chaloux, E., 1998. Geology of the Ignace and Pekagoning Lake Areas, Central Wabigoon Subprovince (Misc. Paper No. 169), Summary of Field Work and Other Activities 1998. Ontario Geological Survey.

Stott, G.M., Corkery, M. T., Percival, J.A., Simard, M. and Goutier, J. 2010. A revised terrane subdivision of the Superior Province; in Summary of Field Work and Other Activities 2010, Ontario Geological Survey, Open File Report 6260, p.20-1 to 20-10.

Suzuki, S. and J. Caers. 2008. A distance-based prior model parameterization for constraining solutions of spatial inverse problems. Mathematical geosciences, 40, 445–469.

Szewczyk, Z.J. and West, G.F. 1976. Gravity study of an Archean granitic area northwest of Ignace, Ontario Canadian Journal of Earth Sciences, v. 13, p. 1119-1130.

Taylor, S.R., McLennan, S.M., 1985. The continental crust: Its composition and evolution. United States.

Terzaghi, R.D., 1965. Sources of Error in Joint Surveys. Géotechnique 15, 287–304.

Thurston, P. 1991. Geology of Ontario: Introduction; in Geology of Ontario, Ontario Geological Survey, Special Volume 4, Part 1, p. 3-25.

Tomlinson, K.Y., Stott, G.M., Percival, J.A. and D. Stone. 2004. Basement terrane correlations and crustal recycling in the western Superior Province: Nd isotopic character of granitoid and felsic volcanic rocks in the Wabigoon Subprovince, N. Ontario, Canada; Precambrian Research, v. 132, p. 245-274.

Virtanen, P. et al. 2020. SciPy 1.0--Fundamental Algorithms for Scientific Computing in Python. Nature Methods, 17, 261–272.

Wanless, R.K. 1970. Isotopic age map of Canada; Geological Survey of Canada, Map 1256A, Compilation 1969.

Wellmann, F. and G. Caumon. 2018. 3-D Structural geological models: Concepts, methods, and uncertainties. Advances in Geophysics, vol. 59, p. 1–121, Elsevier.

Wellmann, J.F. and K. Regenauer-Lieb. 2012. Uncertainties have a meaning: Information entropy as a quality measure for 3-D geological models. Tectonophysics, 526, 207–216.

Wellmann, J.F., F.G. Horowitz, E. Schill and K. Regenauer-Lieb. 2010. Towards incorporating uncertainty of structural data in 3D geological inversion. Tectonophysics, 490, 141–151.

Whalen, J.B., J.A. Percival, V.J. McNICOLL and F.J. Longstaffe. 2002. A mainly crustal origin for tonalitic granitoid rocks, Superior Province, Canada: implications for late Archean tectonomagmatic processes. Journal of Petrology, 43, 1551–1570.

Appendix A: Summary of Inferred Fracture Zone (IFZ) Attributes

Summary of Inferred Fracture Zone (IFZ) Attributes

The following table provides a summary of attributes compiled for the updated lineaments (see section 4.1) used as input in the inferred fracture zone model. These attributes include:

Linea_ID: Unique alpha-numeric identifier assigned to each interpreted lineament. This identification is used in the inferred fracture zone model for traceability.

Length: sum of the trace length for the polyline segments that make up each interpreted lineament

Strike: preferred strike direction of the lineament trace based on a length-weighted mean of polyline segments that make up each interpreted lineament

Width: the inferred fracture zone width calculated based on a derived empirical equation from SKB (Stephens et al., 2007). This width value is considered preliminary and will be updated as more site-specific information is collected.

Inferred: interpretation of the nature of the interpreted trace lineament being a brittle inferred fracture zone of a ductile shear zone, or a dyke.

Order: interpretation of the degree of possible deformation and is based on evidence from the remote sensing data from which it is derived.

Set: subdivision of the lineaments into broad sets based on a threshold query of the lineament strike attribute. The set thresholds are set at 0-45, 45-90, 90-135, and 135-180 degrees.

Additional attributes derived from the borehole high fracture frequency intervals and from the inferred fracture zone model are also included to describe the characteristics of the feature. These attributes include:

Mean Dip: calculated mean dip of the inferred fracture zone model surface

Mean Dip Direction: calculated mean dip direction of the inferred fracture zone model surface

Borehole Identification: name of borehole that the inferred fracture zone surface intersects

HFFI Identification: the high fracture frequency interval that the inferred fracture zone is correlated with.

Borehole Measured Depth: the measured depth along the borehole axis where the inferred fracture zone intersects the borehole.

Linea_ID	Length [m]	Strike [deg]	Width* [m]	Inferred	Order	Set	Mean Dip [deg]	Mean Dip Direction [deg]	Borehole Identification	HFFI Identification	Borehole Measured Depth [m]	Report Section/ Reference
IFZ001	11502.6	73.3	60.1	Brittle	2	NE-E	90					
IFZ002	10962.2	177.5	58.4	Brittle	2	NW - N	90					
IFZ003	10773.0	39.8	57.8	Brittle	2	N - NE	90					
IFZ004	8265.4	40.6	49.3	Brittle	2	N - NE	90					
IFZ005	7755.3	104.8	47.4	Brittle	2	W - NW	90					
IFZ006	7674.6	61.0	47.1	Brittle	2	NE-E	90					
IFZ007	6572.7	83.6	43.0	Brittle	2	NE-E	90					
IFZ008	6177.4	72.6	41.4	Brittle	2	NE-E	90					
IFZ009	5616.9	81.2	39.1	Brittle	2	NE-E	90					
IFZ010	5559.3	17.3	38.9	Brittle	2	N - NE	90					
IFZ011	4136.8	39.6	32.5	Brittle	2	N - NE	90					
IFZ012	3951.8	140.9	31.7	Brittle	2	NW - N	83.7	44				Section 5.5.3
IFZ013	3781.0	75.9	30.8	Brittle	2	NE-E	90					
IFZ014	3428.0	138.0	29.1	Brittle	2	NW - N	90					
IFZ015	3396.4	149.5	28.9	Brittle	2	NW - N	90					
IFZ016	3069.7	87.8	27.2	Brittle	3	NE-E	90					
IFZ017	2857.7	51.7	26.1	Brittle	3	NE-E	90					
IFZ018	2645.3	73.4	24.9	Brittle	2	NE-E	90					
IFZ019	2566.7	94.3	24.4	Brittle	2	W - NW	90					
IFZ020	2371.2	73.1	23.3	Brittle	2	NE-E	90					
IFZ021	2367.5	36.2	23.3	Brittle	2	N - NE	90					
IFZ022	2338.6	31.9	23.1	Brittle	2	N - NE	90					
IFZ023	2087.6	146.8	21.6	Brittle	3	NW - N	90					
IFZ024	1994.5	100.4	21.0	Brittle	2	W - NW	90					
IFZ025	1970.4	132.5	20.9	Brittle	3	NW - N	90					
IFZ026	1924.4	73.4	20.6	Brittle	2	NE-E	90					
IFZ027	1875.8	166.6	20.2	Brittle	2	NW - N	90					
IFZ028	1757.8	24.1	19.5	Brittle	3	N - NE	90					
IFZ029	1708.3	73.4	19.1	Brittle	2	NE-E	90					
IFZ030	1610.1	145.4	18.5	Brittle	2	NW - N	90					
IFZ031	1346.4	149.9	16.6	Brittle	3	NW - N	90					
IFZ032	1330.6	94.0	16.5	Brittle	3	W - NW	90					

IFZ033	1326.3	69.6	16.4	Brittle	3	NE-E	90					
IFZ034	1315.1	105.3	16.4	Brittle	3	W - NW	90					
IFZ035	1288.7	117.5	16.2	Brittle	3	W - NW	90					
IFZ036	1284.0	84.4	16.1	Brittle	3	NE-E	90					
IFZ037	1215.4	42.1	15.6	Brittle	3	N - NE	90					
IFZ038	1164.3	63.4	15.2	Brittle	3	NE-E	90					
IFZ039	1158.7	63.1	15.2	Brittle	2	NE-E	90					
IFZ040	1127.8	155.9	14.9	Brittle	3	NW - N	90					
IFZ041	1120.9	3.4	14.9	Brittle	3	N - NE	90					
IFZ042	1066.5	129.5	14.4	Brittle	3	NW - N	90					
IFZ043	1004.0	175.1	13.9	Brittle	3	NW - N	90					
IFZ044	958.9	118.7	13.5	Brittle	3	W - NW	84.1	209	IG_BH03	no HFFI identified	36 m	Section 5.5.2
IFZ045	951.9	69.6	13.5	Brittle	3	NE-E	90					
IFZ046	949.6	90.5	13.5	Brittle	3	W - NW	90					
IFZ047	945.8	46.4	13.4	Brittle	3	NE-E	90					
IFZ048	900.2	80.7	13.0	Brittle	3	NE-E	90					
IFZ049	888.7	125.3	12.9	Brittle	3	NW - N	90					
IFZ050	861.8	109.5	12.7	Brittle	3	W - NW	69.6	17	IG_BH02	IG_BH02_HFFI_1	22 m	Section 5.5.2
IFZ051	842.8	122.0	12.5	Brittle	3	W - NW	86.9	221	IG_BH02	IG_BH02_HFFI_4	382 m	Section 5.5.2
IFZ052	840.0	86.7	12.5	Brittle	3	NE-E	90					
IFZ053	835.5	22.7	12.5	Brittle	3	N - NE	90					
IFZ054	791.3	122.9	12.1	Brittle	3	W - NW	90					
IFZ055	781.3	160.9	12.0	Brittle	3	NW - N	90					
IFZ056	780.4	53.9	12.0	Brittle	3	NE-E	90					
IFZ057	777.3	177.3	11.9	Brittle	3	NW - N	90					
IFZ058	771.7	19.3	11.9	Brittle	3	N - NE	90					
IFZ059	763.5	51.6	11.8	Brittle	3	NE-E	90					
IFZ060	752.7	151.7	11.7	Brittle	3	NW - N	90					
IFZ061	741.9	122.0	11.6	Brittle	3	W - NW	90					
IFZ062	741.0	89.9	11.6	Brittle	3	NE-E	90					
IFZ063	740.0	111.5	11.6	Brittle	3	W - NW	90					
IFZ064	730.2	127.0	11.5	Brittle	3	NW - N	90					
IFZ065	729.5	22.6	11.5	Brittle	3	N - NE	90					
IFZ066	725.8	144.2	11.5	Brittle	3	NW - N	90					
IFZ067	717.1	117.3	11.4	Brittle	3	W - NW	90					

IFZ068	699.6	35.7	11.2	Brittle	3	N - NE	90					
IFZ069	668.6	59.5	10.9	Brittle	3	NE-E	90					
IFZ070	635.5	161.2	10.6	Brittle	3	NW - N	90					
IFZ071	612.1	88.7	10.3	Brittle	3	NE-E	87.9	179	IG_BH03	IG_BH03_HFFI_3	484 m	Section 5.5.2
IFZ072	600.9	120.1	10.2	Brittle	3	W - NW	89.1	210	IG_BH02	IG_BH02_HFFI_5	676 m	Section 5.5.2
IFZ073	578.4	43.0	10.0	Brittle	3	N - NE	90					
IFZ074	577.5	143.0	10.0	Brittle	3	NW - N	90					
IFZ075	570.7	129.6	9.9	Brittle	3	NW - N	90					
IFZ076	532.6	48.4	9.5	Brittle	3	NE-E	90					
IFZ077	529.6	169.6	9.5	Brittle	3	NW - N	90					
IFZ078	519.8	33.1	9.4	Brittle	3	N - NE	90					
IFZ079	513.2	32.2	9.3	Brittle	3	N - NE	90					
IFZ080	510.4	169.2	9.3	Brittle	3	NW - N	90					
IFZ081	501.8	30.5	9.2	Brittle	3	N - NE	90					